UNIVERSITÀ DEGLI STUDI DELL'INSUBRIA

Dipartimento di Scienza e Alta Tecnologia

Academic Year 2022-2023

Master Degree in Physics

ADVANCED TRACKING SYSTEM FOR CRYSTAL PHYSICS

Author: Stefano Carsi

Matricola 736512

Supervisor:	Prof.ssa Michela Prest Università degli Studi dell'Insubria
Co-supervisor:	Dr. Erik Vallazza INFN - Milano Bicocca

I was an ordinary person who studied hard.
There are no miracle people.
Richard Feynman

Contents

Introduction

Crystals are solid materials composed of microscopic constituents (either atoms, molecules or ions) arranged in a highly ordered structure, the crystal lattice. Crystals play a crucial role in particle Physics and in fact they are widely used in the design of particle detectors and beam instrumentation. However, in such applications they are generally treated as unordered materials: this approximation is justified by the fact that a crystal reveals its ordered nature to an external observer only under certain conditions.

One of the limits of this approximation is the fact that it cannot explain several phenomena which can be observed when a charged particle impinges on a crystal with a small angle with respect to one of its symmetry axes/planes. In such cases, the incident particle may be "trapped" inside the potential well generated by the crystal axis/plane and then be forced to oscillate in such well. This effect is known as *channelling* and results in the particle following the direction of the crystal axis/plane itself. Moreover, if the crystal is bent along the beam direction, the net effect for the channelled particle is a deflection of its direction with respect to the incoming one. These phenomena have been studied for decades and they are now understood well enough to be exploited in the development of novel tools for particle Physics applications.

The idea for this thesis work was born in the framework of two possible applications of crystals which require an intense experimental activity on charged particle beams to understand their feasibility:

- The development of a novel technique for the efficient production of high intensity positron beams: this idea is based on the fact that the radiation emitted by a charged particle when trapped inside a crystal has a higher intensity with respect to the bremsstrahlung one, due to the particle multiple oscillations occurring in the axial potential well. It is thus possible to use a thin crystal to produce high energy secondary photons from a beam of high energy electrons, and then use another crystalline target to make the photons convert into e^+e^- pairs, with an overall reduced amount of budget material. This idea is being pursued

by the e+BOOST (Intense positron source Based On Oriented crySTals) project, financed by the Italian Ministry of Research.

- The development of a new generation of bent crystals: the insertion of a lattice interruption at the very beginning of the crystal should act as a focussing lens and thus should yield a channelling efficiency of nearly 100 %. This technical development has been proposed by the GALORE project of the National Institute of Nuclear Physics.

Both these projects need an intense test activity on extracted beams and require to track the incoming charged particles (and in the case of GALORE, also the outgoing direction of the particle) with a high spatial resolution. The detection system developed by the INSULAB group of the Insubria University, based on microstrip silicon detectors, has been used in several crystal tests and is able to satisfy this requirement.

This thesis work has started from this system and has improved it in order to meet another requirement which is the possibility of collecting a statistics large enough in a relatively short time to study the crystal behaviour.
For the test of such crystals in fact, a low divergence beam with a small beam profile is necessary, that is, particles impinging onto the crystal within the angular acceptance of the phenomena under test. However, reducing the beam divergence results in a large beam profile and thus in a larger percentage of particles that do not cross the crystal itself. In order to acquire a large enough statistics, the tracking system was upgraded to make it able to select a small portion of the beam. This possibility was achieved by allowing the microstrip tracking detectors to self generate a trigger signal when the charged particle crosses the detector itself. The frontend and readout electronics needed to be upgraded to reach this goal: for instance, the firmware of a custom designed board was programmed to implement different logical conditions with the trigger signals from different modules, such as the AND or the OR of these signals, in order to select just a part of the beam and to reduce the divergence.
The upgraded system was first tested in the laboratory and then on an extracted electron beam, before being used in the data taking for the two experiments.

This thesis is organized as follows. Chapter 1 opens with the description of some applications of bent crystals in particle Physics to move then to a brief overview of the Physics of crystals with a particular focus on the channelling effect occurring inside bent crystals and on the crystal-induced enhancement of the pair production probability. This chapter ends presenting the crystal based hybrid positron source and the GALORE project, the two experiments that required the upgrade of the readout electronics of the tracking system.

Chapter 2 is dedicated to the description of the experimental test setups and the beamlines for which it has been designed and optimized: the CERN T9 and H8 extracted beamlines and the Frascati BeamTest Facility.

Chapter 3 presents the INSULAB silicon tracking systems and describes their frontend and readout electronics, with a focus on the parts which were improved in the framework of this thesis for the self generation of the trigger. In the last part of this chapter, the INSULAB Data AcQuisition System (DAQ) is also described.

Chapter 4 is dedicated to the preliminary characterization of the frontend electronics in the laboratory: the readout ASICs (Application Specific Integrated Circuits) have been tested using an external calibration signal to ensure that each channel worked properly and in terms of the noise trigger rate. The chapter ends with the on beam characterization of the beam telescopes at the BeamTest Facility of the Frascati National Laboratories.

The final chapter of this thesis summarizes a few results from two data takings for the GALORE project and the crystal based hybrid positron source. These results, from the measurement of the channeling efficiency of the GALORE crystal to the radiation enhancement in the e+BOOST test, want to underline the features of the system that allowed to collect the data in a short time and with the quality needed to understand the feasibility of such projects.

Chapter 1

The Physics of Crystals

Crystals or crystalline solids are solid materials in which the microscopic constituents are arranged in a highly ordered microscopic structure forming a *crystal lattice* [1]. Since their first observation in 1913 [2], many new "directional" effects in crystals have been theorized and studied.

In fact, when a particle impinges on a crystal with a small angle with respect to a crystal plane or axis, directional effects might show up: for instance the particle may be trapped and forced to propagate oscillating between crystal planes in the so called *channelling* condition.

If a crystal is bent along the direction of motion, a channelled particle is deflected with respect to the incoming angle. A bent crystal of few millimeters along the beam direction can behave as a hundreds of Tesla bending dipole, without energy consumption or the need of a cryogenic system, making it suitable for the integration in existing accelerators and beamlines [3].

Nowadays crystal properties are well understood and many research groups have begun to investigate their possible technological applications, such as the possibility to build compact electromagnetic calorimeters [4] or to efficiently collimate high-luminosity particle beams by removing the beam halo to prevent radiation damage to the accelerator components or background in the experiments [5].

This chapter opens with the description of a few applications of bent crystals in particle Physics, to move then to a brief theoretical review of crystal Physics. The chapter continues with the description of a crystal-based positron source that exploits the radiation emitted by channelled particles which converts into electron-positron pairs. The last section is dedicated to GALORE, an INFN (Istituto Nazionale di Fisica Nucleare) project which aims at overcoming the maximum channelling efficiency reached up to now ($\sim 80\,\%$) with an innovative new generation of bent crystals.

1.1 Bent Crystals in Particle Physics

In the following sections some applications of bent crystals in particle Physics will be presented, concerning the LHC halo extraction, the design of an intense gamma source and possible techniques for beam manipulation.

1.1.1 LHC Halo Extraction

The Physics Beyond Colliders (PBC) group at CERN is investigating the possibility of exploiting the potential of the CERN accelerator complex and infrastructure to broaden the research spectrum with a fixed-target program beyond the colliding-beam Physics. A powerful probe for studying the Physics beyond the Standard Model is represented by the measurement of the *electric* and *magnetic dipole moments*. The standard approach to perform these measurements consists in applying a *dipolar magnetic field* to induce a *dipole moment precession*. Measuring the angular distributions and energy spectra of the decay products, which depend on the induced precession, allows the dipole moment measurement. However, conventional magnets cannot be used for short-lived charmed baryons, such as Λ_c^+, because their magnetic fields induce a too weak precession. The Λ_c^+ magnetic moment measurement is particularly interesting because it is closely related to the magnetic moment of the *charm quark*, which has never been directly measured [6] [7].

The equivalent magnetic field acting on a particle trapped between a bent crystal planes can be several orders of magnitude larger than what can be reached with ordinary dipole magnets and can thus help in overcoming this problem [8] [9].

This technique has already been proved by the E761 collaboration at the Fermilab Proton Center using a $800\,\mathrm{GeV}/c$ proton beam onto a copper target in order to produce the Σ^+ baryon and to measure its magnetic moment precession [10].

The CERN LHC is the world largest collider, nowadays capable of accelerating protons up to $6.8\,\mathrm{TeV}/c$ [11], which plans to reach $7\,\mathrm{TeV}/c$ as well as upgrading to a High Luminosity (HL) design by 2030 during Run 4 [12]. However, no extracted beamlines are present. A possibility to overcome this problem might be represented by the *double crystal concept*, as depicted in figure 1.1. The idea is based on channelling in bent crystals: a particle impinging with a small angle with respect to a crystallographic plane/axis becomes trapped (*channelled*) and is forced to travel aligned to the plane/axis; if the crystal is bent, the channelled particle is deflected with respect to the incoming direction. A detailed discussion of planar channelling in bent crystals is presented in section 1.3. Basically, a first bent crystal (Target Collimator

Crystal for Splitting, TCCS) steers some protons from the LHC secondary halo (see figure 1.2 for a sketch of the collimation hierarchy and refer to [13] and references therein for a detailed description of the collimation hierarchy) and directs them toward a fixed target. A second bent crystal (Target Collimator Crystal for Precession, TCCP) is placed immediately after the target and the short-lived particles produced during the collision can precess inside it. The second crystal must have a large bending angle to provide a significant effective magnetic field for the precession to be measurable. The values for the bending angles were optimized using MAD-X simulations, and are 50 µrad for the TCCS and 7000 µrad for the TCCP [6] [5].

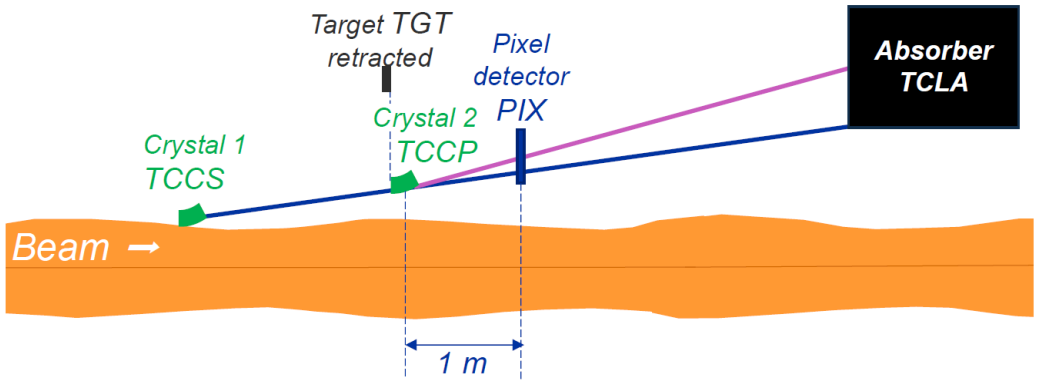

Figure 1.1: Layout of the Proof of Principle experiment for extracting the LHC halo. The TCCS is aligned with the edge of the main beam (orange) channelling protons (blue) onto the TCCP. Some protons are also channeled by the TCCP (purple) so that a double-spot forms on a pixel detector (PIX) 1 m downstream. Any remaining channeled protons are absorbed by a downstream collimator (TCLA). The target (TGT) can be retracted independently. Image and caption from [5].

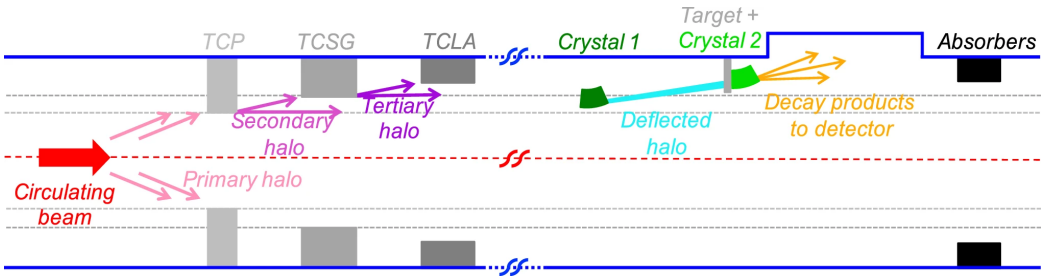

Figure 1.2: Working principle of the double-crystal scheme for fixed-target experiments and dipole moment measurements at the LHC, and its integration in the collimation hierarchy. Image and caption from [6].

LHC offers 8 different Insertion Regions (IR), 4 of which host the 4 experiments (ALICE (IR2), ATLAS (IR1), CMS (IR5) and LHCb (IR8)). Two IRs are particularly appealing for the installation of a double crystal setup and the relative instrumentation needed to validate the concept. Even if IR8 could take the advantage of the LHCb detectors, suited for forward Physics thanks to the experiment asymmetric design, it was decided to use the IR3 off-momentum collimation region. In this way, a Proof-of-Principle test can collect useful information to validate the double-crystal concept, providing input to the future Physics Beyond Colliders layouts since the LHC Run 3, and the same setup can be used without moving key components for the final experiment with the HL-LHC, starting in LHC Run 4 foreseen in 2030 [6].

A challenging element of such an experiment might be represented by the need of maximizing the number of Protons on Target (PoT) while keeping the losses on superconducting magnets below the quenching limits. For sure a dedicated optics could be designed, but the price to pay is high: first of all the commissioning may require years, but, most important, a dedicated optics would need dedicated operation conditions, which might result incompatible with all the other running experiments.

The double crystal technique is a way to go beyond the Physics of high energy colliders in a short time and without the need for new accelerator complexes to be built. The key elements of this concept are the crystals, that have to be extensively tested and characterized to be able to predict their behavior. The TCCS and TCCP were tested in August 2023 by the SELDOM collaboration on the H8 (PPE128) SPS extracted beamline; figure 1.3 presents the TCCP silicon crystal mounted on the goniometer used to align the crystal to the beam. In the following chapters of this thesis, the experimental system requirements to measure the *channelling efficiency* and the *deflection angle* of such crystals with *high spatial resolution* will be described.

1.1.2 Radiation Production

It is well known from electromagnetism that a charged particle, when accelerated, emits radiation; this is basically *bremsstrahlung* (a german word which means *stopping radiation*). Since the acceleration is defined in classical mechanics as a vector

$$\boldsymbol{a} = \frac{\mathrm{d}^2\boldsymbol{x}}{\mathrm{d}t^2}$$

it can either vary in magnitude or direction. The outgoing direction of a channelled charged particle inside a bent crystal is different from the incoming one: the particle has been accelerated and thus radiation has been emitted

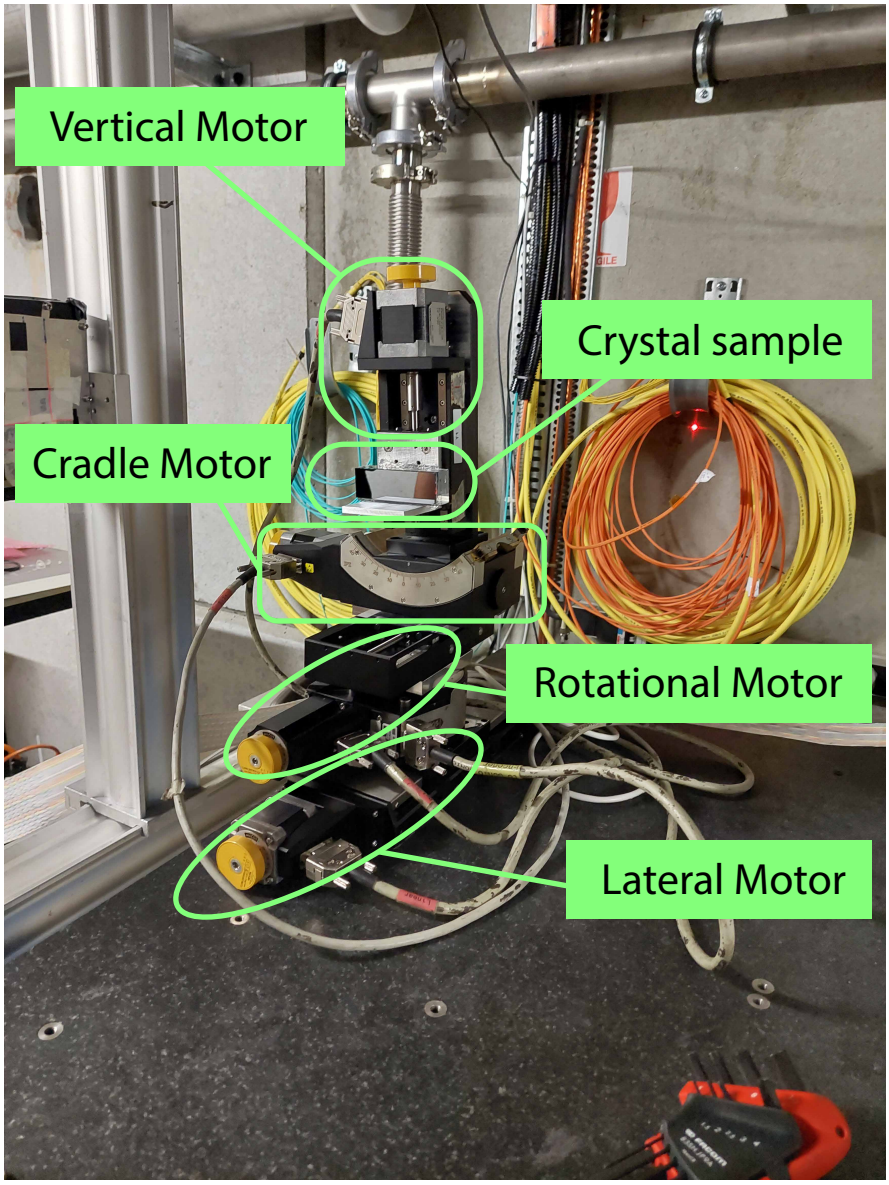

Figure 1.3: Photo of the TCCP silicon crystal mounted on the goniometer required to align the crystal to the beam. This crystal has been tested in August 2023 by the SELDOM collaboration on the H8 (PPE128) SPS extracted beamline.

(see figure 1.4 for a sketch of the trajectory of a channelled particle inside a bent crystal).

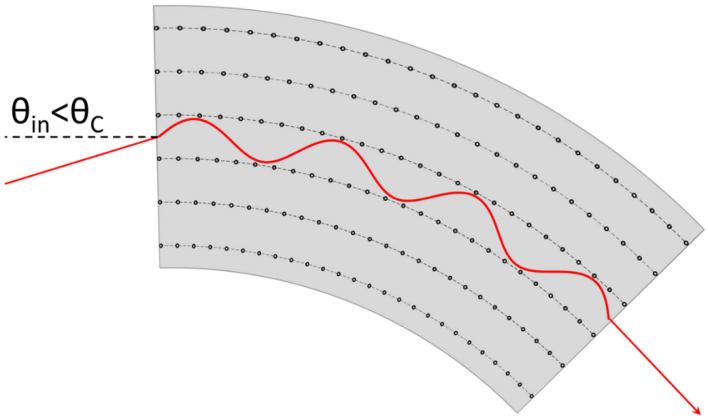

Figure 1.4: Positive charged particle trajectory (red line) inside a bent crystal. If the incidence angle θ_{in} is smaller than the critical angle θ_{C}, the particle is trapped between the atomic planes (black dots). Image from [3].

This is the idea of TECHNO-CLS [14] a project funded by the European Commission to produce innovative gamma-ray Crystal-based Light Sources (CLS) in the 100 keV–1 GeV range, where technologies based on magnetic fields cannot be used [15]. The crystals under test are made of diamond, silicon and germanium with Small Amplitude and Small Period (SASP): the parameters of the produced radiation can be tuned by varying the amplitude and the period of the bending.

Figure 1.5 presents three different crystal samples tested ad DESY (Deutsches Elektronen-Synchrotron) during May 2022.

The construction of a CLS is a challenging technological task, which covers multiple fields, from the crystal preparation, thus material science, solid state Physics, nanotechnology, up to the experimental system to test and characterize such crystals. In particular, beam manipulation and radiation detection innovative designs are needed.

A CLS might find application in nuclear medicine for the production of rare isotopes, non-destructive imaging of complex molecular systems with a good enough resolution for detecting the position of nuclei or to photo-induce nuclear reactions [16].

In [17] it has been shown that a channelled charged particle can emit intense Channelling Radiation (ChR) and that the characteristic energy scales with the beam energy E according to a $E^{3/2}$ power law. Nowadays high-quality electron beams of tunable energies within the tens of MeV/c range

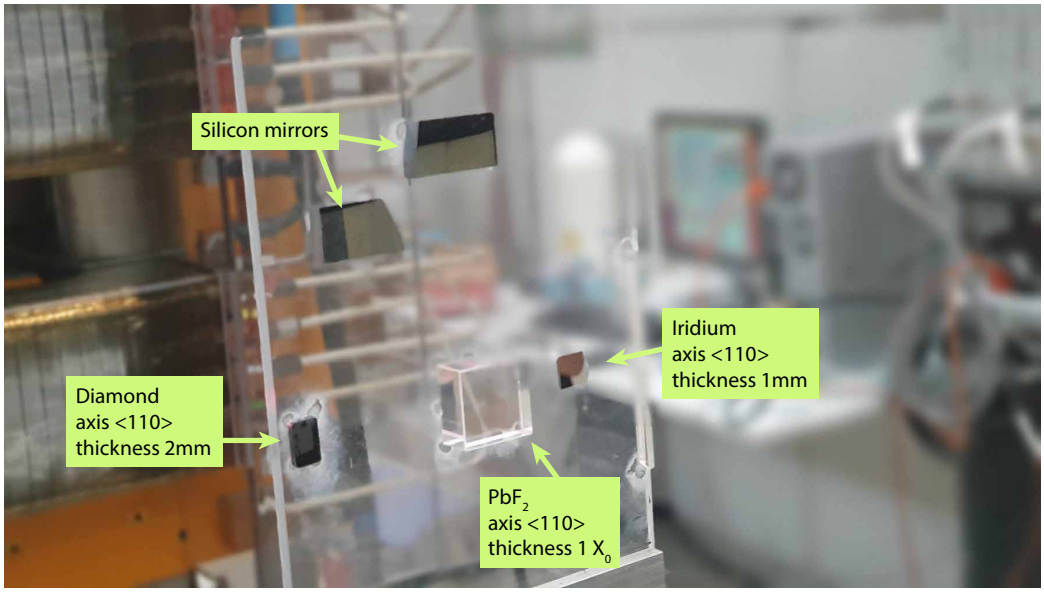

Figure 1.5: Plastic support where three different crystal samples are mounted. In the upper part two silicon mirrors are present to help in the alignment procedure.

are available at many facilities. Channelled electrons with $E = 10$ - $40\,\mathrm{MeV}/c$ can generate ChR of $\hbar\omega =$ 10 - 80 keV: it is therefore possible to consider this technique as a new X-ray light source [17].

Modern accelerators usually operate at a fixed value of E (or a discrete set): in order to make the CLS tunable, bent and especially periodically bent crystals may become the natural choice as they provide tunable emission in the gamma-ray range by varying the amplitude and the period of the bending [18].

1.1.3 Beam manipulation

Bent crystals may be used in a wide range of applications from *beam extraction*, as described in section 1.1.1, to the *focusing* of a parallel beam or the *defocusing* of a point like source into a parallel beam. Thanks to the small critical angle for high energy particles, it is possible to achieve a focussing high precision or deliver highly parallel beams. Focusing and defocusing can be achieved modifying the path length inside the crystal and therefore the deflection angle either with a precise face shaping (figure 1.6 a) or by imposing an angle (called *miscut angle*) between the surface and the particle beam (figure 1.6 b). With this technology a wide range of focal lengths can be obtained, from 10^{-1} to 10^{2} m [19].

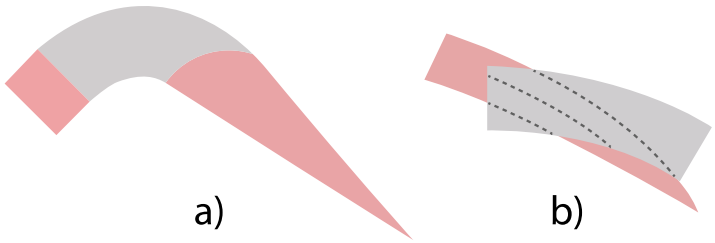

Figure 1.6: Beam manipulation techniques based on modifying the traveled path using bent crystals. The pink region is the beam and, depending on which are the incoming and outcoming directions, the crystal (grey region) is used to focus or defocus the beam. (a) The path length inside the crystal is modified working on the crystal shape. (b) In this case a careful choice of the *miscut angle* between the crystal surface and its planes provides a different path length. Image from [3].

Some of the advantages of a bent crystal approach consist in the high steering power without energy consumption and the small needed space.

The classical focussing approach is based on *quadrupole magnets*. Unlike dipole magnets, which produce a uniform field and can therefore only steer particle trajectories in the direction perpendicular with respect to the motion and the field ones, by arranging four bar magnets as in figure 1.7a, a quadrupole magnet is obtained. Figure 1.7b presents the magnetic field lines of an ideal quadrupole in the plane transverse to the nominal beam direction. The resulting field in the middle is null while, moving away from the center, the beam is focussed in one direction and defocussed in the perpendicular one. Another advantage of a bent crystal with respect to a quadrupole magnet approach is that there is no opposite effect in the orthogonal direction [3]. Figure 1.8 presents a photo of the QNL 427 quadrupole focussing magnet installed in the H8 beamline inside the PPE128 area at CERN [20] [21].

As a conclusion of the bent crystal application section, it is worth mentioning that they might be used for *beam collimation*. LHC plans to increase the number of protons per bunch up to 2.3×10^{11} during the High-Luminosity program, to be compared with the goal at the end of Run 3, which is 1.8×10^{11}. Thanks to the "slip stacking" implemented in the SPS accelerator, which consists in complex radio-frequency manipulations to shorten the bunch spacing of the LHC beam trains from 75 to 50 ns, the HL-LHC target has been reached already during Run 3 for lead ions [22].

Every particle beam has an intrinsic divergence, that is, particles moving in a direction different from the desired one. Collimation allows to remove these particles that form a dangerous halo around the main beam. When

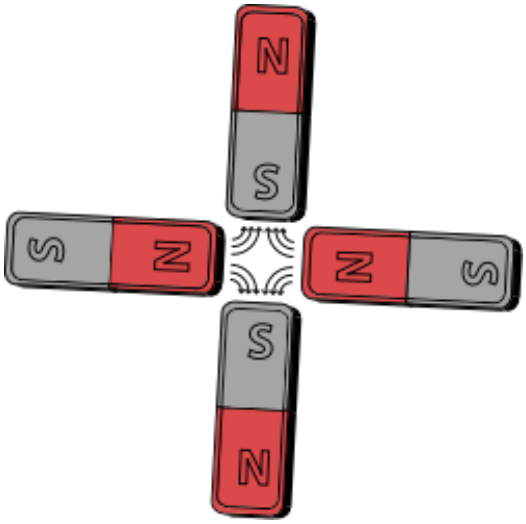

(a)

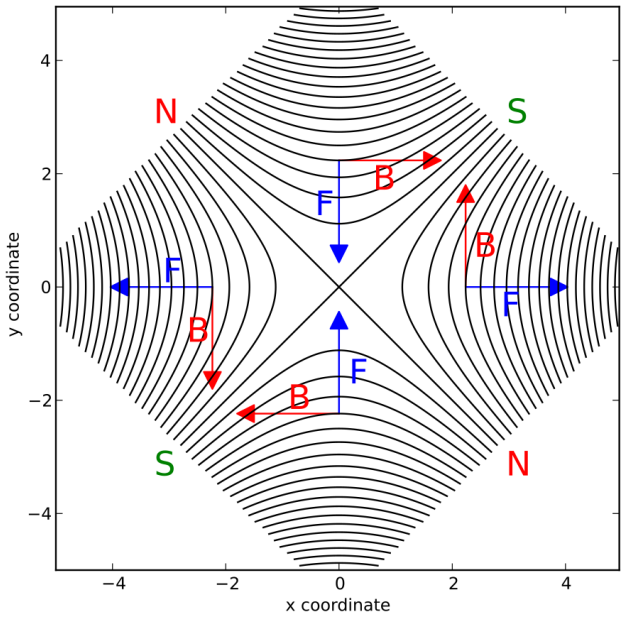

(b)

Figure 1.7: (a) Four bar magnets configured to produce a quadrupole. (b) Magnetic field lines of an ideal quadrupole in the plane transverse to the nominal beam direction. The red arrows show the direction of the magnetic field while the blue arrows indicate the direction of the Lorentz force on a positive charged particle going into the image plane. Images and captions from Wikipedia.

Figure 1.8: Photo of the QNL 427 quadrupole focussing magnet installed in the H8 beamline inside PPE128 at CERN.

operating the LHC as a heavy-ion collider, several unique challenges must be addressed. Magnetically, the machine behaves similarly to its operation during proton-proton collisions. However, due to the lower charge of lead-ion bunches (approximately 15 times less than protons), certain typical machine challenges, such as beam-beam interactions, impedance, electron-cloud effects, injection, and beam-dump protection, are somewhat reduced. On the other hand, addressing the challenges associated with beam halos becomes harder [22]. The LHC rings are equipped with more than 100 collimators to ensure that particles not following the desired trajectory, that is, with high divergence or with a different momentum, are cleaned by absorption, thus protecting sensitive superconducting and other accelerator components. The conventional LHC collimation system consists of 3 stages, designed to manage and control the intense particle beams circulating within its ring. The left part of figure 1.2 presents a sketch of the collimation hierarchy. In particular, the first stage intercepts and absorbs the stray particles. The second stage is employed to further clean the beam by removing the halo. Finally, the third stage is placed near the experimental regions to protect sensitive parts of equipment from radiation damage. This sophisticated collimation system enhances the overall performance and safety of the LHC, contributing to improve the quality of the collected data. A detailed description of the LHC collimation hierarchy may be found in [13].

Although the total beam energy is about 30 times lower for lead ion beams, a conventional multi stage collimator system (figure 1.2) is two order of magnitude less efficient with respect to a proton beam. This is related to the nuclear fragmentation process, which occurs when lead ions interact with conventional collimator materials producing ion fragments. These fragments might not have enough transverse kick to be sent onto the next collimator stage. For this reason, in IR7 there is the *betatron collimation system* capable of safely dispose such undesired particles. However, this creates a cluster of energy deposit near the region of the next superconducting dipole magnet, and can therefore increase the quenching probability, that is, the possibility that a magnet moves from the superconducting state to a resistive one.

Apart from these problems with ion beams, the standard collimation system has performed very well so far and provided adequate cleaning efficiency for the nominal LHC ion-beam parameters. But the situation will change with the HL-LHC: the magnet downstream of the betatron could receive an energy three times larger than its quenching limit[1]. A possibility might be to replace the existing 15 m long 8.5 T swiping magnet with two new smaller

[1]The quench occurs at a power load of $P_{\text{quench}} \approx 15\,\text{kW}$. Refer to [23] for a complete description of the quenching test.

dipole magnets with a higher magnetic field (11 T) that can fit in the same space. However, due to the unavailability of the new niobium-tin based dipole magnets, this intervention was deferred [24].

The bent crystal based approach (figure 1.9 a) is more compact and offers a much more precise control over the beam halo particles trajectory (instead of randomly scattering them away from the beam) reducing the number of produced secondary particles. In fact, particles follow the crystal geometrical shape and experience a net kick that can steer them with high efficiency to a downstream absorber.

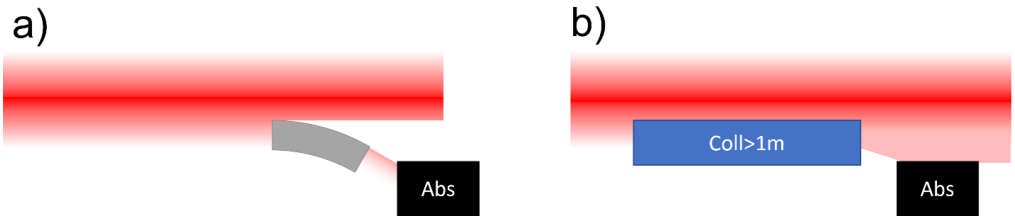

Figure 1.9: Collimation of the beam halo: approach based on oriented bent crystals (a) or on traditional jaws (b). Image from [3].

After years of dedicated R&D and beamtests on the SPS extracted beamlines at the CERN North Area, in 2015 the first prototype has been installed in the main LHC ring, and coherent effects at the record energy of 6.5 TeV have been observed [25].

LHC needs a total of four bent crystals to collimate both beams in the vertical and horizontal planes. During Run 2, 4 mm long silicon crystals with a bending angle of 50 µrad were installed in the betatron cleaning region to demonstrate that the crystal approach is a valid option. The equivalent kick would be the one provided by a 300 T magnet in the same volume occupied by the crystal. All the crystals are hosted in a vacuum tank (figure 1.10) and installed on a goniometer for adjusting their orientation remotely, with a precision of 1 µrad.

Some of the applications of bent crystals in particle Physics have been described up to here. In the following section an overview of the crystal Physics will be presented.

1.2 Crystallography and Crystal Structure

Crystals or crystalline solids are solid materials in which their microscopic constituents (either atoms, molecules or ions) are arranged in a highly ordered microscopic structure, forming a *crystal lattice* that extends in all directions.

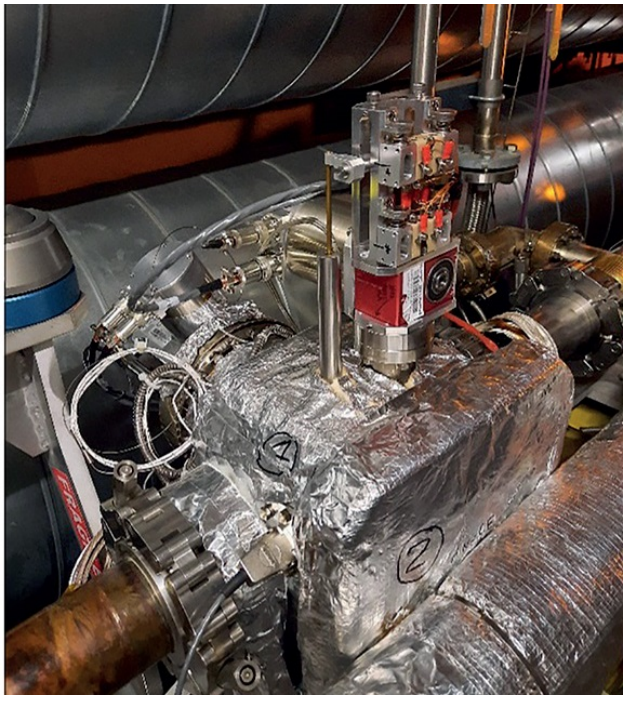

Figure 1.10: Photo of the vacuum tank that hosts a collimation crystal in the LHC ring and the system to control the crystal orientation. Image from [22].

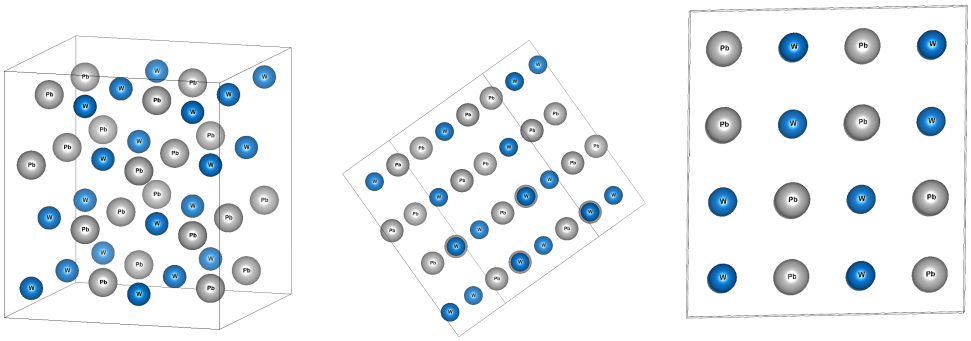

Figure 1.11: The lattice of a $PbWO_4$ crystal as seen by an external observer: randomly oriented (a), arranged in planes (b) or in strings (c). Image from [26].

A crystal is therefore the *periodic* repetition, along all the three spatial dimensions, of an elementary structure, called *crystal basis* [1].

Depending on the relative orientation between an observer and a crystal, the crystal itself may reveal or not its ordered structure; the former case is referred to as *oriented crystal*, while the latter as *amorphous*, *misaligned* or *randomly oriented* crystal. In the High Energy Physics (HEP) context, unless explicitly specified, the observer is assumed to be a particle beam. Figure 1.11 shows the lattice of a $PbWO_4$ crystal as seen by an external observer: randomly oriented (a), arranged in planes (b) or in strings (c) [26].

The periodicity of a crystal implies *invariance* under *spatial translation*, that is, any given lattice node might be obtained starting from a fundamental (primitive) block, identified by a set of three linear independent vectors $(\boldsymbol{a_1}, \boldsymbol{a_2}, \boldsymbol{a_3})$ and moving an integer number of times in any direction. If the fundamental block is placed in the axes origin and the crystal lattice extends toward the positive direction of all the axes, the position $\boldsymbol{r}$ of a generic node satisfies

$$\boldsymbol{r} = \sum_i n_i \boldsymbol{a_i} = n_1 \boldsymbol{a_1} + n_2 \boldsymbol{a_2} + n_3 \boldsymbol{a_3} \qquad \text{with } n_i \in \mathbb{N} \tag{1.1}$$

or in other terms, the positions $\boldsymbol{r}$ and $\boldsymbol{r'}$ of any pair of nodes satisfy

$$\boldsymbol{r} = \boldsymbol{r'} + n_1 \boldsymbol{a_1} + n_2 \boldsymbol{a_2} + n_3 \boldsymbol{a_3} \qquad \text{with } n_i \in \mathbb{Z} \tag{1.2}$$

The crystal lattice, also referred to as *Bravais reticulus*, is obtained by spanning all the possible values for n_i. In the three dimensional space there exist 14 different possible reticula, as presented in figure 1.12 [1].

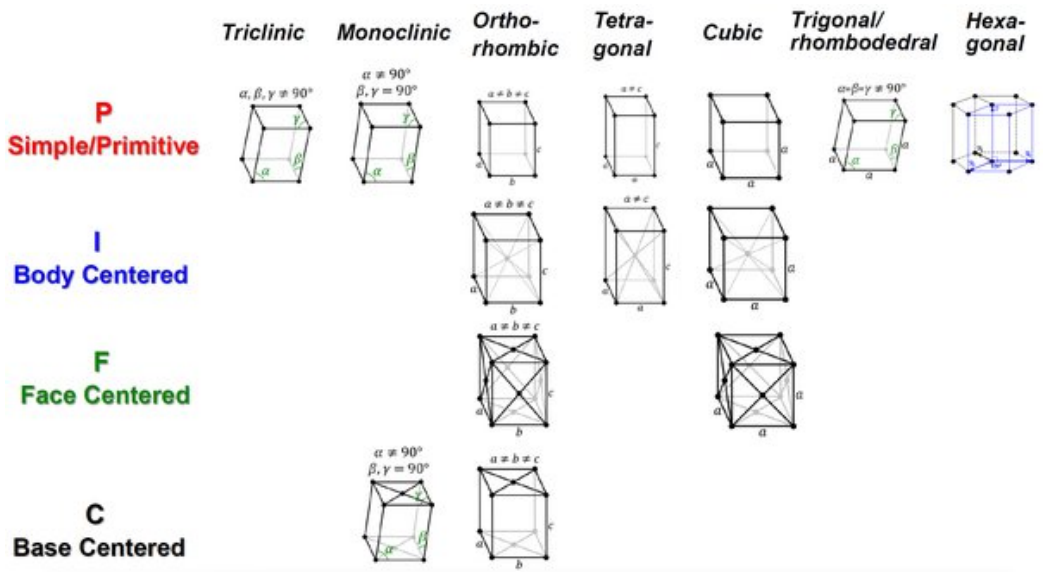

Figure 1.12: The 14 possible Bravais reticula in the three dimensional space. Image from [27].

A plane is a subset of nodes of great interest, because of the planar channelling phenomenon, introduced in section 1.1 and that will be described in detail in section 1.3.1. A plane may be described by the following equation

$$\frac{n_1}{n_1^0} + \frac{n_2}{n_2^0} + \frac{n_3}{n_3^0} = 1 \tag{1.3}$$

being n_i the node coordinates in units of the lattice primitive and n_i^0 the intersection between the plane and the axes. Provided that n_i are integer numbers, it is possible to define four integer numbers (n, h, k, l) such that

$$h \cdot n_1 = n \qquad k \cdot n_2 = n \qquad l \cdot n_3 = n \tag{1.4}$$

which allows equation (1.3) to be rewritten as

$$h \cdot n_1 + k \cdot n_2 + l \cdot n_3 = N \tag{1.5}$$

The three integer constants (h, k, l), not all zero at the same time and with no factors in common, are called *Miller indices* and are the components of a (not normalized) vector, orthogonal to the plane itself [28]. Another subset of nodes of interest is the axis or string. Miller indices are suited also for describing them. The *crystallographic notation* is a convenient way to use the same Miller indices to represent different objects [29]:

- $[hkl]$ represents a direction

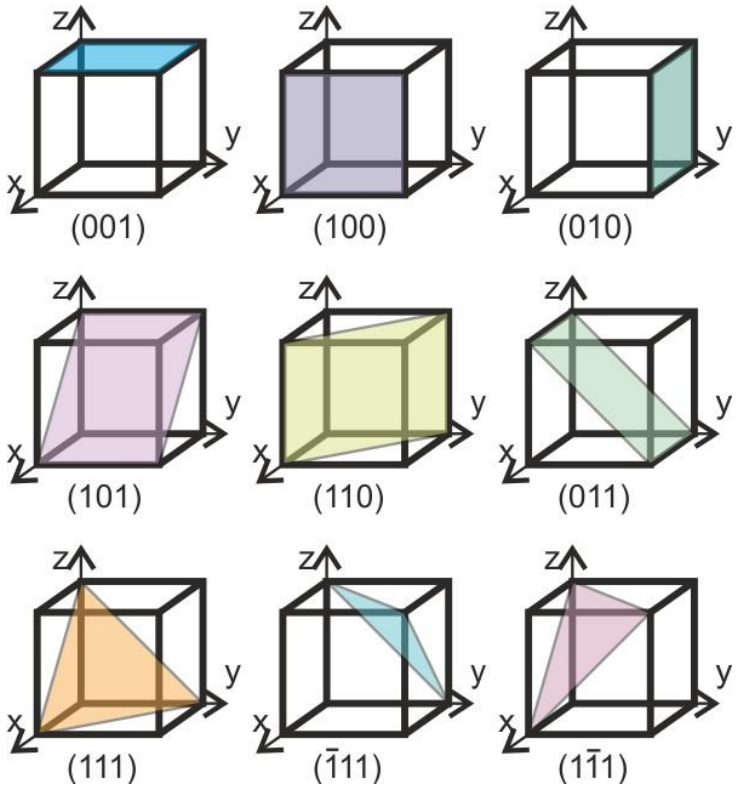

Figure 1.13: Miller indices for different crystallographic planes. Such indices are the components of a (non normalized) vector orthogonal to the surface. A negative value $-h$ is represented as $\bar{h}$.

- $\langle hkl \rangle$ represents a set of directions, that is all the $[hkl]$ equivalent directions under the symmetry group of the crystal. For instance, in a cubic crystal the $\langle 100 \rangle$ directions are [100], [010], [001], $[\bar{1}00]$, $[0\bar{1}0]$ and $[00\bar{1}]$

- (hkl) represents a plane

- $\{hkl\}$ represents a set of all the planes equivalent under the symmetry group of the crystal, as for $\langle hkl \rangle$ in the direction case.

In non-cubic crystals, the $[hkl]$ direction is generally not orthogonal to the (hkl) plane. Sometimes, it is convenient to specify directions in terms of perpendicular planes. It is allowed to refer to a "(hkl) direction" or a "hkl direction", provided that the specification is explicitly detailed. Figure 1.13 presents a few examples of such planes.

1.3 Planar Channelling in Bent Crystals

1.3.1 The Channelling Phenomenon

The crystal lattice was first observed thanks to X-rays on July 30$^{\text{th}}$ 1913 [2] exploiting the phenomenon of *diffraction*, which is impossible in an amorphous medium (i.e. without an ordered periodic structure). Since then, many new directional effects have been theorized and studied: among these *channelling*, a phenomenon that affects the motion of a charged particle travelling in close alignment with an atomic plane (*planar channelling*) or axis (*axial channelling*).

In 1912 Stark predicted the existence of "*easy passages*" [30] for ions along *open channels* in the crystal lattice: this effect was named *channelling* [31]. For over half a century, this effect has been overlooked until computer simulations of radiation-crystal interactions uncovered evidence of comparable features [32] [30]. The theoretical description of the phenomenon dates back to 1964 when Lindhard published a comprehensive theoretical study on the "Influence of Crystal Lattice on Motion of Energetic Charged Particles" [33], where the concept of *continuum potential* was introduced to describe the interaction of a particle with the whole set of crystal atoms. In the following sections, an overview of Lindhard's mathematical formalism will be presented; for a detailed description of the topic, the reader can refer to [33] [34] and [35].

1.3.2 The Continuum Description

Directional effects in aligned crystals appear because of the correlation between successive soft collisions of an impinging charged particle with the target constituents.

In his work Lindhard focussed mainly on axial effects, although the description can be generalized to include planar ones. Figure 1.14 presents the sketch of an axially aligned cubic crystal.

For a heavy positive charged particle moving at a non-relativistic energy, the interaction between the particle itself and each single crystal atom is governed by a *screened Coulomb potential*: the screening is provided by the electron cloud surrounding the nuclear charge. The single collision angular deflection $\Delta\psi$ is small compared to the total deflection. When a particle passes close to an atom experiencing only a slight deflection, it must also pass close to the next atom in the string. Provided that the interaction distance is typically an order of magnitude smaller than the string interspacing, collisions occur with just one string at a time, at least at the lowest order approximation. Since the deflection in each collision is small, the trajectory between two

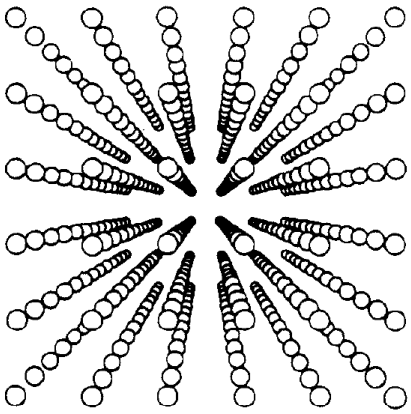

Figure 1.14: Sketch of an axially aligned cubic crystal. Image from [34].

consecutive collisions might be approximated as a straight line. Therefore the momentum transfer associated with all the collisions is orthogonal to the direction of motion, which in turn can be approximated to be $\hat{\boldsymbol{z}}$, the direction of the string, that is

$$\Delta \boldsymbol{p} \simeq -\frac{1}{v} \int_{-\infty}^{+\infty} dz \, \boldsymbol{\nabla}_{\boldsymbol{r}_\perp} V\left(\boldsymbol{r}_\perp, z\right) \tag{1.6}$$

being $\boldsymbol{r}_\perp$ the coordinate transverse to the string and v the incoming particle speed. V is the particle-atom interaction potential (or energy). Starting from equation (1.6), the momentum transfer due to a single scattering event might be computed, integrating over the transit time $\Delta t = d/v$ (where d is the spacing between the atoms in a string) the force obtained from the potential

$$U\left(\boldsymbol{r}_\perp\right) = \frac{1}{d} \int_{-\infty}^{+\infty} dz \, V\left(\boldsymbol{r}_\perp, z\right) \tag{1.7}$$

The potential (1.7) corresponds to a charge uniformly distributed along the z direction.

The motion of a charged particle impinging with a small angle with respect to a crystal string is governed by a two-dimensional continuum potential, obtained by smearing the total screened nuclear charge along the z direction [34]. Figure 1.15 shows the deflection of a charged particle by an atomic string in the true discrete case (a) and in the continuum approximation (b).

The so called *standard expression* is usually adopted for the screened Coulomb potential:

$$V\left(r\right) = \frac{Z_1 Z_2 e^2}{r} \left[1 - \frac{r}{\left(r^2 + C^2 a^2\right)^{1/2}}\right] \tag{1.8}$$

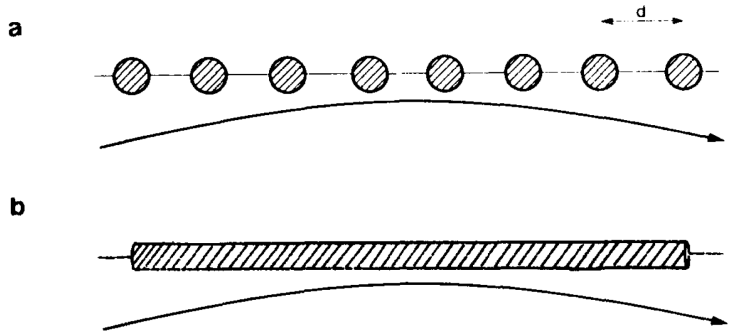

Figure 1.15: Deflection of a charged particle impinging with a small angle with respect to a crystal string in the true discrete case (a) and in the continuum approximation (b). d is the spacing between the atoms in a string. Image from [34].

where $Z_1 e$ and $Z_2 e$ denote respectively the particle and nuclear electric charge, C^2 is a constant normally fixed at 3, and a is the *screening length*, defined as

$$a = 0.89\, a_0 \left(Z_1^{2/3} + Z_2^{2/3} \right)^{-1/2} \tag{1.9}$$

where a_0 is the Bohr radius for the hydrogen atom.

By plugging equation (1.9) into equation (1.7), the standard continuum potential corresponding to one single crystal string is obtained:

$$U\left(\boldsymbol{r}_\perp\right) = \frac{Z_1 Z_2\, e^2}{d}\, \ln\left[1 + \left(\frac{C_a}{\boldsymbol{r}_\perp}\right)^2\right] \tag{1.10}$$

The finite positive temperature introduces an uncertainty in the atom position due to *thermal vibrations*, which implies a *transverse* smearing in addition to the already discussed *longitudinal* smearing.

The *harmonic approximation* consists in considering the probability distribution $P\left(\boldsymbol{r}_\perp\right)$ of finding an atom in the $\boldsymbol{r}_\perp$ position in the transverse plane to be Gaussian, that is

$$P\left(\boldsymbol{r}_\perp\right) = \frac{1}{\pi \rho^2}\, e^{-{\boldsymbol{r}_\perp}^2/\rho^2} \tag{1.11}$$

being ρ the two-dimensional mean square thermal displacement from the string. The continuum potential in the axial case is the convolution between equation (1.7) and the Gaussian distribution (1.11):

$$U_T\left(\boldsymbol{r}_\perp\right) = \int d^2\boldsymbol{r}_\perp\, P\left(\boldsymbol{r}_\perp\right)\, U\left(\boldsymbol{r}_\perp - \boldsymbol{r}_\perp{}'\right) \tag{1.12}$$

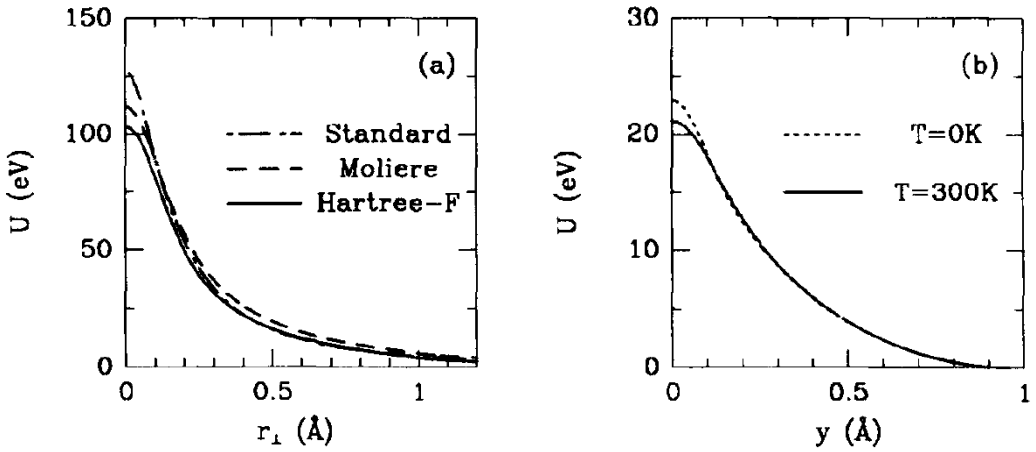

Figure 1.16: Plots of continuum potentials ($Z_1 = 1$). (a) Axial potential for <111> silicon at room temperature. The standard potential (1.13) is compared with other models found in literature [36]. (b) Thermally averaged planar potential for {110} silicon with the inclusion of the nearest neighbor planes contribution. Image from [34].

From now on, all the potentials will be thermally averaged, unless explicitly stated. Therefore, dropping the T subscript and making the quantities inside the integral explicit, a simple approximation for the thermally averaged standard potential of a single continuum string is obtained:

$$U_T(\boldsymbol{r}_\perp) = \frac{Z_1 Z_2\, e^2}{d} \ln\left(1 + \frac{C^2 a^2}{r_\perp^2 + \frac{1}{2}\rho^2}\right) \tag{1.13}$$

A similar calculation might be worked out to obtain the *standard continuum potential for a single static plane*. Defining y as the particle-plane distance and d_p the distance between two consecutive planes inside the crystal, the analytical expression assumes the following form:

$$U(y) = 2\pi Z_1 Z_2\, e^2 n d_p \left[\left(y^2 + C^2 a^2\right)^{1/2} - y\right] \tag{1.14}$$

Also in this case a thermal average should be considered, which is known as *Hartree-Fock* potential [36]. However in the planar case the smearing effect is less relevant, since the potential remains finite when evaluated in the plane position ($y = 0$). Figure 1.16 presents the potentials derived in this section compared with other models found in literature [36] for a silicon crystal. It is worth to note the potentials height and width: in the axial case the former is a factor 5 higher and the latter about a factor 2 wider.

1.3.3 Particle Motion in the Continuum Approximation and Critical Angle

The particle-string interaction potential (1.7) is independent on z, hence there is a complete *separation* between the longitudinal and transverse motion. The former is that of a free particle that proceeds with momentum $p_z = \boldsymbol{p}\hat{z}$ which is a constant of the motion. The translational energy E_z associated to the longitudinal motion is also constant, and it is defined as

$$E_z = \frac{p_z^2}{2M} \tag{1.15}$$

where M is the mass of the impinging particle. On the other hand, the transverse motion is governed by the potential (1.7) of the whole lattice.

Considering that also the total energy of the particle is conserved (no external force fields are present), it is found that also the *transverse energy* $E_\perp$ is a constant of motion:

$$E_\perp \equiv E - E_z = \frac{p_\perp^2}{2M} + U\left(\boldsymbol{r}_\perp\right) \tag{1.16}$$

Since E is typically orders of magnitude greater than U, the local angle with respect to the continuum string is $\psi \ll 1$, and therefore

$$p_\perp^2 = p^2 \sin^2\psi \approx p^2\psi^2 = p\, Mv\, \psi^2 \tag{1.17}$$

which yields

$$E_\perp \approx E\psi^2 + U\left(\boldsymbol{r}_\perp\right) = \frac{1}{2}pv\psi^2 + U\left(\boldsymbol{r}_\perp\right) \tag{1.18}$$

where it can be noted that $E_\perp$ has two components: the kinetic energy associated to the transverse motion and a potential term describing the interaction of the particle with a string.

The theory can be extended to the regime of relativistic impact energies, where the impinging particle velocity v approaches the speed of light c: the energies E and E_z are replaced with their relativistic expressions leaving everything unchanged, with the exception of the introduction of the relativistic mass γM, where γ is the usual Lorentz factor:

$$\gamma = \sqrt{\frac{1}{1 - \frac{v^2}{c^2}}} \tag{1.19}$$

The transversal energy becomes

$$E_\perp = \frac{p_\perp^2}{2\gamma M} + U\left(\boldsymbol{r}_\perp\right) \tag{1.20}$$

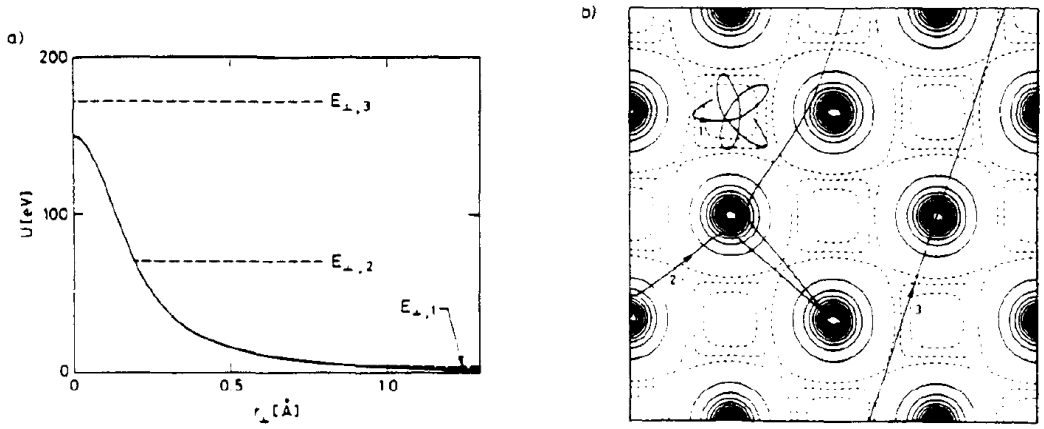

Figure 1.17: Sketch of the transverse motion for different values of $E_\perp$ in a <100> germanium. (a) The potential of a single string and the three chosen energies. (b) Contour plot of the full potential with the trajectories corresponding to the three different energies superimposed. Image from [34].

One way to observe directional effects, that is, channelling, is to consider the yield of a process which requires a close contact on the atomic scale between the particle and the target nuclei. Figure 1.17 shows a sketch of the transverse motion for three different values of the transverse energy $E_\perp$ with respect to the height of the string potential barrier. If $E_\perp \ll U(0)$ ($E_{\perp,1}$ in figure 1.17), the particle is trapped at the bottom of the potential well and follows a highly localized orbit, known as *Rosette orbit*. This condition is also known as *hyper channelling* [37]. If the particle moves with a transverse energy greater than the maximum of the potential ($E_{\perp,3}$ in figure 1.17), it is free to move above the potential barrier and hits the crystal atoms as in an amorphous (random) medium. The critical value for directional effects to happen is thus of the order of $U(0)$; to take into account that the atoms can be met off their average position ($\boldsymbol{r}_\perp = 0$) due to thermal fluctuations, the slightly lower $U(\rho)$ value might be adopted.

Moving away from the string, the transverse energy has only the kinetic component $E_\perp \approx \frac{1}{2}pv\psi^2$, where ψ is the angle of the impinging particle with respect to the string direction. The *characteristic angle* is given by

$$\psi_c \approx \sqrt{\frac{U(\rho)}{\frac{1}{2}pv}} \tag{1.21}$$

and for any reasonable choice of potentials it approximates the Lindhard

angle ψ_1 (often called *critical angle* θ_c)

$$\psi_c \approx \psi_1 \equiv \sqrt{\frac{4Z_1 Z_2 e^2}{pvd}} \tag{1.22}$$

The critical angle for planar effects might be obtained in the same way:

$$\psi_p = \sqrt{\frac{4Z_1 Z_2\, e^2\, n d_p\, Ca}{pv}} \tag{1.23}$$

The planar continuum potential is shallower than the one for the axes, as might be seen in figure 1.16, resulting in smaller critical angles: typically, $\psi_p \sim \psi_1/3$.

To summarize, channelling occurs when a charged particle impinges onto the crystal with an angle with respect to a crystal plane or axis smaller than the critical angle. Once into the channelling condition, the particle gets confined by the continuum potential and keeps travelling following the crystal planes/axes. Calculations, simulations and measurements show that the typical energy of the potential well is of the order of 10^1 - 10^2 eV while the width is comparable to the interatomic distance in solids (10^{-10} m) [3]. Figure 1.18 presents a positive charged channelled particle oscillating in a potential well defined by the crystal planes.

Even if experiments are in good agreement with this theoretical description, given the fact that some approximations have been made, some discrepancies may naturally arise. It is important in fact to consider that the conservation of $E_\perp$ is not exact: the impinging particle has a chance to scatter on point-like charges, either an electron or a thermally displaced nucleus. This is equivalent to say that the continuum potential is not exactly the superposition of a Coulomb potential for each point-like charge, and this difference perturbs the particle motion as determined by the continuum potential. In any case, the net effect is that $E_\perp$ increases when a particle crosses a crystal.

So far only positive charged particles have been considered. Channelling exists also for negative ones: the potential has the same shape but with an overall minus sign, which causes the minimum to be at the center of the string or plane, as depicted in figure 1.19. The channelling region (hatched region in figure 1.19) for negative particles is narrower. Negative particles are thus focussed close to the nuclei, increasing the dechannelling probability, that is, the possibility for a channelled particle to lose the channelling condition and return to move in an amorphous medium. This is why the natural choice is to perform beamtests with positive charged particles.

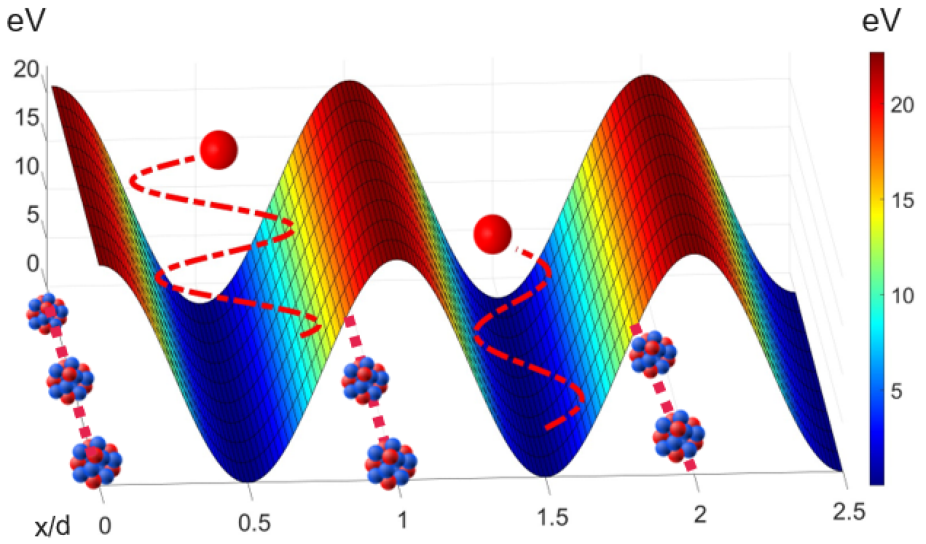

Figure 1.18: Continuum potential generated by atomic planes (surface plot) with a confined positive charged channelled particle (red). The potential shows maxima at the nuclei position, letting the positively charged particles oscillate between two adjacent planes while crossing the crystal. The horizontal axis is the coordinate x normalized by the distance d between two adjacent planes; the y axis is the direction parallel to the lattice plane. Image from [3].

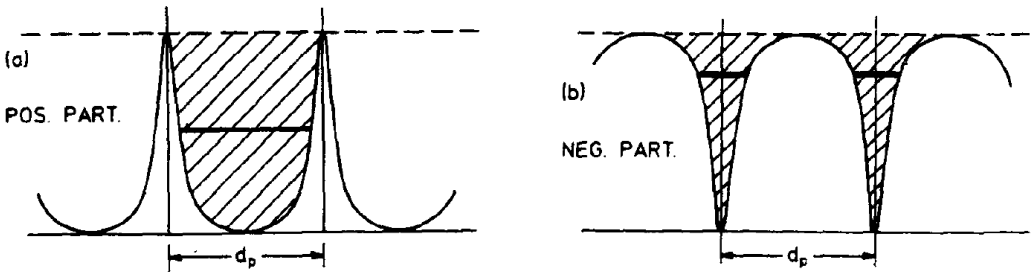

Figure 1.19: Sketch of the planar continuum potential for positive charged (a) and negative charged (b) particles. Image from [34].

1.3.4 Bent Crystals

An interesting effect might be observed when a crystal is curved along the direction of motion of the impinging particles. Indeed a channelled particle, being bounded, keeps travelling parallel to the planes/axes, resulting in the outgoing direction being different from the incoming one (figure 1.4). By exploiting this effect, deflections comparable to the ones reachable with hundreds of Tesla dipoles can be obtained with just a few millimeters in the beam direction bent crystals.

To take into account the curvature of the crystal, an additional *centrifugal force* term might be added to the continuum potential:

$$U_{\text{bent}}(x) = U_{\text{flat}}(x) + \frac{pv}{R}\,x \tag{1.24}$$

being $U_{\text{bent}}(x)$ and $U_{\text{flat}}(x)$ the continuum potentials in the *bent* and *flat* case respectively, x the direction orthogonal to the lattice planes and R the *curvature radius*.

A direct consequence of the centrifugal term is the existence of a maximum curvature radius; for the planar channelling it can be estimated as

$$R_{\text{c}} = \frac{pv}{U'_{\text{max}}} \tag{1.25}$$

where R_{c} is the critical curvature radius and U'_{max} the maximum electric field value in the potential well.

The asymmetry caused by the bending may result in the crystal acting as a mirror, reflecting an incoming particle in the opposite direction with respect to a channeled particle. This happens to particles not aligned to the potential wells, therefore, travelling over the barrier (figure 1.20) in the medium until they reach a tangency point to a plane and are deflected by a value of the order of twice the critical angle. This is the so called *volume reflection*, first theorized [38] and then observed in [39]. Table 1.1 summarizes the angular acceptance and the deflection angles of the volume reflection and channelling effects.

The last effect presented in figure 1.20 is the *volume capture* effect which consists in a particle impinging with an angle larger than the critical one which gets trapped in channelling in the volume of the crystal.

All these effects can be studied experimentally tracking each incoming and outgoing particle with high resolution detectors such as silicon microstrip detectors. Figure 1.21 presents the plot of the particle orientation with respect to the crystal as a function of the deflection angle. Six different regions might be identified:

Table 1.1: Angular acceptance and deflection angle for the channelling and volume reflection phenomena; θ_C is the critical angle, R is the curvature radius. Table from [3].

	Channelling	Volume Reflection
Angular acceptance	θ_C	$1/R$
Deflection angle	$1/R$	$\approx 2\theta_C$

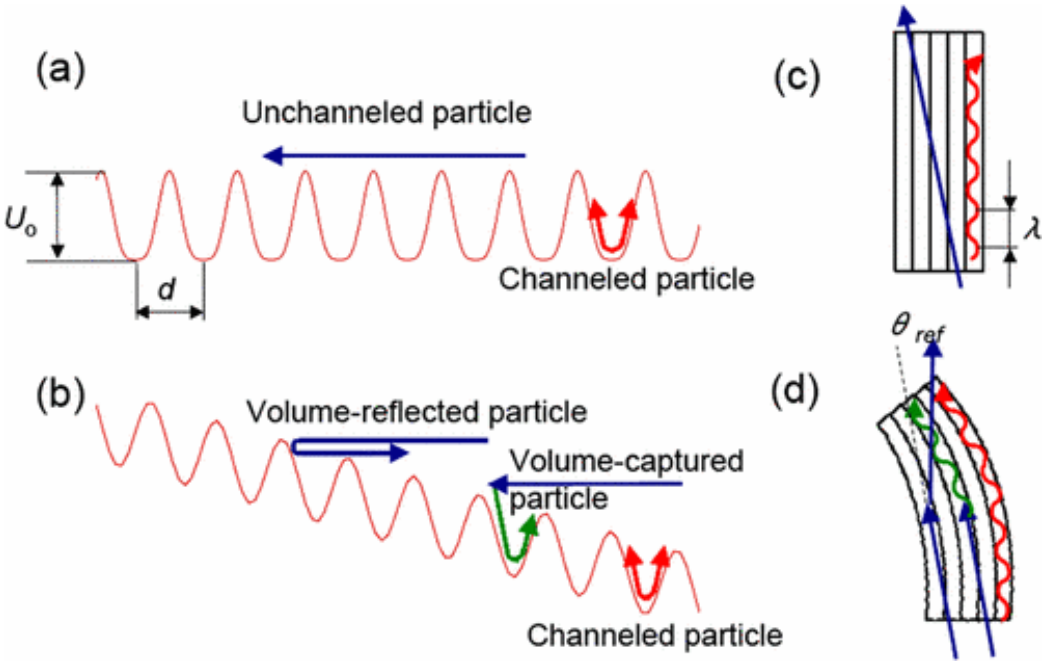

Figure 1.20: (a) Periodic potential in a *planar crystal*. The red arrow shows a channelled particle oscillatory motion in the potential well, while the blue one an unchannelled particle, with a transverse energy greater than the depth of the potential well U_0. (b) Same situation but for a *bent crystal*. Volume capture (green arrow) and volume reflection (blue arrow on the left) are now possible. The pictures on the right show the particle trajectories in a straight (c) and bent (d) crystal. Image from [40].

(1) and (6) not oriented (amorphous) crystal: incoming particles are not deflected (the deflection angle distribution is centered on 0) for impinging angles much larger than the channelling one. The spread in the deflection angle (i.e. the width of the deflection angle region) is the result of the convolution between the intrinsic divergence of the beam (which is of the order of 10 µrad) and the multiple scattering in the crystal medium.

(2) Channelling: for incident angles smaller than the critical angle, a large deflection angle is observed, which depends on the curvature radius.

(3) Dechannelling: particles entering the crystal in the channelling condition can lose this condition inside the crystal itself, thus being deflected by a smaller angle with respect to the channelling one.

(4) Volume reflection: for impinging angles within the $1/R$ range, that is, the angular acceptance for this effect, particles may be deflected in the opposite direction with respect to the channelled ones, with an efficiency of the order of 100 %.

(5) Volume capture: a small fraction of the particles impinging within the volume reflection same range, might be trapped in channelling inside the crystal and exit the crystal in the same direction of the channelled ones, but with a smaller deflection angle.

By examining the plot in figure 1.21, the *wider angular acceptance* of *volume reflection* (4) compared to channelling (2) may be seen. A particle is considered as reflected when its angle with the incident beam axis is $\theta_{\text{def}} > \theta_{\text{VR}} - 3\sigma_{\text{VR}}$, being θ_{VR} and σ_{VR} the mean and the standard deviation of the peak of the reflected beam; the volume reflection efficiency was estimated to exceed 95 %, while the channelling efficiency was only 55 %. Examining the color scale, it is evident that volume capture (5) represents a small fraction of events within the same range of impinging angles in comparison to volume reflection (4). However, this *diagonal feature* plays a crucial role in interpreting such plots as it can be "*followed*" to identify the channelling position.

1.4 A Glimpse on Radiation Production in Oriented Crystals

As already introduced in section 1.1.2, it is well known from classical electrodynamics that a charged particle, when accelerated, emits electromagnetic radiation [41]. The emitted power per unit of time P is proportional to

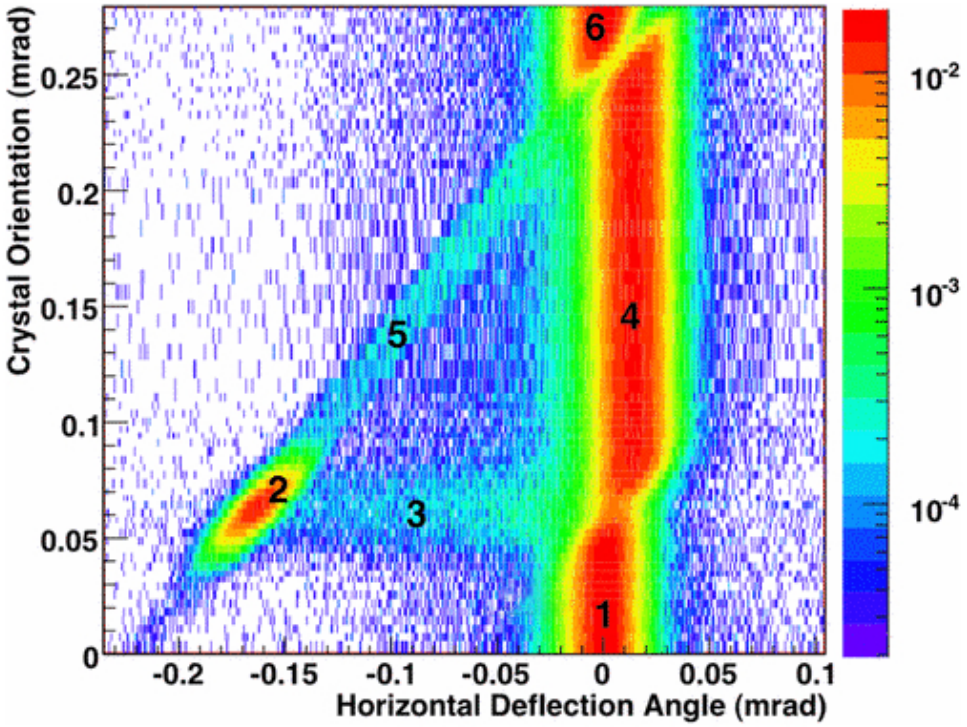

Figure 1.21: Plot of the particle orientation with respect to the crystal as a function of the deflection angle. (1-6) non oriented crystal; (2) channelling; (3) dechannelling; (4) volume reflection; (5) volume capture. Image from [40].

the square root of the acceleration. From the second principle of dynamics, $a = F/M$ being F the force acting on the particle. Therefore $P \propto (F/M)^2$, which in the relativistic case becomes $P \propto (\gamma F/M)^2$. This result implies that only the lightest particles, namely electrons and positrons, are of pratical interest for the radiation production in crystals. A complete overview may be found in [17] and [42], while [34] offers a concise but rather complete theoretical description, which will be taken as a template for the rest of this section.

1.4.1 Quantum Description

A classical approach has been used up to here. To judge whether or not a quantum mechanical treatment is necessary to describe the channelling phenomenon, the number of quantum states ν corresponding to a bound transverse motion might be calculated. The classical description of channelling can be applied when the discrete quantum spectrum of quantum states becomes dense, providing a reliable approximation for the quantum behavior.

A possible estimation of ν is the number of cells of volume h^2 (axial channelling) or h (planar channelling) in the classically available phase space such that $e_\perp < \max\left[U\left(\boldsymbol{r}_\perp\right)\right]$. Without describing the technical calculation (the full calculation might be found in [17]), the result for a negative charged particle is

$$\text{string:} \qquad \nu \sim |Z_1| \frac{\gamma M}{m} \tag{1.26}$$

$$\text{plane:} \qquad \nu \sim \left(|Z_1| \frac{\gamma M}{m}\right)^{1/2} \tag{1.27}$$

For positive charged particles the scaling is the same, but having more available space, the absolute values are larger.

From equations (1.26) and (1.27) it is clear that the number of bound states for the transverse motion is large at all energies for heavy charged particles ($M \gg m$). A quantum description might be required only for electrons/positrons, although at GeV energies where $\gamma M/m = \gamma \gg 1$ it is not necessary.

The motion of a quantum relativistic electron is described by the Dirac equation; however, as far as channelling is concerned, the much simpler Klein-Gordon equation might be used as long as spin effects turn out to be negligible. The reader can refer to the appendices of [43] for an overview of these equations or [44] for a more complete description.

From the wave function Ψ of a channelled electron, a rapid oscillating e^{ikz} term associated to the uniform motion in the channelling direction with

energy E can be extracted, that is

$$\Psi\left(\boldsymbol{r}_{\perp}, z\right) \equiv e^{ikz}\, w\left(\boldsymbol{r}_{\perp}, z\right) \tag{1.28}$$

where

$$E^2 = (hkc)^2 + m^2c^4 \tag{1.29}$$

In the limit of small angle scattering, the stationary Klein-Gordon equation for the whole wave function Ψ reduces to a Schrödinger-like equation for the w term

$$i\hbar \frac{\partial}{\partial t} w\left(t, \boldsymbol{r}_{\perp}\right) = H w\left(t, \boldsymbol{r}_{\perp}\right) \tag{1.30}$$

where the time-like coordinate is defined as $t = z/v$ and the Hamiltonian operator H is defined as

$$H\left(\boldsymbol{r}_{\perp}, t\right) = -\frac{\hbar^2}{2m\gamma} \nabla^2_{\boldsymbol{r}_{\perp}} + V\left(tv, \boldsymbol{r}_{\perp}\right) \tag{1.31}$$

By approximating the whole crystal potential $V\left(tv, \boldsymbol{r}_{\perp}\right)$ with the thermal averaged continuum potential $U\left(\boldsymbol{r}_{\perp}\right)$, the solutions of equation (1.30) assume the form

$$w\left(t, \boldsymbol{r}_{\perp}\right) = u\left(\boldsymbol{r}_{\perp}\right)\, e^{-iE_{\perp}t/\hbar} \tag{1.32}$$

where $u\left(\boldsymbol{r}_{\perp}\right)$ are eigenfunctions of H, that is, solutions of the stationary (time independent) Schrödinger-like equation:

$$\left[-\frac{\hbar^2}{2m\gamma} \nabla^2_{\boldsymbol{r}_{\perp}} + U\left(\boldsymbol{r}_{\perp}\right)\right] u\left(\boldsymbol{r}_{\perp}\right) = E_{\perp} u\left(\boldsymbol{r}_{\perp}\right) \tag{1.33}$$

Equation (1.33) is the quantized counterpart of equation (1.20).

The eigenvalues problem can be solved for a plenty of scenarios, but it is quite irrelevant for the purposes of this thesis. It may be worth to note that for an isolated string the potential is rotationally symmetric $U = U\left(r_{\perp}\right)$ and the eigenfunctions $u\left(\boldsymbol{r}_{\perp}\right)$ can be expressed in polar coordinates $(r_{\perp}, \varphi)$ as

$$u\left(\boldsymbol{r}_{\perp}\right) = R_{nl}(r_{\perp})\, \frac{1}{2\pi}\, e^{\pm il\varphi} \qquad \text{with } l = 0, 1, 2, \ldots \tag{1.34}$$

where n is the principal quantum number and $R_{nl}(r_{\perp})$ the radial term. In this approximation the electron density

$$|u|^2 = \frac{R^2}{2\pi} \tag{1.35}$$

is angle independent. Methods for including the four nearest neighbor strings can be found in literature.

1.4.2 Bremsstrahlung

By using a quantum model, the differential cross section for photon emission at energy $\hbar\omega$ by a relativistic electron or positron[2] of energy E, in the Born approximation, may be approximated by the *Bethe-Heitler cross section* [45] [46]:

$$\frac{d\sigma}{d\hbar\omega} = \frac{16}{3} Z^2 \alpha r_e^2 \frac{1}{\hbar\omega} \left[1 - \frac{\hbar\omega}{E} + \frac{3}{4} \left(\frac{\hbar\omega}{E} \right)^2 \right] \ln\left(183\, Z^{-1/3}\right) \tag{1.36}$$

where $r_e = e^2/mc^2 = \alpha^2 a_0$ is the classical electron radius, α the fine structure constant and $Z \equiv Z_2$. This result holds in the limit $\gamma \gg 1$ that is when the atomic screening is complete (this is the statistical Thomas-Fermi model [47] [48]), otherwise the argument of the logarithm has to be slightly modified. The result can be used also for moderate γ values for the so called *soft photons*, that is $\hbar\omega/E \ll 1$. The cross section (1.36) describes the radiation emitted as a result of a scattering event in the screened nuclear field. Radiation may be emitted also due to a direct scattering event with an electron: this leads to an extra contribution which is $1/Z$ times the nuclear one. For very light targets ($Z \lesssim 5$), the screening is described more accurately than by the Thomas-Fermi model.

High-energy electrons ($\gtrsim 1\,\mathrm{GeV}/c$ for most materials) predominantly lose energy in matter via bremsstrahlung. It is convenient to introduce the *radiation length* X_0, defined as the mean distance over which a high-energy electron loses all but $1/e$ of its energy via bremsstrahlung [49]. In literature, there are practical calculation approximations available, and for most materials, these calculations have been meticulously performed and tabulated [49] [50].

1.4.3 Coherent Bremsstrahlung

When an electron impinges onto a crystal in a direction close to a major crystallographic axis or plane, it is likely to scatter coherently on many atoms along its way, as already described for the channelling. The coherence in the scattering has an effect on the radiation emission: when in channelling condition, the radiation emission can significantly exceed the bremsstrahlung emission of the non oriented material. This is the so called *coherent bremsstrahlung*.

[2] All the considerations and results in this section are valid both for electrons and positrons, unless explicitly pointed out. Therefore the term *electron* will be used to refer to both of them.

In this subsection an overview of the emission process is presented. The interaction of the impinging particle both with the radiation field and the atoms might be described under the Born approximation, a perturbation technique which consists of considering the incident field instead of the total field as the driving field at each point in the scatterer.

In the perturbation limit, the bremsstrahlung emission probability is proportional to the square of a second-order matrix element, which, in turn, is a sum of terms, each one proportional to a first-order matrix element, one for the interaction with the radiation field and the other for the interaction with the nuclei. Since the particle states are described by plane waves, this yields for a single crystal atom

$$d\sigma \propto \left| \int V(r)\; e^{i\boldsymbol{qr}}\, d^3\boldsymbol{r} \right|^2 \tag{1.37}$$

where V is the atomic potential and $\hbar\boldsymbol{q}$ the recoil momentum of the nucleus. A crystal is made of N atoms: the potential has therefore to be replaced with the total interaction potential

$$V \mapsto \sum_{n=1}^{N} V(\boldsymbol{r} - \boldsymbol{r_n}) \tag{1.38}$$

where $\boldsymbol{r_n}$ denotes the position of the n-th atom.

Since the electrons inside the crystal play only the role of screening the nuclear charge, boundary effects from the mutual atom-atom interactions which would lead to changes in the potential form may be ignored when applying equation (1.38).

Substituting equation (1.38) into equation (1.37), the following relation for the differential cross section for the production of photons with an energy $\hbar\omega$ is obtained:

$$\left.\frac{d\sigma}{d\hbar\omega\, d^3\boldsymbol{q}}\right|_{\text{N atoms}} = \left.\frac{d\sigma}{d\hbar\omega\, d^3\boldsymbol{q}}\right|_{\text{single atom}} \times \left| \sum_{n=1}^{N} e^{i\boldsymbol{qr_n}} \right|^2 \tag{1.39}$$

The last term yields simply N for an amorphous medium. On the other hand, for a perfect static crystal, in the limit $N \to \infty$ equation (1.39) becomes

$$\left| \sum_{n=1}^{N} e^{i\boldsymbol{qr_n}} \right|^2 = N\, \frac{(2\pi)^3}{N_0 \Delta}\; |S(\boldsymbol{g})|^2 \sum_{\boldsymbol{g}} \delta(\boldsymbol{q} - \boldsymbol{g}) \tag{1.40}$$

where $\boldsymbol{g}$ is a reciprocal lattice vector, $S(\boldsymbol{g})$ the structure factor and N_0 the number of atoms contained in the unit cell with volume Δ.

The solid line in figure 1.22 presents the spectrum generated by a 10 GeV/c electron beam impinging on a $\langle 110 \rangle$ germanium at 1 mrad with respect to the axis. The peaks represent the periodic crossing of axes. The peak structure is softened as a result of the thermal vibrations. Furthermore, the coherent radiation spectrum is superimposed to an incoherent scattering background contribution, which is all that is left when $\eta \equiv \hbar\omega/E$ (the x axis) approaches 1. For large-angle impinging particles (dotted line), the peak structure disappears. However the enhancement over the Bethe-Heitler equation (1.36) rate (dashed line) is still large. The main source of enhancement is the coherent scattering with atoms belonging to a crystal row (or plane).

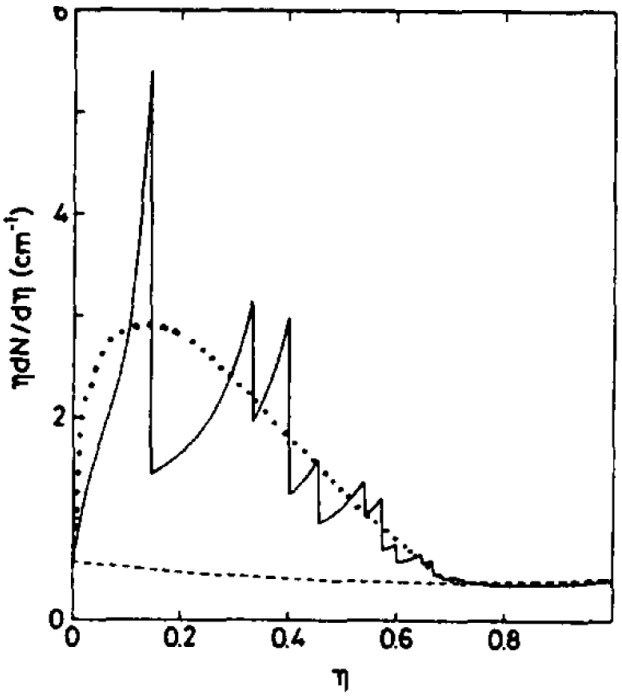

Figure 1.22: Solid line: coherent bremsstrahlung for a 10 GeV/c electron beam incident on a $\langle 110 \rangle$ germanium at 1 mrad with respect to the axis. Dotted line: coherent bremsstrahlung for a large-angle impinging particle; the enhancement is still present, but the peak structure has disappeared. Dashed line: Bethe-Heitler equation (1.36) prediction which represents the incoherent background. Image from [34].

1.4.4 Channelling Radiation

The perturbation approach to describe the particle motion inside the crystal breaks down in the channelling condition: in fact the motion of a

channelled particle cannot be approximated as the one of a free particle, and only the interaction with the radiation field might be treated as a weak perturbation.

As pointed out in the previous section, the channelling radiation for electrons of few MeV requires a quantum mechanical description. Given the fact that the crystal potential defines the possible states for the motion, which are the eigenstates of equation (1.33), the interaction between the impinging particle and the radiation fields allows the transitions between such eigenstates.

The treatment may be simplified in the *longitudinal rest frame* $\mathcal{R}$ moving with respect to the *laboratory frame*, with $v_z \equiv p_z/\gamma m$, that is by taking the viewpoint of an observer moving along the channel with the particle. In $\mathcal{R}$ the particle motion is purely transverse, and the energy spectrum is thus quantized. In this frame, when undergoing a transition from a higher level to a lower level, an electron emits a photon whose energy equals the energy difference between the electron states of transverse motion, having no other possible source to take the energy from.

The rest frame is a useful mean to study the features of the channelling radiation. In $\mathcal{R}$ the crystal appears Lorentz-contracted along the z (channelling) direction: the potential is then magnified by a factor γ with respect to the laboratory frame $U^{\mathcal{R}} = \gamma U$. Also the kinetic energy term in equation (1.33) is magnified by the same factor, since in $\mathcal{R}$ the motion is non-relativistic. These two observations result in a scaling of the transverse energy spectrum by a factor γ, that is, $E_\perp^{\mathcal{R}} = \gamma E_\perp$ while $u(\boldsymbol{r}_\perp)$ remains unchanged. The photon energy measured in $\mathcal{R}$ corresponding to a transition between the transverse energy states $E_{\perp,i}$ and $E_{\perp,f}$ is

$$\hbar\omega^{\mathcal{R}} = -\Delta E_\perp^{\mathcal{R}} = -\left(E_{\perp,f}^{\mathcal{R}} - E_{\perp,i}^{\mathcal{R}}\right) = -\gamma \Delta E_\perp \tag{1.41}$$

A Doppler transformation back to the laboratory frame provides the final result:

$$\hbar\omega = \frac{-\Delta E_\perp}{1 - \beta\cos\theta_\gamma} =\simeq \frac{2\gamma^2\left(-\Delta E_\perp\right)}{1 + \left(\gamma\theta_\gamma\right)^2} \tag{1.42}$$

where the approximation is valid in the limit $\beta \equiv v/c \to 1$, but it is fairly accurate as soon as E is larger than 2 - 3 MeV.

The γ^2 factor in equation (1.42) shifts the energy difference $\Delta E_\perp$, which is typically few tens of eV, in the keV range, although in the laboratory frame most of the energy is related to the motion in the channelling direction.

θ_γ is the emission angle with respect to the z axis: in $\mathcal{R}$ a dipole pattern is obtained. However, since an emission at 90° in $\mathcal{R}$ corresponds to an emission angle of $\sin^{-1}(1/\gamma) \simeq 1/\gamma$ in the laboratory frame, the channelling radiation

is strongly forward peaked in a narrow cone along the channelling direction, exactly as the "normal" bremsstrahlung.

Figure 1.23 presents the intensity of the channelling radiation produced by a $4\,\mathrm{MeV}/c$ electron beam impinging on a $\langle 111 \rangle$ silicon crystal as a function of its energy and the incident angle, where the quantum jumps are clearly visible. The atomic spectroscopy notation ($l = 0, 1, 2, 3 \ldots \quad \mapsto \quad s, p, d, f \ldots$) has been used [42].

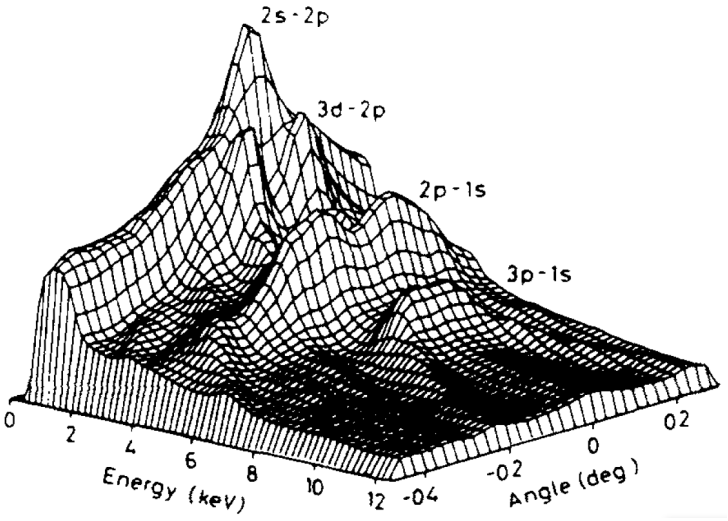

Figure 1.23: Intensity of the channelling radiation produced by a $4\,\mathrm{MeV}/c$ electron beam impinging on a $\langle 111 \rangle$ silicon crystal as a function of its energy and the incident angle. Image from [34]

As the particle energy increases up to a few GeV, the number of available states increases and the level spacing reduces correspondingly. Hence the channelling radiation appears as a classical emission process. In general the classical channelling radiation spectra are just broader and featureless.

However, planar channelling for positrons represents an exception. Since the motion is periodic and the interplanar potential may be approximated as harmonic, the oscillation frequency depends only weakly on $E_\perp$. For a purely harmonic potential in a non relativistic reference frame (such as the rest frame $\mathcal{R}$), the emission is only into the first harmonic. However, anharmonicity in the real interplanar potential results in higher harmonics being populated.

Again, the technical calculation goes beyond the purposes of this section. It is worth to note that such predictions have been verified experimentally [42]. Figure 1.24 presents the spectrum of the channelling radiation emitted by a $6.7\,\mathrm{GeV}/c$ positron beam incident parallel to the $\langle 110 \rangle$ plane of a 0.1 mm thick silicon crystal. Even if the experimental data (circles) exhibit a trend

similar to the one predicted by the theoretical predictions based on standard electrodynamics formulas (solid line), there is a moderate discrepancy between the two.

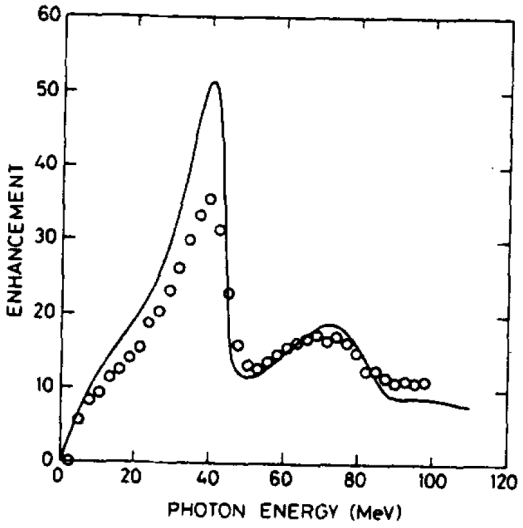

Figure 1.24: Spectrum of the channelling radiation emitted by a 6.7 GeV/c positron beam incident parallel to the $\langle 110 \rangle$ plane of a 0.1 mm thick silicon crystal. Even if the experimental data (circles) exhibit a trend similar to the one predicted by the theoretical predictions based on standard electrodynamics formulas (solid line), there is a moderate discrepancy between the two. Image from [34].

When the energy of the incident electron or positron increases to the several GeV range, the classical description of the radiation emission process is not valid anymore. The problem here is not the quantization of the available states, since the density of states is proportional to γ. The breakdown is associated with the nuclear recoil due to the radiation, which is no more negligible, and a quantum description is again necessary.

In Quantum Field Theory (QFT), *crossing* is the property that allows the scattering amplitudes of processes related by one of the three discrete symmetries (namely Charge inversion, Parity and Time inversion) to be obtained by simply exchanging the relevant variables. Thus, an increase in hard photon emission by incoming electrons should correspond to an amplification of the reverse process of *electron-positron pair production* induced by a photon impact.

1.5 A crystal-based positron source

An intense positron source is a crucial element in the design of future e^+e^- colliders. While electrons can be readily stripped off from atoms, positrons do not exist in nature and must be produced. All present high-energy lepton colliders are based on the so-called *conventional scheme* (figure 1.25a): a high-energy electron beam impinges on a high-density and high-Z target, such as tungsten, which is very thick (several X_0 in length). An electromagnetic shower starts inside the material, and photons are produced primarily via bremsstrahlung, and, in turn, convert into electron-positron pairs [51].

While the conventional design for positron sources is well-known and simple, it may not be suitable for the next generation of high-energy lepton colliders, such as the Future Circular Collider (FCC), since it is not possible to reach the required intensity [52].

In fact the main problem of a conventional positron source is the unprecedented intensity required by next generation colliders (FCC requires a positron bunch of 2.1×10^{10} particles), which would result in serious target heating and radiation issues, especially if the target is optimized for the generation of as many positrons as possible, that is 3.6 X_0 [52] [53].

Moreover, the beams obtained with the conventional scheme feature an output emittance[3] which is orders of magnitude worse than the ones from high-brilliance electron sources due to the large divergence and momentum spread resulting from the shower development and the multiple scattering in the target [51].

A potential alternative for designing a new generation of positron sources is a crystal-based hybrid positron source. The key concept involves two separate components: a photon radiator and a converter, where positrons can be produced (figure 1.25b). Additionally, collimators (figure 1.25c) and magnets (figure 1.25d) can be integrated into the layout. The former contribute to cutting off the tails of the beam, while the latter help sweeping away all charged particles from the acceptance of the converter [55].

As previously described in section 1.4, within an oriented crystal, the radiation produced by an impinging electron experiences an increase due to the coherent bremsstrahlung and channelling radiation. This increase has been experimentally measured at CERN [56].

e+BOOST (intense positron source Based On Oriented crySTals) is a two-year Italian project funded by MUR (Ministero dell'Università e della Ricerca), whose goal is to demonstrate the feasibility of a crystal-based scheme

[3] In accelerator Physics, the emittance is a property of a charged particle beam. It refers to the area occupied by the beam in a position-and-momentum phase space [54].

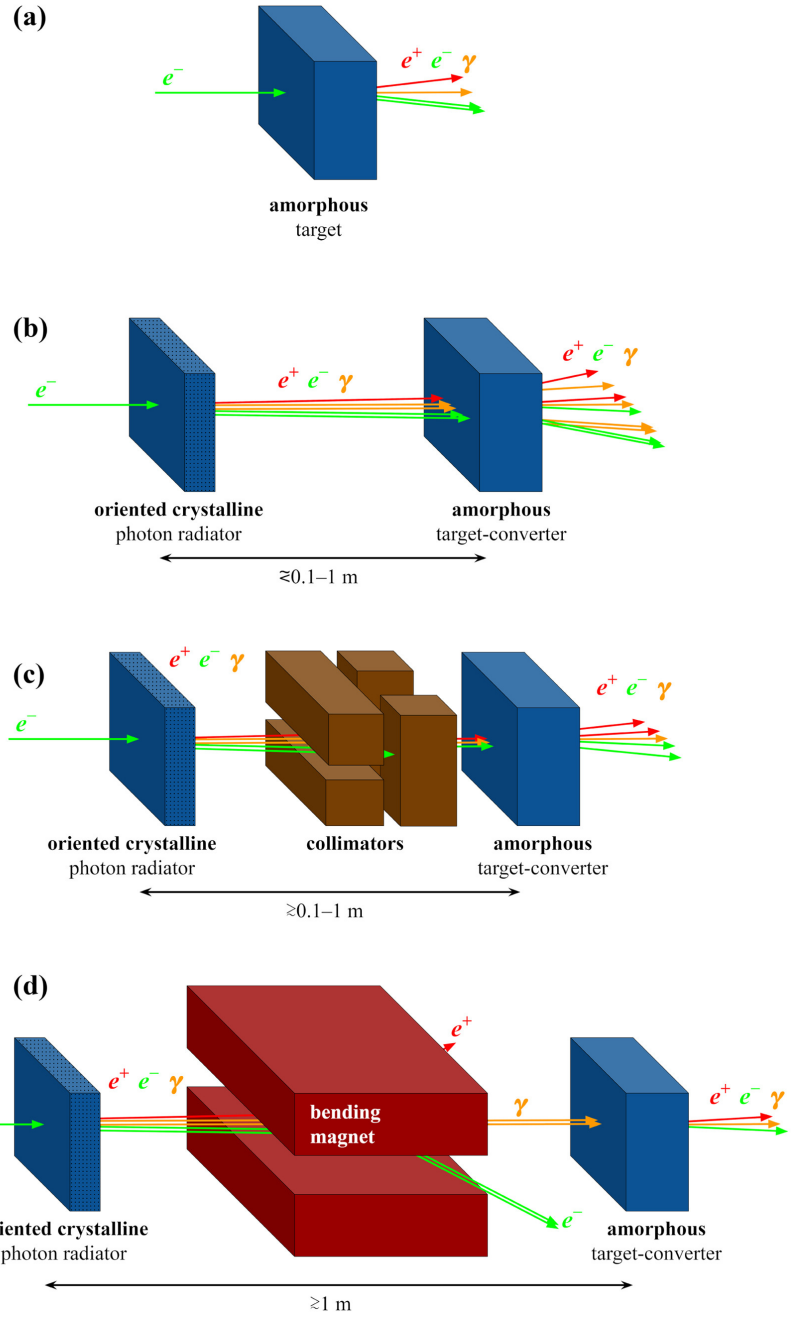

Figure 1.25: Comparison between different positron source layouts: (a) conventional; (b) hybrid simple; (c) hybrid optimized with collimators; (d) hybrid optimized with a bending magnet. Image from [55].

as an alternative to conventional methods for generating intense unpolarized e^+ beams. This technology could potentially be incorporated into the Future Circular Collider project.

A total of three crystals were tested on the T9 extracted beamline in the CERN East Area during August 2023:

- a 2.5 mm thick $\langle 111 \rangle$ tungsten crystal
- a 1.5 mm thick $\langle 111 \rangle$ tungsten crystal
- a 1 mm thick $\langle 110 \rangle$ iridium crystal

e+BOOST plans to experimentally test the photon enhancement in the crystal radiator and the positron yield of the hybrid scheme at the energies of interest for the FCC, which are 6 and 20 GeV/c.

The experimental evaluation of the performance of tungsten and diamond crystal prototypes requires a beam with an angular divergence as small as possible, of the order of the critical angle, which is $\sim 450\,\mu$rad for tungsten and $\sim 100\,\mu$rad for carbon (diamond) at 20 GeV/c. As explained in the following chapter, reducing the divergence leads to an enlargement of the beam spot and thus to particles not crossing the crystal. This problem can be addressed by selecting a small portion of the beam, triggering the acquisition system exclusively with particles crossing the crystal under test.

This thesis describes the development of a test system capable of reconstructing the tracks of the incoming particles with high resolution as well as selecting a portion of the incoming beam. The system is designed to provide also a measurement of the increase in the radiation intensity produced by an oriented crystal radiator.

1.6 GALORE

GALORE (hiGh-efficient beAm defLector fOR accElerators) is a two-year (2022-2023) INFN project which aims at enhancing the crystal channelling performance by suppressing the dechannelling phenomenon in the planar channelling scenario. The key idea, initially proposed by Professor Tikhomirov [57], is to modify the particle dynamics within the crystal by introducing a *lattice interruption* at the very beginning of the crystal itself. This can be done either by etching a trench or by burying an amorphous layer [57]. The amorphous layer acts as a lens, focussing the positive-charged particles away from the crystal nuclei before the dechannelling process can take place. Figure 1.26 shows a Monte Carlo simulation for a 180 GeV/c proton in planar channelling:

the particle motion is characterized by periodic oscillations between the crystal planes, but particles with an initial too low impact parameter are rapidly dechannelled [58].

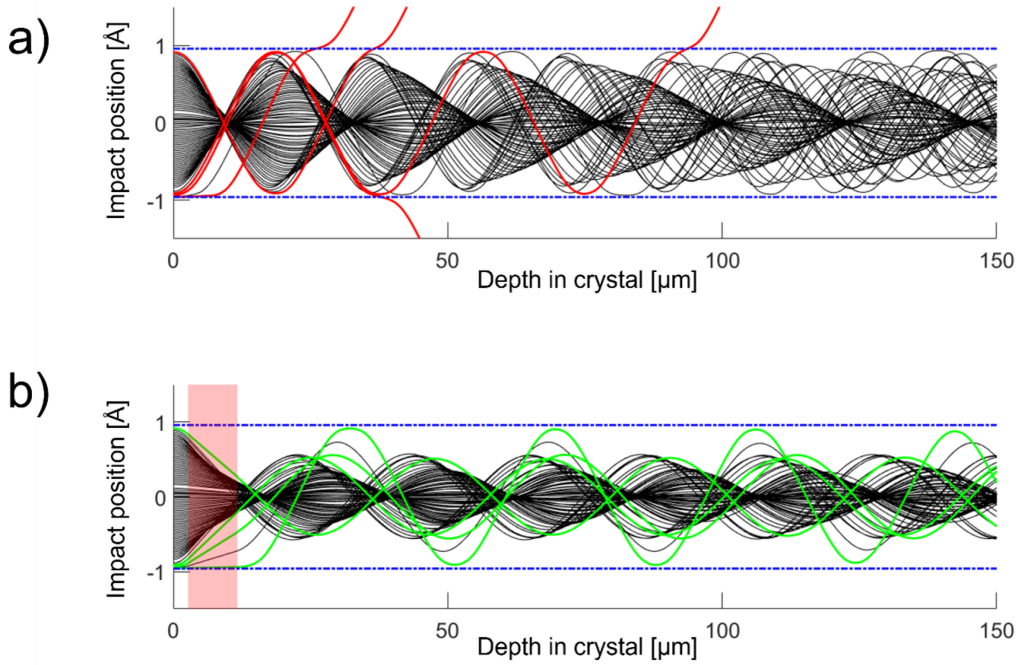

Figure 1.26: Monte Carlo simulation of a 180 GeV/c proton in planar channelling. The blue lines indicate the atomic plane position. (a) Simulated trajectories for a normal crystal; the red lines are the dechannelled particles. (b) The pink region indicates the interruption of the lattice; the green lines are the dechannelled particles of figure (a), which now are channelled. Image from [3].

Since the first experiments in the 1980s, thanks to an extensive R&D, the steering efficiency has been increased from few % up to $\sim 80\,\%$, limited only by the scattering of the particles with nuclei inside the crystal. GALORE aims at going beyond this limit by developing a new generation of bent crystals to boost the efficiency near to 100 %.

Such crystals might be applied to *extract the halo* at high-energy accelerators such as LHC, acting as a bending magnet of hundreds of Tesla, but without the need of either power consumption or a cryogenic environment. Furthermore they are lightweight and compact, thus suitable for being integrated in particle accelerators. The halo can be directed toward fixed-target experiments using existing detectors [59] [5] or even toward a new extracted

beamline allowing an innovative Physics program exploiting the multi-TeV proton and ion beams [60] [61]. A possible integration in the LHC ring has been discussed in detail in section 1.1.1.

The crystal designed for the GALORE experiment is a 4.1 mm long in the beam direction silicon crystal. The face perpendicular to the beam is $0.5\,\mathrm{x}\,55\,\mathrm{mm}^2$. The micro structure is $0.15\mathrm{x}10\,\mathrm{mm}^2$ measured in the middle of the crystal sample. The crystal is flat for the first 0.1 mm and then curved for the remaining 4 mm with a curvature radius of about 130 m, inferred since a deflection of 30 µrad has been measured during the GALORE beamtest on the H8 CERN beamline in June 2023 and later confirmed with a diffractometer.

The GALORE crystal (figure 1.27) represents a technological challenge both for the design and for the production. However, the purpose of this thesis work is not to describe these aspects, which are extensively detailed in [58] and [3].

The H8 beamline at CERN offers a variable-intensity positive pion beam of 180 GeV/c with a maximum $\Delta p/p$ acceptance $\sim 1.5\,\%$ and with a beam spot of the order of 1 cm [62]. Considering the small section of the crystal perpendicular to the beam and that the trench is present only in a small subsection, a very high intensity is needed to acquire enough statistics in a reasonable time. By design, this beamline is capable of delivering the primary proton beam up to 400 GeV/c; such a beam could be an advantage, considering that the angular divergence and the beam spot are inversely proportional to the momentum. Furthermore, the dimension of the microstructure scales with the square root of the momentum, making it easier to manufacture a crystal with the required features. However, due to technical reasons, some of which will be presented in section 2.2.2, this option was not available. Instead, a mixed hadron tertiary positive beam, mainly composed of 180 GeV/c pions, is still acceptable and has allowed the collection of high-quality data.

A high-resolution single-particle tracking system is required for a reliable channelling efficiency measurement. The University of Insubria INSULAB research group, responsible of the tracking system, has developed a silicon microstrip system, which will be described in detail in chapter 3.

The critical angle may be estimated using equation (1.21), knowing that the potential well U for the (110) channelling plane is 22 eV: θ_c results to be ≈ 15 µrad. Considering equation (1.25), one can observe that the curvature of the crystal may contribute to a reduction of the critical angle. However, for $pv = 180$ GeV, using a maximum electric field in the potential well of 5.7 GeV/cm, a critical curvature radius of about 30 cm is obtained, which can be neglected for a crystal bent with a radius of 130 m. The critical angle for

Figure 1.27: Photo of the GALORE silicon crystal installed on the goniometer for the alignment to the particle beam in the PPE128 experimental area of the H8 SPS extracted beamline at CERN.

a bent crystal in fact is given by

$$\theta_c^{\text{curved}} = \theta_c^{\text{plane}} \left(1 - \frac{R_c}{R}\right) \tag{1.43}$$

being R_c and R the critical and the bending radii [3].

As in the case of the feasibility tests of the positron source, the value of the angular divergence is crucial, to have the incoming particles within the channelling angular acceptance. However, for this crystal, the region of interest perpendicular to the beam is only 0.15x10 mm^2. Without the possibility to select only the particles impinging onto this area, acquiring a statistics large enough in a reasonable time frame would be impossible. The experimental measurement of the channelling efficiency of the GALORE crystal required a test system capable of selecting a small portion of the beam and tracking both the incoming and deflected particles with high spatial resolution. As for the crystal-based positron source, the readout electronics of the silicon trackers had to be upgraded.

In this chapter, several applications of crystals in particle Physics have been discussed, with a particular emphasis on the crystal-based positron source and the GALORE project. The following chapters will define the key elements to understand how these crystals behave: the test layout and the test facilities (chapter 2), and the testing system (chapter 3), which has been upgraded to meet the test requirements of the GALORE project and which is the major topic of this thesis.

Chapter 2

The Test Facilities

The experimental measurement of the phenomena described in the previous chapter requires an intense beam of charged particles and tracking detectors with high spatial resolution capabilities (1 - 10 µm).

The key factors to consider for testing a crystal on a beamline are the *beam intensity* and the *angular divergence*. A high intensity, namely a large amount of particles, is required in order to gather a statistics large enough in a limited amount of time. However, as intensity increases, the occurrence of *single cluster events*, that is, events characterized by one single particle, decreases with respect to those involving more than one particle, that make the identification of the effect of the crystal impossible.

Moreover, given that the angular acceptance for channelling is of the order of the critical angle, the *angular divergence*, which is defined as the angle of the particle with respect to the beam direction z in the xz and yz planes, has to be as small as possible. Events with a divergence greater than the critical angle in fact will not undergo the phenomenon of interest, that is channelling in the case of the GALORE experiment. Considering that the process occurs with an efficiency smaller than 1, reducing the beam divergence allows an increase in the number of events with a reasonable chance of channelling inside the crystal. Nevertheless, reducing the beam divergence leads to an enlargement of the *beam profile*, which is undesirable as the crystals used in channelling experiments are small in the plane orthogonal to the beam. In this scenario, a trade-off between divergence and beam size, or intensity over a fixed area, must be found.

This chapter opens with an overview of the different layouts and systems designed for testing a crystal on a beamline. Then, three beamtest facilities will be introduced, describing their key features that have influenced the design of the test system.

2.1 Crystal Test Setups

In the previous chapter, two potential applications of the channelling effect were explored. Despite the common underlying physical phenomenon, that is channelling, the test setup required to perform on-beam measurements is quite different in the two cases. For the crystal-based positron source (section 1.5), the main goal is to measure the produced radiation as a function of the crystal orientation. On the other hand, GALORE (section 1.6) aims at characterizing a new crystal design by measuring the channelling efficiency. This efficiency represents the probability that a particle impinging within the channelling acceptance achieves and maintains the channelling condition throughout the crystal length.

2.1.1 Experimental Layouts

The experimental layout, presented in figure 2.1, to test the performance of a crystal as a photon radiator, features the following key elements:

- A pair of high-resolution tracking detectors, such as silicon microstrip ones, to track the incoming particle.

- The crystal under test, mounted on a high-precision multi-stage goniometer to accurately choose the angle between the beam incidence direction and the crystal axes/planes.

- A bending magnet may be added, though not fundamental, to swipe all the charged particles allowing only photons to travel along the beam direction.

- An active Photon Converter (APC), composed of a thin copper layer ($0.1 - 0.4\,X_0$) sandwiched between a couple of 1 cm thick plastic scintillators. The first scintillator acts as a *veto* allowing the APC to discard the events in which not only photons are present. Within the copper layer, a small fraction of the photons may convert in an electron-positron pair which can be detected by the second plastic scintillator. This system, combined with simulation, provides an average information about the photon multiplicity, useful both to find the correct axial orientation and to measure the produced radiation.

- At the end of the line, an electromagnetic calorimeter measures the deposited energy by fully absorbing the radiation.

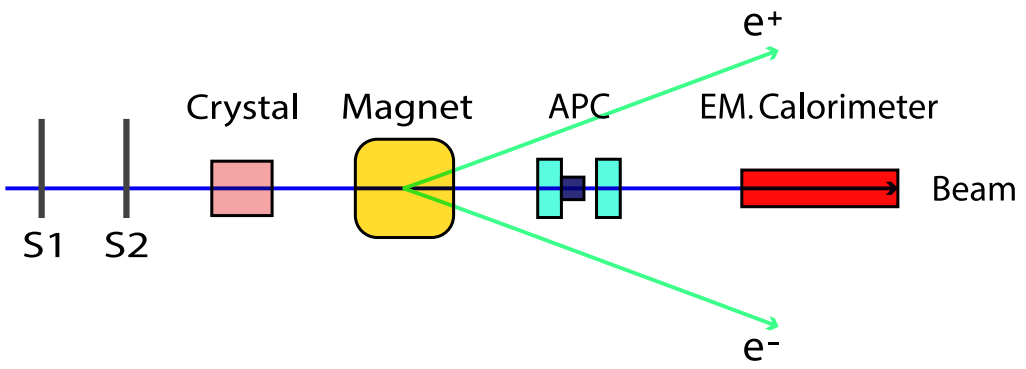

Figure 2.1: Sketch of the beamtest layout for the measurement of the enhancement of the radiation production for a crystal-based positron source. A couple of silicon detectors reconstructs the track of the particle impinging onto the crystal. A magnet swipes away all the charged particles. The Active Photon Converter (APC), composed of a thin copper layer sandwiched between a couple of plastic scintillators, provides an average information about the photon multiplicity, useful both to find the correct axial orientation and to measure the produced radiation. At the end of the line, an electromagnetic calorimeter measures the deposited energy by fully absorbing the beam.

The study of channelling in a bent crystal, as for the GALORE experiment, requires a high spatial resolution track reconstruction for both the incoming and outgoing particle. The main elements for such an experimental setup, presented in figure 2.2, are the following:

- A pair of high-resolution tracking detectors, such as silicon microstrip ones, to track the incoming particle.
- The crystal under test, mounted on a high-precision multi-stage goniometer.
- Another pair of tracking detectors to reconstruct the outgoing track. If the crystal is short along the beam direction, as the GALORE one, a single downstream detector may be enough, with the second point of the outgoing track provided by the particle position on the crystal itself.

The fourth detector should have a dimension of at least $\ell = d \tan\theta$, being θ the deflection angle and d the distance between the crystal and the farthest silicon module. This requirement fixes the maximum distance at which it can be installed. Each pair of tracking detectors should be placed at the

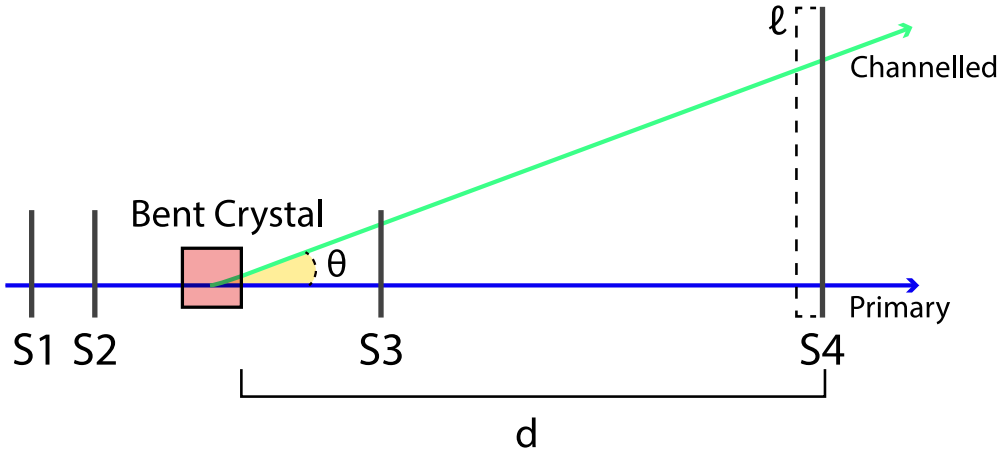

Figure 2.2: Sketch of the beamtest layout for the measurement of the channelling performance of a bent crystal: S1 and S2 track the incoming particle while S3 and S4 reconstruct the channelled particle. The fourth detector should have a dimension of at least $\ell = d \tan\theta$, being θ the deflection angle.

largest possible distance, as the angular resolution is a function of the distance between the detectors themselves.

Once again, a trade-off must be reached, primarily based on the deflection angle of the crystal under test and the length of the beamline. Given a fixed spatial resolution of the detectors, increasing the distance between the two detectors enhances the angular resolution. However, if there is not a vacuum tube between the detectors, the multiple scattering with the air degrades the resolution. Moreover, as far as the downstream pair of detectors is concerned, if the crystal has a large deflection angle, they should have a large dimension and should be located near enough to intersect the bent beam. On the other hand, if the deflection angle is small, a good spatial resolution is essential, while a large area is not necessary.

The data acquisition system needs a *trigger* signal when a particle crosses the detectors such that the detectors themselves sample and store the information. A possible way to generate this signal is to use the discriminated signal of a plastic scintillator or of a pair of scintillators working *in coincidence* configuration, that is the logical AND of the two discriminated signals. This approach is very common since plastic scintillators can detect charged particles without degrading the beam. Moreover, they can be crafted in different dimensions and shapes allowing them to detect only a portion of the beam.

When testing small dimension crystals or crystals with particular features

such as the GALORE one, it is fundamental to have a low divergence and small dimension beam. The angular divergence may be reduced through a suitable configuration of the magnets of the beamline; however, this leads to a larger beam size and thus to the acquisition of a considerable percentage of useless events, which saturate the DAQ (Data AcQuisition) capability and have to be discarded offline.

Plastic scintillators can be designed to be small enough (for instance using fibers), but the mechanical assembly and the alignment with the crystal may become difficult tasks.

For these reasons, it was decided to upgrade the readout electronics of the tracking detectors allowing the system to trigger on specific strips of the tracking detectors themselves. In this way, it is possible to start looking at the whole beam and then select only the region of the beam itself that crosses the crystal face.

It is important to note that there is no universally defined *best module*. Depending on the specific beamline and the characteristics of the crystal under test, different detectors may be more appropriate. As discussed earlier, in a typical experimental setup, different modules are employed for different purposes; for instance, self triggering capability is required only for the upstream pair, while the downstream module typically needs to have a wider active area. In chapter 3 several microstrip detectors of the INSULAB research group will be described.

2.1.2 The goniometer

To ensure that a particle beam impinges within the channelling angular acceptance, the crystal under test must be aligned very precisely to the beam itself. The system used for this goal was based on a multi stage high precision goniometer, hosting the crystal sample. The goniometer consists of several stages, manufactured by PI[1], that can be combined in several ways:

- WT-100 cradle stage, with a rotational range of 10°, 2 kg of maximum load and a repeatability of 8.7 µrad. By employing an encoder and an active feedback system, a resolution of 1.57 µrad may be achieved. This stage allows the orientation of the crystal with respect to the beam in the $y - z$ plane.

- Similar to the previous one, the WT-90 is another cradle stage, where the rotational range is 90° with 2.7 µrad of repeatability and a maximum

[1]Physik Instrumente, `https://www.pionline.it/it/`

load capacity of 8 kg. With an active feedback system, the achievable resolution is 2.69 µrad.

- PRS-110 is a rotational stage which can perform a full 360° rotation in the $x - z$ plane, that is, around the y direction.

- Two linear stages (VT-80 and L-511) allow to control the position of the samples along the x axis, with a 1.5 µm accuracy, a 2 µm bidirectional repeatability and a 5 µm resolution. The range is 102 mm for the former and 52 mm for the latter.

- L-310 is a vertical stage with a full range of 26 mm and a 10 kg maximum load capacity. This stage may be used for moving the crystal along the vertical y direction. A maximum resolution of 0.2 µm can be achieved thanks to the encoder.

The stages are connected through dedicated cables to different controllers, such as the Corvus, the Pollux and the Mercury, all manufactured by PI. The controllers are directly connected to the DAQ computer and communicate through a RS-232 serial port.

Depending on the experimental requirements, a different combination of the listed stages is employed. Furthermore, the goniometer may be installed on remotely controlled platforms, such as the Desy table or the XSCA table, which offer two additional translational degrees of freedom along the x and y directions, that is, perpendicularly to the beam. A comprehensive description of the features of the goniometer may be found in [63]. Figure 2.3 presents the goniometer configuration used for the beamtest of a crystal-based positron source, installed on a XSCA table; for the GALORE experiment a linear stage was mounted to align the crystal also in the vertical direction, as in the PPE128 experimental area no moving platforms were available.

2.2 CERN Beamtest Facilities

The accelerator complex at CERN is a succession of machines that accelerate particles to increasingly higher energies. Each machine boosts the energy of a beam of particles before injecting it into the next machine in the sequence. Linac 4, a linear accelerator, speeds up negative hydrogen ions (H^-, hydrogen atoms with an extra electron) up to 160 MeV/c. The ions are stripped of their two electrons and the resulting proton is fed into the Proton Synchrotron Booster (PSB), an accelerator with four superimposed synchrotron rings, and is accelerated up to 2 GeV/c. The next machine is the

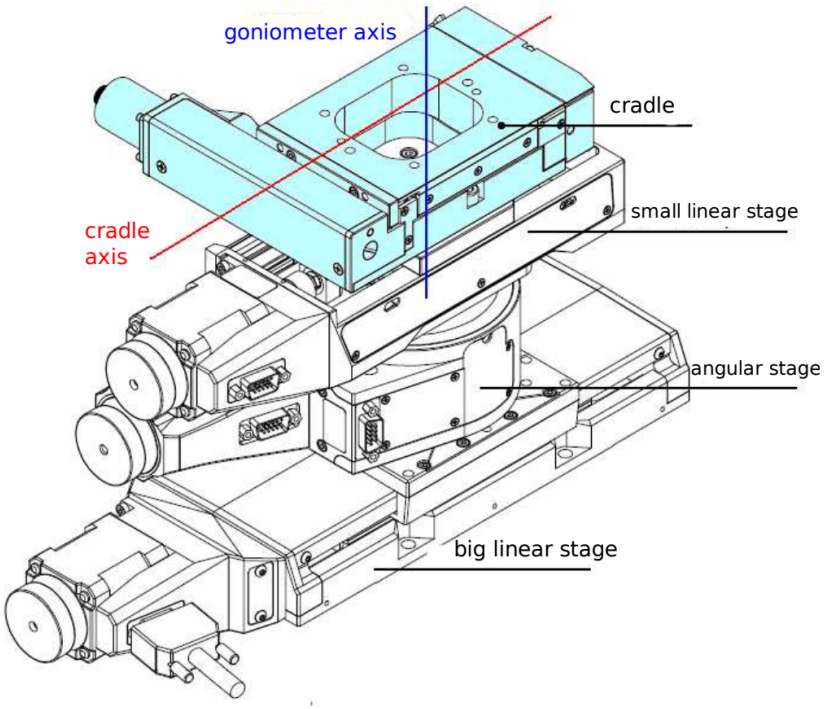

Figure 2.3: Sketch of the goniometer configuration used for the beamtest of a crystal-based positron source in the T9 beamline. The goniometer was installed on a remotely controlled moving platform (XSCA table). Image from [64].

Proton Synchrotron (PS), the CERN first synchrotron, which can increase the proton momentum up to 24 GeV/c. These protons can be either extracted to the *East Area Beamlines* or sent to the Super Proton Synchrotron (SPS) which can push the beam up to 450 GeV/c. The accelerated proton beam can be either delivered to the *North Area* beamlines or sent to the largest and most powerful particle accelerator in the world, namely LHC (Large Hadron Collider) [65].

The CERN accelerator complex features other accelerators and facilities that will not be described since they are of no interest for crystal Physics. Figure 2.4 presents the whole CERN accelerator complex.

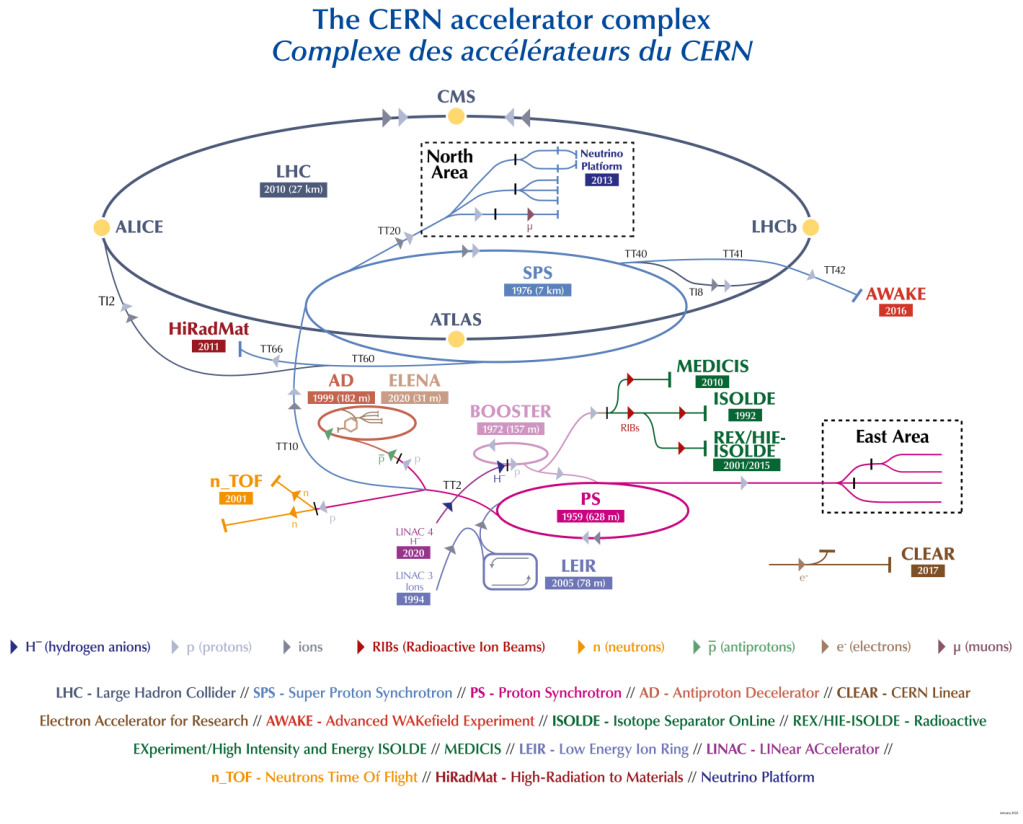

Figure 2.4: CERN accelerator complex. Image from [65].

2.2.1 T9 PS extracted beamline

The CERN *East Area* hosts the Proton Synchrotron extracted beamlines. Among them, there is the *T9* one capable of delivering an intense (up to 10^4

electrons per spill [66]) and a high-purity tertiary beam of electrons/positrons up to 6 GeV/c. Figure 2.5 presents the East Area beamlines, where T9 is in yellow; figure 2.6 presents a photo of the experimental areas.

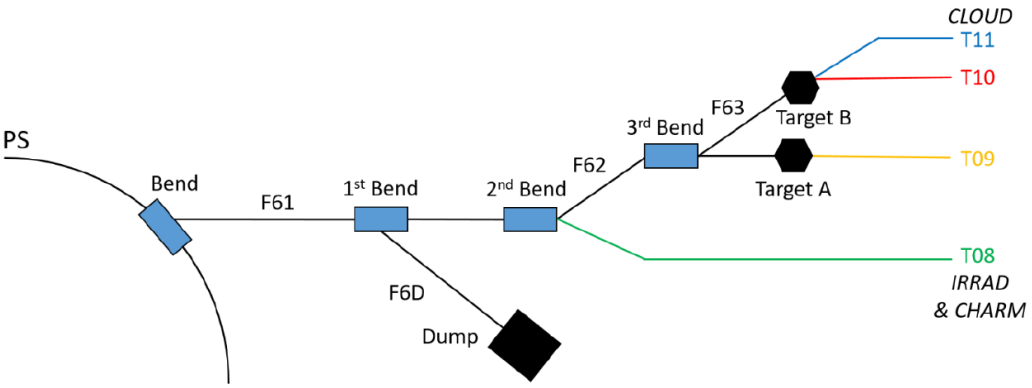

Figure 2.5: Sketch of the CERN East Area beamlines. The T09 beamline is in yellow. Image from [67].

The experimental area ($\sim 90\,\mathrm{m}^2$) can be equipped with a bending dipole magnet with a field up to 0.6 T m, and remotely controlled moving platforms, such as XSCA and Desy tables.

The East Hall experimental area underwent renovation in 2019 during the Long Shutdown 2 period; for a detailed description of the whole experimental hall and the renovation project, the reader is referred to [67].

2.2.1.1 The beamline

One of the main features of the T9 beamline is the possibility to have a pure beam of electrons/positrons, a fundamental element for the feasibility test of a positron source.

When the primary 24 GeV/c protons interact with the primary target, many neutral pions are generated which almost exclusively decay in flight in two high energy photons. After the target, two magnets with a maximum field of 0.3 T m are employed to sweep the charged particles towards a beam dump. A 2 - 8 mm lead conversion layer is placed 8 m after, to convert the photons into electron-positron pairs. Since the generated electrons typically carry about half the energy of the gamma rays, which in turn have roughly half the energy of the neutral pions responsible for their production, it becomes evident why the electron beam intensity decreases as the beam momentum increases. For instance, to be produced, a 5 GeV/c electron requires a 20 GeV/c neutral pion from a 24 GeV/c proton, an occurrence that, while possible, is not very

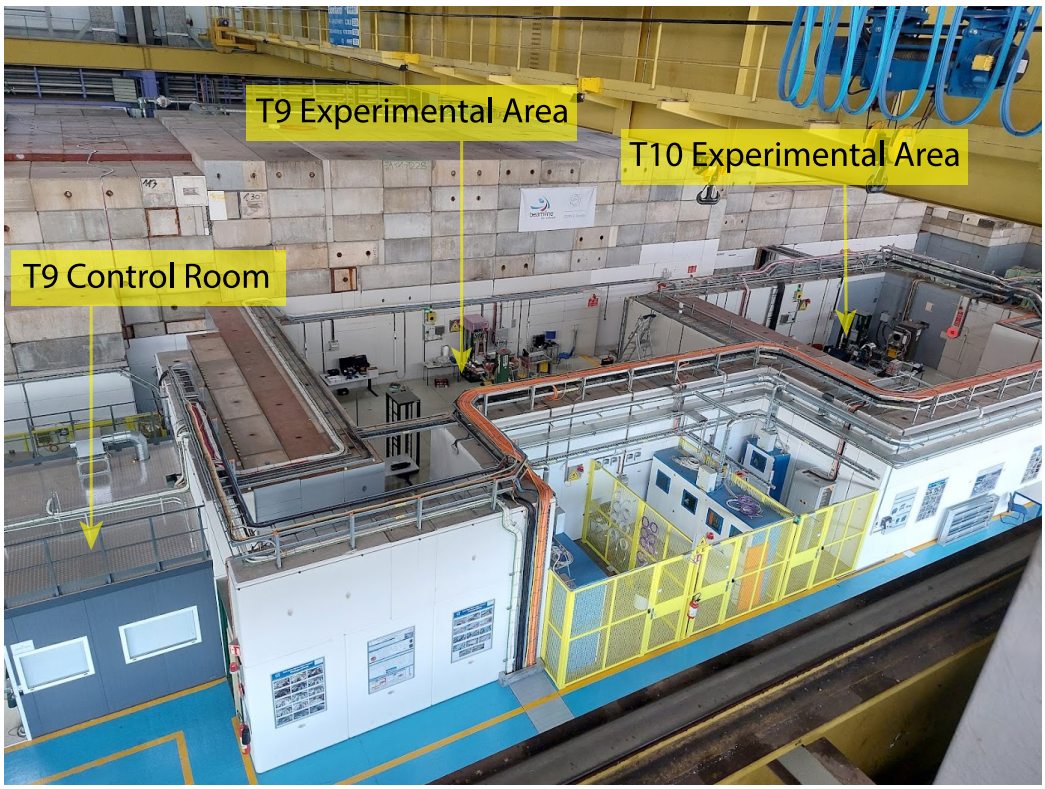

Figure 2.6: Photo of the East Area experimental areas.

frequent. Beyond 6 GeV/c, only a small fraction of secondary electrons is present in the beam. Downstream of the lead converter, a combination of magnets and slits is employed to select the charge and momentum range of the beam. A common choice is to set the slits at ± 3 mm, resulting in a beam momentum spread $\Delta p/p \sim 1\,\%$.

The beam inevitably contains some muons, which come mainly from the decay of charged pions and kaons generated in the target. Muons, as well as hadrons, do not suffer too much from the thin lead absorber. Therefore a small fraction of muons is present in the tertiary beam.

The T9 beamline is also capable of delivering a *secondary beam* of mixed hadrons up to 15 GeV/c, generated after the collision of a primary proton. A small fraction of electrons is present in this beam configuration, and their presence decreases as the momentum increases.

The T9 beamline is equipped with two threshold Čerenkov detectors to discriminate electrons, muons and pions. Particles crossing these gas detectors emit Čerenkov light if they travel faster than the light speed in the gas itself. Given the particle momentum and the particle type, the Čerenkov light emission depends on the gas type and pressure (threshold). Figure 2.7 presents the thresholds for electrons and muons in a tertiary beam (in the 1 - 6 GeV/c range) to generate a signal in a 2.5 m long detector filled with CO_2, computed using the empirical formula:

$$\text{threshold [bar]} = \frac{m^2}{1.01325 \cdot 2np^2} \tag{2.1}$$

where 1/1.01325 is a conversion factor to transform atm in bar, n is the refractive index of the gas (4.18×10^{-4} for CO_2), m is the mass of the particle and p its momentum in MeV/c. Figure 2.8 presents the computed tagging efficiency for electrons and muons of different momenta as a function of the detector pressure. For the electrons in the GeV/c range the curve looks always the same; thus only the 1 GeV/c one has been plotted. The efficiency may be computed according to the formula

$$\text{efficiency} = 1 - e^{2ALn\,(p-p_0)} \tag{2.2}$$

where $L = 2.50$ m is the length of the Čerenkov detectors, p the pressure and p_0 the threshold given by equation (2.1). $A \lesssim 100$ is an empirical constant, depending on the wavelength of the Čerenkov light, the inefficiency of the optical system, the photon collection efficiency, the quantum efficiency of the photocathode and the discrimination threshold. It should be estimated with a fit for each detector, however it is usually set to 50 to provide a (theoretical) estimation of the tagging efficiency within few %. More details

about these detectors and formulas may be found in [68] and [69]. For a more comprehensive characterization of the tagging system, the efficiency, which depends on several other factors, should be experimentally measured using, for instance, electromagnetic calorimeters, where the electron and muon peaks can be clearly identified.

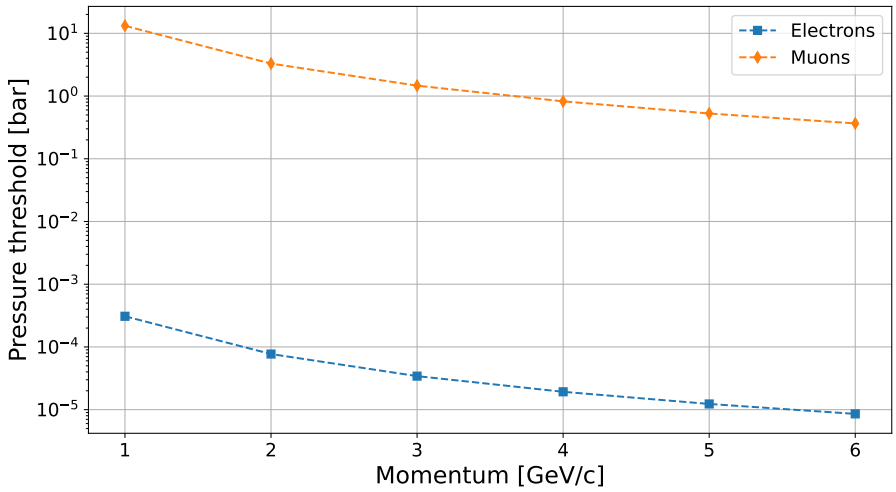

Figure 2.7: Pressure threshold as a function of momentum for electrons and muons to produce Čerenkov light.

At GeV/c momenta, muons behave as MIPs[2] and can provide useful information to calibrate detectors or compensate temperature-dependent gain variations.

2.2.1.2 Parallel and Focussing Optics

As mentioned at the beginning of the chapter, a trade off between angular divergence and beam size has to be chosen. The beamline allows to select between two main beam configurations, called *parallel optics* and *focussing optics*: the former aims at minimizing the divergence (making all the particles to travel *parallel*), while the latter at reducing the beam spot size (by *focussing* at a given point), which results in the divergence increase.

Figure 2.9 presents the x and y angular divergence measured with a couple of silicon beam chambers[3] for focussed and parallel beams as a function of

[2]Minimum Ionizing Particle, a particle which is at the minimum of the Bethe-Bloch energy loss curve.

[3]For a detailed description of the detectors, see section 3.1.1.

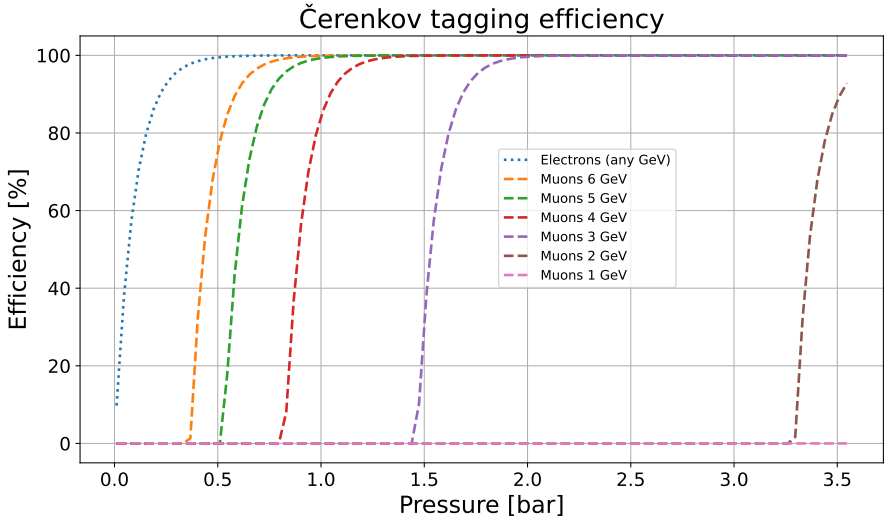

Figure 2.8: Tagging efficiency of a Čerenkov threshold detector as a function of the pressure for electrons and muons of different momenta. For the electrons all the curves in the 1 - 6 GeV/c look the same, and therefore only the 1 GeV/c one has been plotted.

the energy (August 2022 beamtest).

Figure 2.10 presents the beam profiles measured during the same beamtests for 6 GeV/c electrons. It is clear that the price to pay for reducing the divergence is the flattening of the beam profile. In particular, when employing parallel optics, the beam was selected in the y direction by triggering on a suitable group of strips. This approach was adopted because the crystals under test had a small section (approximately $\sim$ cm) and using the wide beam would have resulted in collecting useless data.

2.2.2 H8 SPS extracted beamline

The CERN building 887, also known as *North Area* or *Experimental Hall North 1* (EHN1), accommodates several of the Super Proton Synchrotron (SPS) extracted beamlines. Spanning a length of 330 m and a width of 55 m, the North Area (figure 2.11) stands as the largest experimental area at CERN. Built in 1976, the same year the SPS was switched on, it is located in the French site in Prévessin.

The SPS has six extracted lines, two of which are directed towards dedicated buildings hosting fixed experiments, namely NA62 and COMPASS/AMBER. The remaining four, called H2, H4, H6 and H8, are directed to the

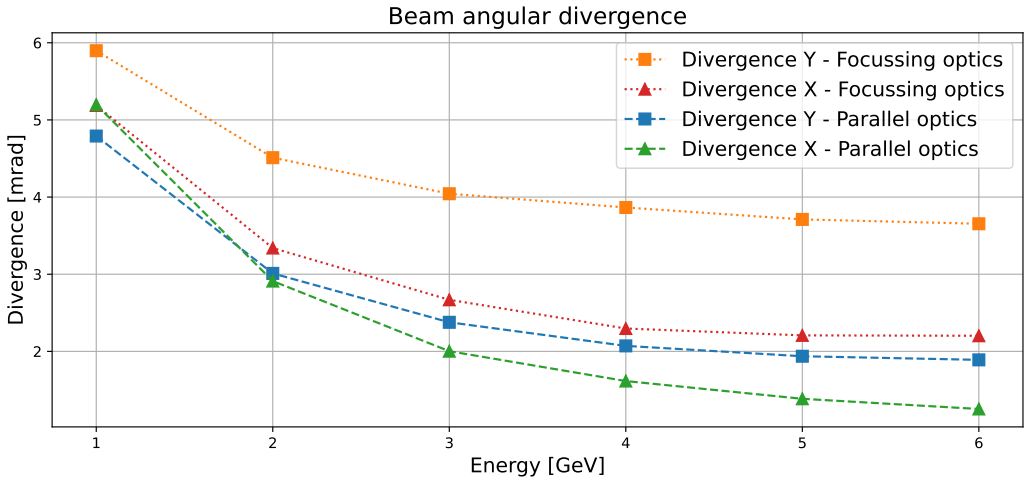

Figure 2.9: Plot of the beam x (squares) and y (triangles) angular divergence for different T9 beam configurations, with parallel optics (dashed lines) and focussing optics (dotted lines) as a function of the energy. Using the parallel optics configuration, a smaller divergence can be achieved.

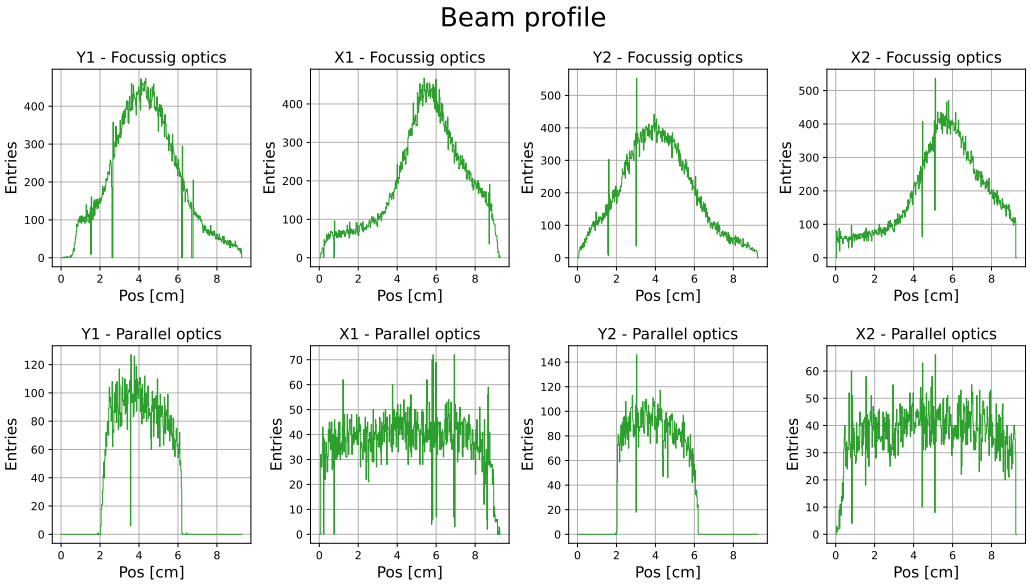

Figure 2.10: Beam profile for 6 GeV/c electrons with focussing optics (first row) and parallel optics (second row). In the latter case the beam profile is flattened; along the y direction it goes to zero at the edges because of the trigger logic.

Figure 2.11: Photo of the CERN North Area.

North Area. Although the term "North Area" typically refers to the extracted beamline areas, it also encompasses other fixed experiments like NA61 (SHINE), situated on the H2 beamline, and various testing areas crucial for the development of future accelerators and detectors. An extension of the building houses the *Neutrino Platform*, accommodating the Proto-DUNE experiment [70]. Figure 2.12 presents a schematic of the SPS extracted beamlines.

The primary beam accelerated by the SPS impinges on dedicated targets, producing secondary particles. Each target is shared between a pair of beamlines.

The H8 beamline is a high energy and high resolution extracted beamline, capable of providing a secondary mixed hadron beam within the 10 - 360 GeV/c range up to few 10^6 particles per spill. Furthermore, this beamline offers an electron beam with a variable purity ranging from 10 % to 99 %, with a maximum $\Delta p/p$ acceptance of 1.5 %.

Along the H8 beamline, several experimental areas are located; PPE128 is the area used for the GALORE beamtest. Figure 2.13 presents the beam profile and the angular divergence during the GALORE beamtest in June 2022, while figure 2.14 shows the same beam selected with the self triggering system. In particular, a slice approximately 1 mm wide along the x direction was chosen and, as a consequence, the divergence in that direction decreased from 40 µrad to about 30 µrad.

By design, the H8 beamline is capable of delivering the 400 GeV/c primary proton beam [62]. However, this capability is rarely exploited. In fact, the SPS provides around $10^{12} - 10^{13}$ particles, which is a huge amount of power to put in an extracted beamline such as H8, considering that at 180 GeV/c the safety radioprotection limit is around 5×10^6 particles if the beam is

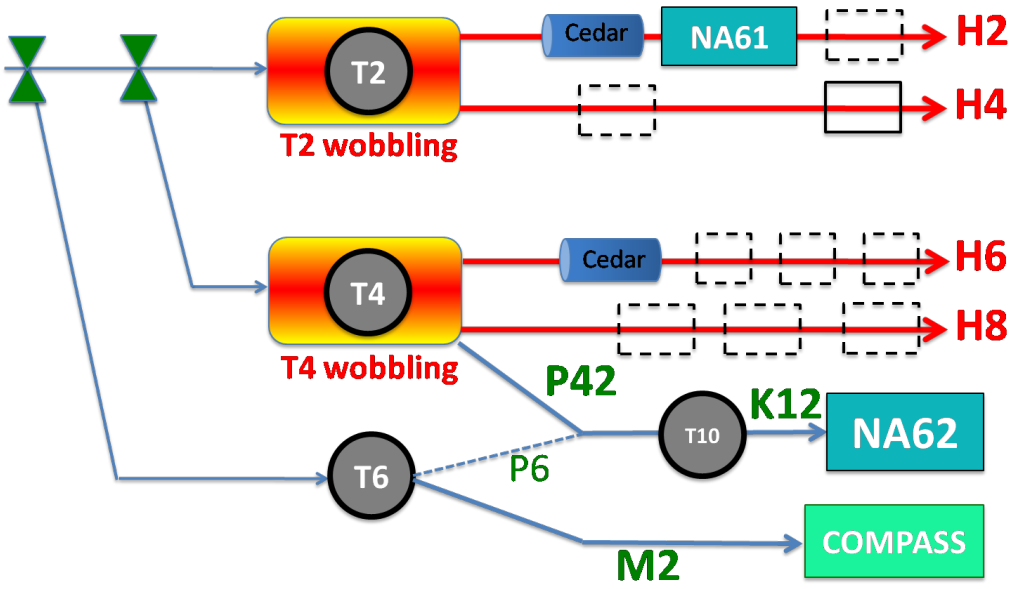

Figure 2.12: Sketch of the SPS extracted beamlines. The H2, H4, H6 and H8 lines are delivered to the North Area. Image from [71].

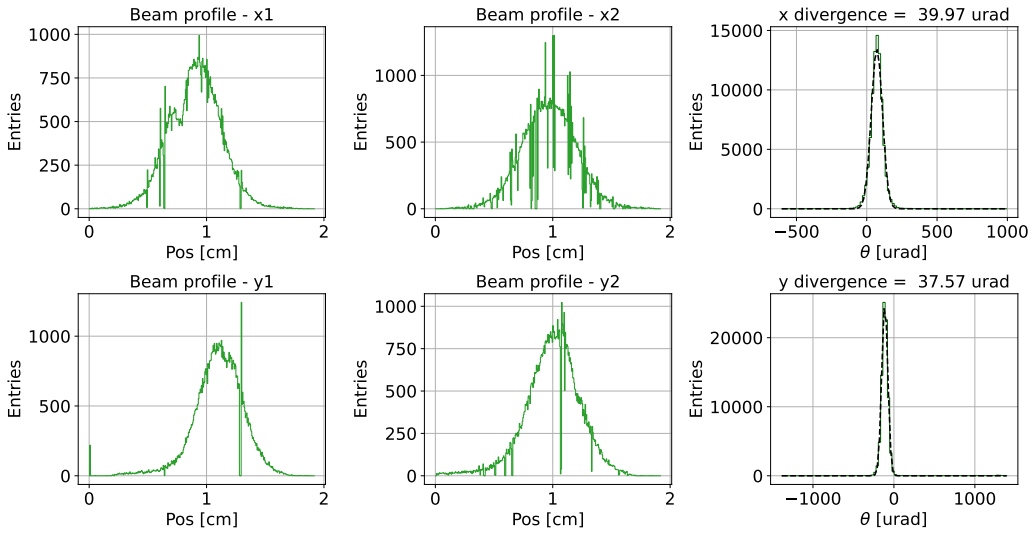

Figure 2.13: Beam profile and angular divergence for a 180 GeV/c positive pion beam as seen by the two upstream beam telescopes.

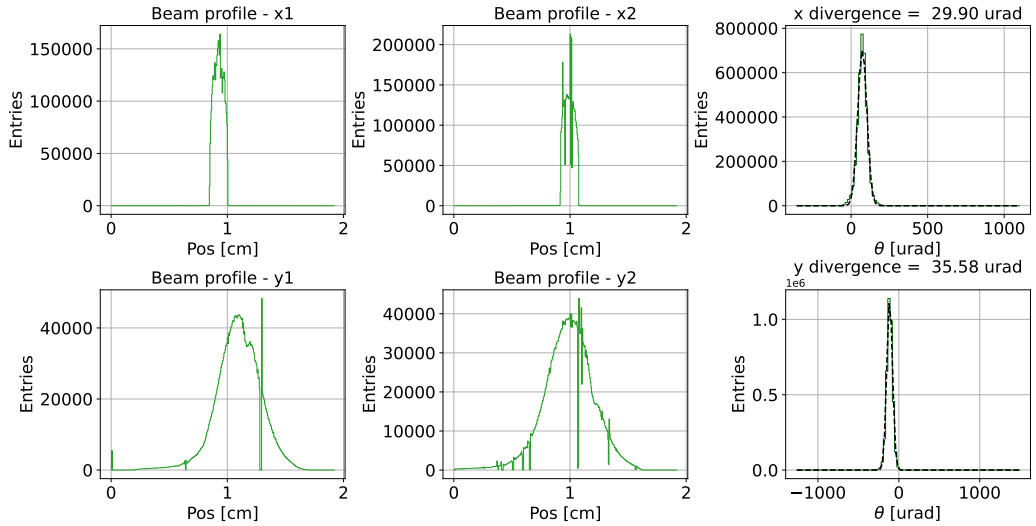

Figure 2.14: Beam profile and angular divergence for a 180 GeV/c positive pion beam as seen by the two upstream beam telescopes by triggering on a region approximately 1 mm wide along the x direction.

constrained in the PPE128-PPE138 areas. A complete description of the SPS extracted beamlines, including the H8 one, may be found in [72].

2.3 Frascati Beamtest Facility

The unique demands of the GALORE and crystal-based positron source experiments required an upgrade of the readout electronics of the silicon telescopes. The small section of the crystal, combined with the extremely reduced *angular acceptance*, required to trigger on a small part of the beam using just a 50 µm few strips (2-10) of a pair of telescopes placed $\sim$ 10 m away, to create an extremely thin and low divergence beam.

The first beamtest to verify the self trigger capabilities of the beam telescopes was performed in April 2023, at the BeamTest Facility (BTF) at the Frascati laboratory.

DAΦNE or DAFNE (Double Annular Φ Factory for Nice Experiments) is an electron-positron collider whose main purpose is to study the Physics of the kaons produced in the decay of the Φ mesons and the test of CPT violation; it is hosted at the INFN *Laboratori Nazionali di Frascati* (LNF, Frascati National Laboratories), a complex of laboratories based in Frascati, Italy. The DAΦNE accelerator complex includes a double ring lepton collider working at the center of mass energy of the Φ-resonance (1.02 GeV) and an

injection system, made of a S-band Linear Accelerator (LINAC), a 180 m long transfer line and an accumulator/damping ring [73].

Two beamtest facilities, namely BTF1 and BTF2, underwent a renovation process that was completed in 2020. Both experimental halls receive the primary beam accelerated by the LINAC. To broaden the momentum distribution of the incoming beam, a variable depth target (1.7 to 2.3 X_0) is employed [74]. In Figure 2.15, a schematic representation of the two experimental areas is presented,

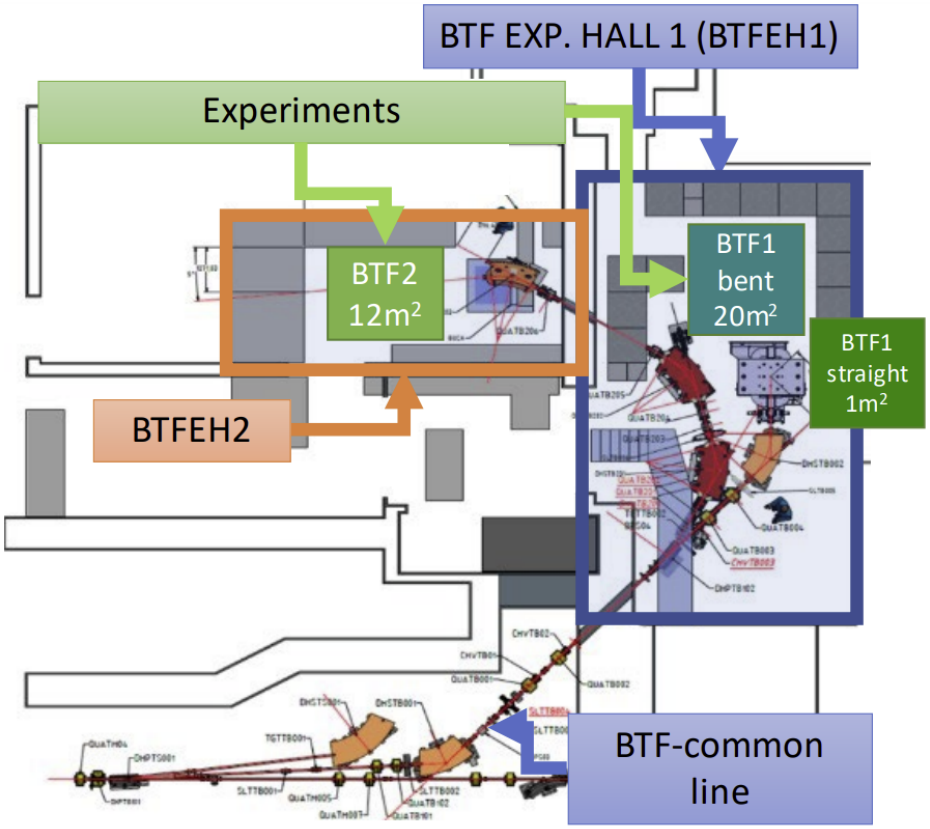

Figure 2.15: Layout of the Frascati BeamTest Facilities. Image from [74].

The renovation primarily focused on achieving a high-quality beam, with special attention given to factors such as beam size, divergence and background events, even at the lower end of the BTF energy range, which is in the range of a few tens of MeV/c. Even if both beamlines can be operated simultaneously thanks to a dipole connected to a pulsed magnet power supply, internal safety rules dictate that only one beamline is to be operated at a time.

The momentum dispersion is mainly introduced by the bending magnet, therefore the relative energy spread $\Delta E/E$ is determined by the magnets

and collimators configuration. However, for most of the configurations, a resolution better than 1 % can be obtained.

The average number of transported electrons (or positrons) is adjustable within a broad range, reaching up to 10×10^{10}. However, due to radioprotection considerations, the maximum intensity per bunch is restricted to 10×10^{6}. For the lower limit, the minimum number of particles is 1. Nevertheless, the intensity is controlled using collimators, allowing only a mean value to be set. For small numbers, the number of particles follows a Poissonian distribution, which tends toward a Gaussian as the mean number becomes $\gtrsim 20$. Therefore, a mean value smaller than 1 may be chosen to ensure that most events involve a single particle.

The BTF2 features an experimental area of $12\,\mathrm{m}^2$, providing a space for research groups to install and test their detectors. This beamline is capable of delivering a secondary electron beam up to $510\,\mathrm{MeV}/c$ while the primary beam can arrive to $700\,\mathrm{MeV}/c$ [74]. Each pulse is 10 ms long and the repetition rate is 50 Hz, depending on whether or not DAΦNE is operational.

Figure 2.16 presents a photo of the BTF2 experimental area, where the last bending magnet may be observed. The beamline is equipped with a remotely controllable table, and users have access to silicon pixel detectors (FitPix and TimePix3) to observe the beam spot, along with a lead glass calorimeter.

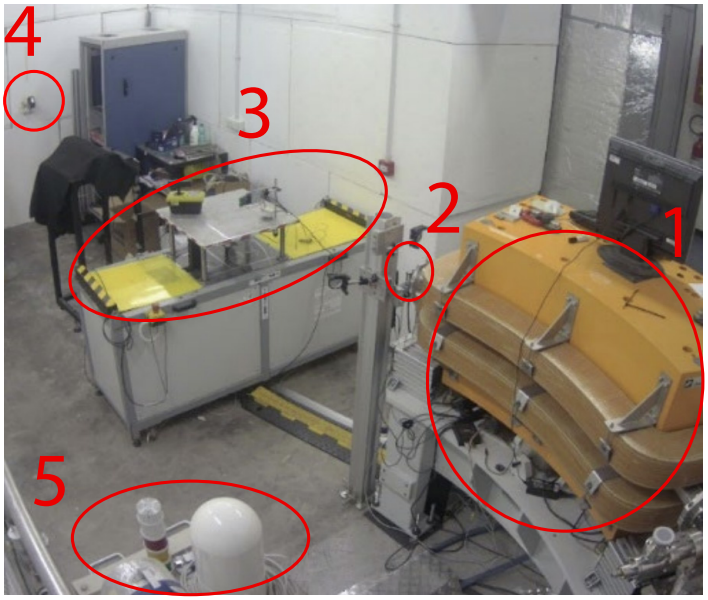

Figure 2.16: Photo of the BTF2 experimental hall: (1) last bending magnet; (2) silicon pixel detectors; (3) remotely controllable table; (4) laser to align equipments with the beam; (5) radiation monitor. Image from [74].

Figure 2.17 presents the beam profile and the angular divergence with an external trigger, i.e. considering the whole beam, while figure 2.18 regards the self-trigger mode with the modules in the *AND* configuration selecting ± 10 strips around the beam peak. Taking a y-slice of the beam results in a reduction of a factor 3 of the y angular divergence, going from 3.15 mrad to 1.02 mrad, keeping unchanged the x divergence. The smearing of the $y2$ peak in figure 2.18 is due to a noise trigger with a real particle in the region outside the trigger one.

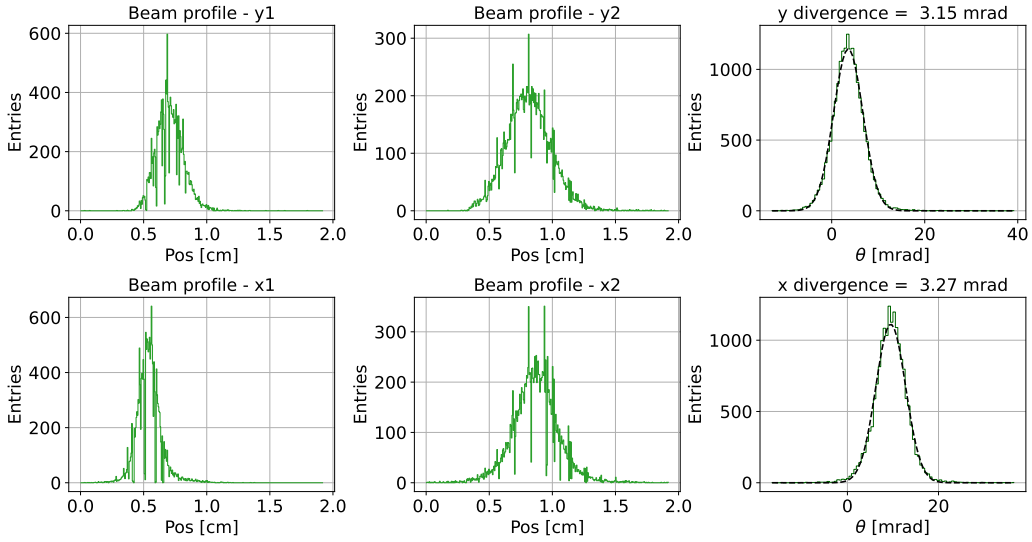

Figure 2.17: Beam profile and angular divergence for a 450 MeV/c electron beam at the Frascati BTF, triggering on a signal provided by the machine.

In this chapter a detailed description of the experimental test systems, and of several beamtest facilities for which these systems have been designed, have been provided. The following chapter is dedicated to the silicon microstrip detectors, the readout electronics and the data acquisition software.

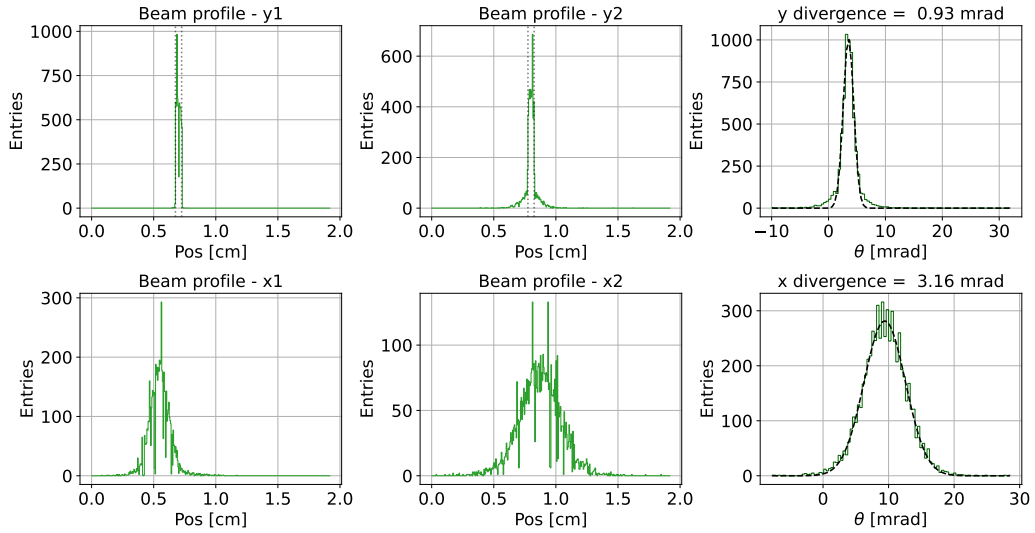

Figure 2.18: Beam profile and angular divergence for a 450 MeV/c electron beam at the Frascati BTF, triggering in the y direction on ± 10 strips across the beam peak (*AND* of the modules). The grey dotted lines represent the selected region; the y angular divergence has been reduced of a factor 3.

Chapter 3

The Tracking System

In the previous chapter, the experimental test layout, and the beamtest facilities upon which the system was designed, were presented.

The crystal-based positron source and the GALORE experiment, both relying on the channelling phenomenon, require high-resolution particle tracking for a reliable measurement of the crystal performance.

Silicon strip detectors have the adequate features for such a tracking system: coupled to low noise electronics and depending on their strip pitch, they can reach a spatial resolution of a few µm.

To allow the collection of a statistics large enough, they must be read out by a fast Data AcQuisition system, able to save only the strips that have detected the particle crossing

This chapter is dedicated to the description of the silicon strip tracking systems of the INSULAB group that have been used for the crystal tests. The chapter presents the silicon detectors features and their frontend and readout electronics, describing the upgrades that have been implemented for this thesis work. The last part of the chapter deals with the data acquisition and pre-processing software.

3.1 The INSULAB Microstrip Detectors

The INSULAB group has developed a variety of silicon microstrip tracking modules with different features and therefore to be employed in different scenarios. Two types of detectors will be described:

- a set of large area ($\sim 10 \times 10\,\mathrm{cm}^2$) single side detectors called Beam Chambers (BC)

- a set of smaller ($\sim 2 \times 2\,\mathrm{cm}^2$) single and double side high resolution (5 - 10 µm) detectors called Beam Telescopes.

3.1.1 The Silicon Beam Chambers

The *Beam Chambers* are large area silicon microstrip detectors based on the spare modules of the AGILE (Astrorivelatore Gamma a Immagini LEggero - Light Imager for Gamma-ray Astrophysics) satellite, a project selected by ASI (Agenzia Spaziale Italiana - Italian Space Agency) to observe γ rays in the 30 MeV - 50 GeV energy range [75] [76].

3.1.1.1 The Silicon Detector

The AGILE silicon detector is a single side 410 µm thick strip detector built on a 6-inch high resistivity ($\geq 4\,\mathrm{k}\Omega\,\mathrm{cm}$) substrate manufactured by HAMAMATSU PK and is presented in figure 3.1.

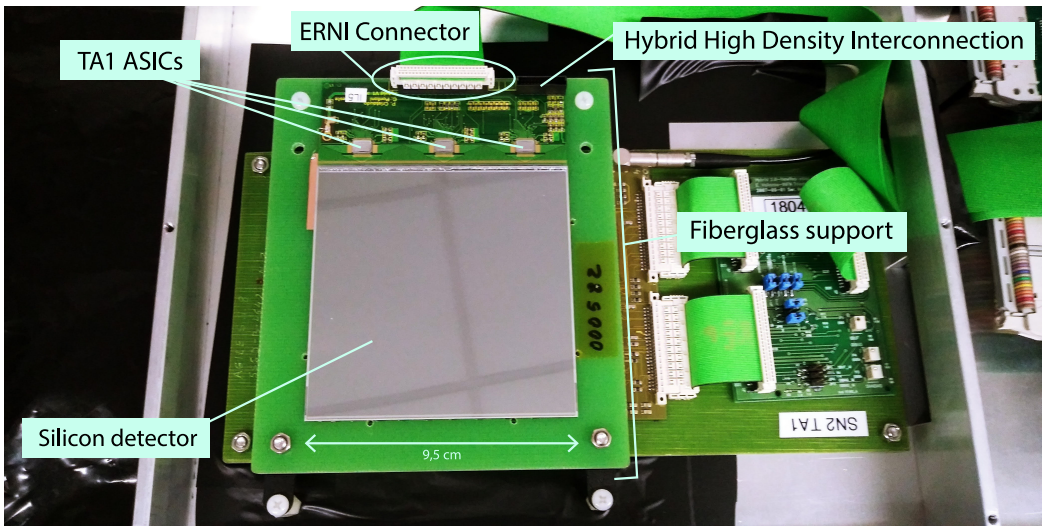

Figure 3.1: Photo of a silicon strip beam chamber, where the silicon detector, the readout ASICs and the HDI (High Density Interconnection) hybrid can be seen.

The physical strip pitch is 121 µm while the readout one is 242 µm. In fact the *floating strip* technique is employed, that is, all the 121 µm strips are properly biassed but only one strip out of two is read out. In this way the spatial resolution can be improved applying a center of gravity (COG) method to reconstruct the particle crossing position, keeping under control the power consumption. A total of 384 strips is read out, which results in a

sensitive area of $9.3 \times 9.3\,\mathrm{cm}^2$. Given the fact that the strip area is surrounded by the guard rings and the bias ring, the overall dimension is $9.5 \times 9.5\,\mathrm{cm}^2$.

The detectors are AC-coupled with a coupling capacitance of 527 pF measured at 10 kHz and an AC coupling Al resistance value of $4.5\,\Omega/\mathrm{cm}$. The bias resistor is 40 MΩ and the typical bias value for the silicon to be fully depleted lies in the 30 - 36 V range. The leakage current is $1.5\,\mathrm{nA}/\mathrm{cm}^2$. The measured spatial resolution resulted to be 40 µm in a wide range of incidence angles of the particles [77].

The Beam Chambers are well suited for the beamlines with a wide beam profile, such as the T9 line at CERN, or for setups that need to measure channelling in bent crystals with a large (few mrad) deflection angle, as in the case of the TWOCRYST beamtest, described in section 1.1.1.

3.1.1.2 The Readout ASICs

Each silicon detector is read out by three TA1 128-channel, low-noise and low-power ASICs. The TA1 ASIC has been designed by IDEAS[1] and produced by AMS[2] with 1.2 µm N-well BiCMOS (Bipolar Complementary Metal Oxide Semiconductor), double poly, double metal on epitaxial layer technology.

Each channel is made of a folded cascode Charge Sensitive preAmplifier (CSA), a CR-RC slow shaper, a sample and hold circuit (S&H) and a level sensitive discriminator, as shown in figure 3.2. Once an external trigger signal occurs, a *hold* signal is generated to sample the signal Pulse Height (PH) at the shaper output. The readout is a multiplexed differential analog readout with a maximum clock of 10 MHz; however during beamtests the ASICs are usually operated at 2.5 MHz or 5 MHz.

Given the presence of a discriminator, the TA1 ASIC, whose main features are summarized in table 3.1, is able to generate a trigger; the discriminator threshold is the same for all the 128 channels, and has to be set from outside the ASIC. The strips selected in the *trigger mask*, loading a bit pattern in a shift register, are put in OR. The possibility to select the strips to trigger on is a key feature for the on beam crystal characterization, since it is possible to select the part of the beam spot corresponding to the region where the crystal is placed. Moreover there is the possibility to disable noisy strips to avoid noise triggers.

The custom readout electronics, as will be described later, is designed to work at CERN, where beams are *spilled*, that is, a bunch of particles (lasting from hundreds of ms to seconds) is delivered approximately each minute. The raw events are stored in fast memories and transferred to the DAQ computer

[1] IDEAS, Oslo, Norway

[2] Austria Mikro Systeme International AG, Austria

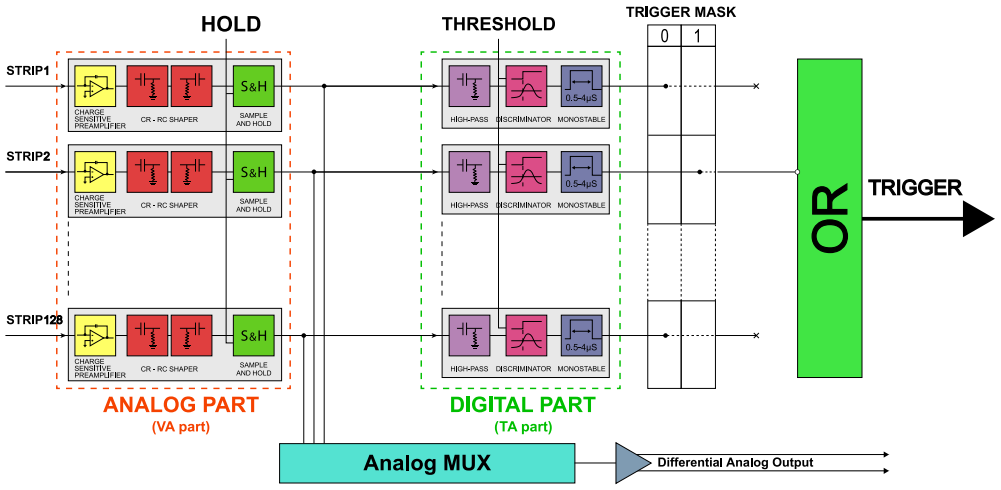

Figure 3.2: Schematic view of the TA1 ASIC. Starting from the left: the analog part (*VA part*), the digital part, responsible of the trigger generation (also indicated as *TA part*).

in the *interspill* period. Such memories present a maximum amount of data that can be stored (the exact number depends on the operation conditions), and avoiding to fill them with useless data allows to maximize the acquired Physics data.

3.1.2 The High Resolution Beam Telescopes

The spatial resolution may be improved by reducing the strip pitch. The INSULAB *Beam Telescopes* are a set of silicon detectors with a readout pitch of 50 µm which allows to reach a spatial resolution of 5 - 10 µm. In this section the detector itself and the different types of readout ASICs will be presented.

3.1.2.1 The Silicon Detector

This subsection is dedicated to the so called *VA2 Telescopes*, a set of six silicon microstrip tracking modules (*Tele A* to *Tele F*). Each module houses a high resistivity ($\geq 4\,\mathrm{k\Omega\,cm}$) 300 µm thick *double side* silicon microstrip detector, that is, a single silicon wafer with $p+$ strips on the *junction side* and $n+$ strips in the orthogonal direction on the *ohmic side*. By employing the double side layout, it is possible to build thinner detectors, and therefore to reduce the multiple scattering. On the other hand, the ohmic side electronics

Table 3.1: Main features of the TA1 ASIC.

ASIC name	TA1
Process (N-well CMOS)	1.2 µm
Surface	$4.85 \times 6.9\,\mathrm{mm}^2$
Thickness	$\sim 600\,\mu\mathrm{m}$
Number of channels	128
Input pad size	$50 \times 90\,\mu\mathrm{m}^2$
Input pad pitch	100 µm
Control pad size	$90 \times 90\,\mu\mathrm{m}^2$
Control pad pitch	200 µm
ENC at 2 µs of peaking time	$165 \pm 6.11/\mathrm{pF}$
Peaking time	1 - 3 µs
Dynamic range	±5 MIPs
Current gain	$\sim 20\,\mu\mathrm{A/fC}$
Gain	$25\,\mathrm{mV/fC}$

is referred to the bias value and not to 0 V. Therefore the ohmic side signals must be opto-coupled to be handled by the readout electronics.

The silicon detectors, presented in figure 3.3, have been manufactured by CSEM[3]. A one floating strip scheme is used on the junction side, with a $p+$ implantation every 25 µm and a readout pitch of 50 µm, while on the ohmic side no floating strip is present: there is a $n+$ implantation every 50 µm, which coincides with the readout pitch. 384 strips are readout on each side, resulting in a $1.92 \times 1.92\,\mathrm{cm}^2$ sensitive area. The spatial resolution is 5 µm on the junction side thanks to the floating strip while on the ohmic side is 10 µm [78].

The silicon detectors are DC coupled, and they are bonded to 150 pF external coupling capacitors to ensure the AC coupling with the electronics. The typical leakage current per strip lies in the 1.5 - 2 nA range, and the bias voltage required for the silicon to be fully depleted is in the 36 - 54 V range. For further details the reader can refer to [78].

3.1.2.2 The Readout ASICs

Each side of the CSEM silicon detectors is read out by three VA2 ASICs. The VA2 is a 128 channel radiation tolerant integrated circuit built with the 1.2 µm N-well CMOS (Complementary Metal Oxide Semiconductor) technol-

[3]Centro Svizzero di Elettronica e Microtecnica (Swiss Center for Electronics and Microtechnology.) , Neuchâtel, Switzerland

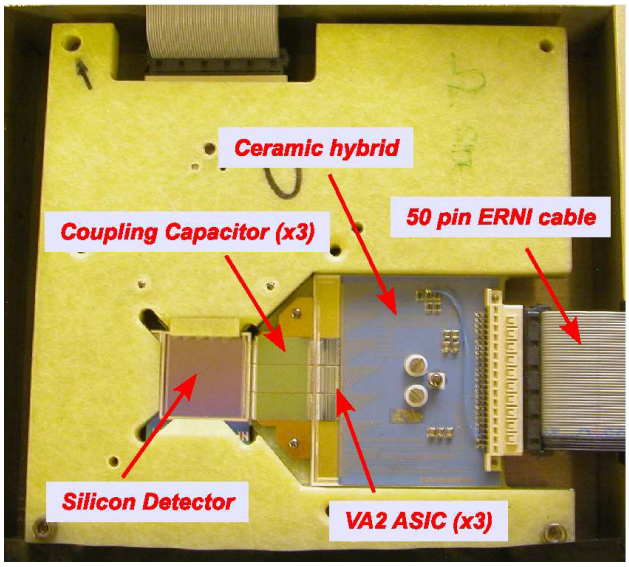

Figure 3.3: Photo of one of the Beam Telescope modules with a CSEM double side detector readout by the VA2 ASICs. Image from [78].

ogy.

They feature an analog part similar to the one of the TA1, namely a CSA, a CR-RC slow shaper and a S&H with a multiplexed analog differential output, but the digital part is not present. The main features are summarized in table 3.2.

3.1.3 Self Triggering Beam Telescopes

The so-called VISION Telescopes (Versatile and Innovative SIlicON Telescopes) consist in several modules featuring both single and double side silicon tiles from HAMAMATSU and FBK-irst, whose design is very similar and therefore they will be presented together in this section. For more details about these modules and their on beam characterization, the reader can refer to [78].

The key features of the VISION telescopes are the readout ASICs, which are capable of generating a trigger signal when a charged particle crosses a user defined subset of silicon strips, as in the case of the beam chambers.

3.1.3.1 The Silicon Detector

The FBK-irst silicon modules consist in a double side microstrip detector with a sensitive area of $1.92 \times 1.92\,\mathrm{cm}^2$. The HAMAMATSU ones have the

Table 3.2: Main features of the VA2 ASIC. Table from [78].

ASIC name	VA2
Process (N-well CMOS)	1.2 µm
Die surface	$6.18 \times 4.51\,\mathrm{mm}^2$
Die thickness	$\sim 600\,\mu\mathrm{m}$
Number of channels	128
Input pad size	$50 \times 90\,\mu\mathrm{m}^2$
Output pad size	$80 \times 90\,\mu\mathrm{m}^2$
ENC at 1 µs of peaking time	$80 + 15 \cdot C_d$ ($e-$ rms)
Power consumption	170 mW
Slow shaper peaking time	1 - 3 µs
Fast shaper peaking time	not present
Dynamic range	±4 MIPs
Current gain	$\sim 25\,\mu\mathrm{A/fC}$

same sensitive area but they are single side. Figure 3.4 presents some photos of the detectors.

In both cases the detectors have been built on a 300 µm thick high resistivity ($\geq 4\,\mathrm{k}\Omega\,\mathrm{cm}$) silicon. No floating strips are present in the HAMAMATSU detectors, and therefore the physical pitch is the same as the readout pitch, which is 50 µm.

The leakage current and the required bias voltage for the junction to be fully depleted are the same as for the VA2 telescopes.

3.1.3.2 The Readout ASICs

The self triggering capabilities are provided by the VA1TA (and VA2TA, which is very similar) ASIC, whose main features are reported in table 3.3.

The VA1TA presents the same analog part (VA part) of the VA2 ASIC, including the CSA, the CR-RC shaping filter, and a S&H, while the triggering signal generation is performed by the digital TA part. The sketch reported in figure 3.2 for the TA1 is valid also in this case.

The TA part consists in

- A charge sensitive amplifier, shared with the VA part.
- A CR-RC fast shaper with a peaking time of either 0.075 µs or 0.3 µs. The fast shaper is important for the trigger signal generation: in fact the trigger signal has to arrive before the peak of the analog signal that has to be sampled, which is produced by a slow shaper (with a peaking

(a)

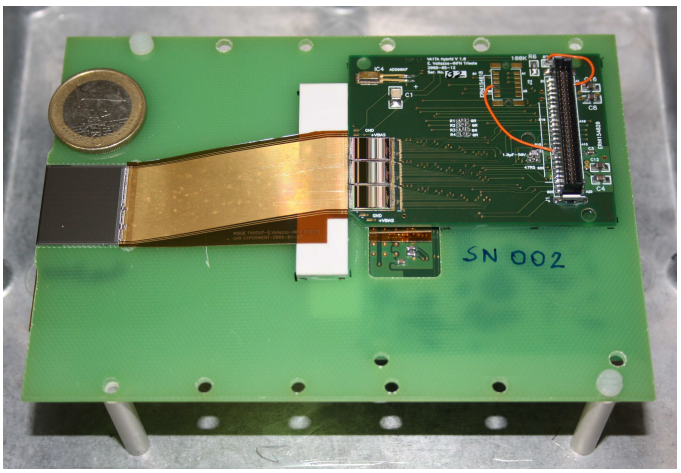

(b)

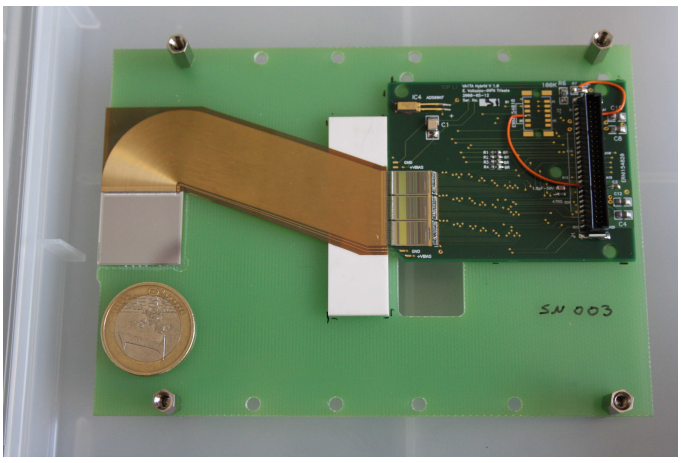

(c)

Figure 3.4: Photos of the VISION self triggering beam telescopes mounted on their fiberglass support: (a) FBK-irst module with the ASIC directly bonded to the silicon; HAMAMATSU modules with a (b) straight and a (c) bent upilex fanout. Image from [78].

Table 3.3: Main features of the VA1TA ASIC. Table from [78].

ASIC name	VA1TA
Process (N-well CMOS)	0.35 µm
Die surface	$9.28 \times 6.12\,\mathrm{mm}^2$
Die thickness	$\sim 725\,\mu\mathrm{m}$
Number of channels	128
Input pad size	$50 \times 90\,\mu\mathrm{m}^2$
Output pad size	$90 \times 90\,\mu\mathrm{m}^2$
ENC at 1 µs of peaking time	$180 + 7.5 \cdot C_d$ ($e-$ rms)
Power consumption	195 mW
Slow shaper peaking time	0.3 - 1 µs
Fast shaper peaking time	0.075 µs or 0.3 µs
Dynamic range	±10 MIPs
Current gain	$\sim 10\,\mu\mathrm{A/fC}$

time of 0.3 - 1 µs). For the TA1, the presence of only one shaper leads to a spread in the hold signal which degrades slightly the signal to noise ratio.

- A level sensitive discriminator with a tunable threshold in common to the 128 channels and a 4 bit trimming DAC to adjust the threshold on a channel by channel basis.

- A monostable to generate fixed width trigger signals.

Both positive and negative signals can be used to generate the trigger. The trigger mask is loaded with a shift register. The trigger output is the OR of all the strip discriminator outputs.

Some additional parameters, such as the shaping times of the slow and fast CR-RC shapers, the gain of the preamplifier, the trigger width and the trigger and DAC thresholds, can be configured through the *configuration mask*, that is a sequence of 680 bits which are written in a dedicated shift register. Figure 3.5 presents a sketch of the configuration mask.

For the GALORE beamtest, a module made of two single side HAMAMATSU tiles readout by VA1TA was placed close to the crystal, while a FBK-irst double side silicon detector readout by the VA2TA ASIC was put upstream. A module with two single side detectors has a thickness which is twice the one of a double side detector: such a layout was chosen to minimize the multiple scattering contribution.

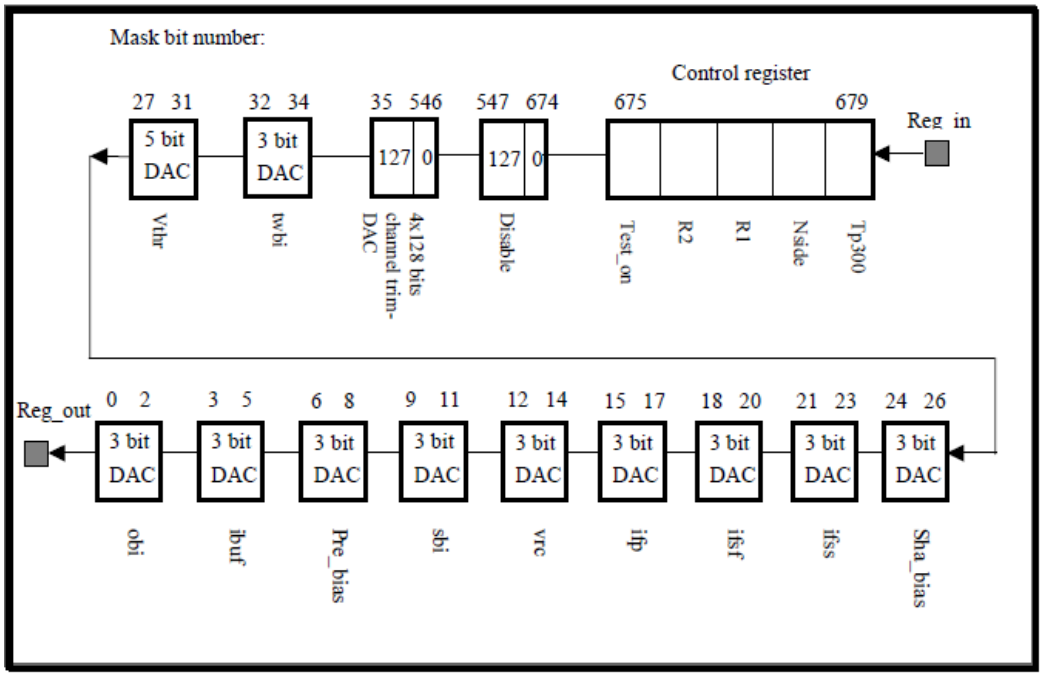

Figure 3.5: Sketch of the 680 bit VA1TA configuration mask to be written in a shift register, starting from bit 0. Image from [79]

3.2 The Readout Electronics

The electronics system may be divided into two main parts: the *frontend electronics*, placed close to each detector, whose task is to sample the analog signals from the silicon modules, and the *readout electronics*, which includes custom FPGA based boards that have to manage the trigger for all the detectors, digitize the sampled signals and store data in fast memories during the spill and transfer them to the DAQ PC at the end of the spill itself. Figure 3.6 presents a sketch of the readout electronics.

In the following, both the frontend and readout electronics will be described.

3.2.1 The Frontend Boards

The frontend electronics consists of the *Repeaters* and *Optocoupler boards*, which are presented in figure 3.7, where the main blocks are shown.

The repeater board is a 4 layer Printed Circuit Board (PCB), whose main tasks are the following:

- It provides the bias (generated by a battery or a power supply) to the

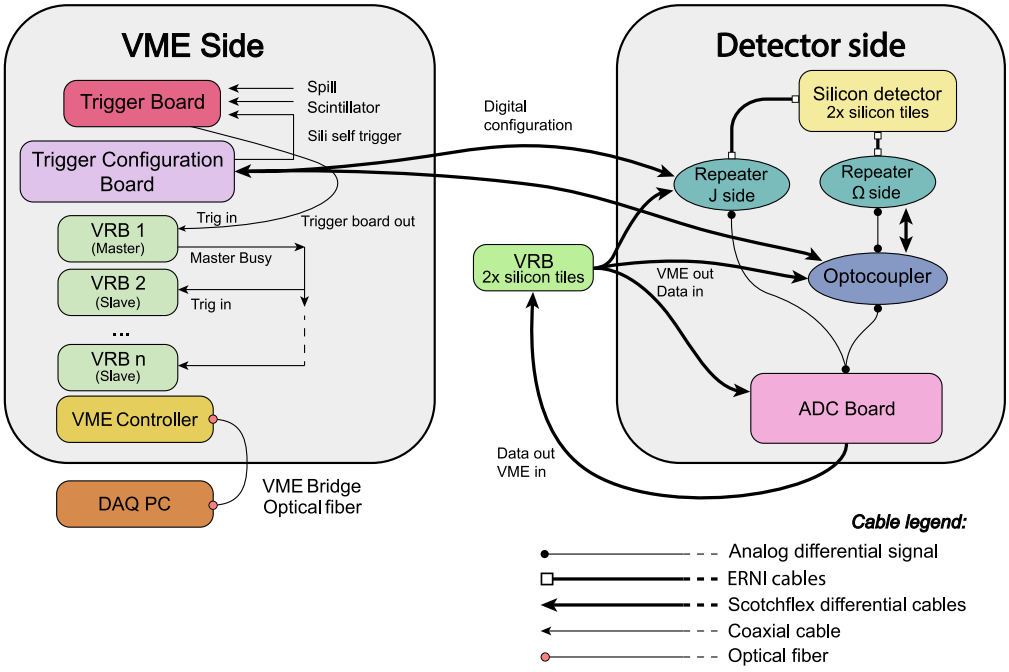

Figure 3.6: Sketch of the electronics chain for the double side telescopes.

silicon detectors.

- It provides the ± 2 V bias (generated by a power regulator on the repeater itself) to the ASICs. The ASIC and silicon biases are filtered separately to reduce the noise.

- It provides the digital configuration signals to the ASICs through ERNI cables. These signals are *differential* to be transported over a long distance without being affected by common mode noise. The RS422[4] differential signals are then converted by the repeater in single ended ones, as required by the ASICs.

- It amplifies the multiplexed output from the ASICs with a NE592 [80].

- It allows to set the configuration settings, such as the trigger thresholds and mask, for the ASICs with a *TA* part, that is, for the ASICs with the self triggering capabilities. The upgrades for the self triggering system required by the crystal-based positron source and the GALORE experiment concerned the test and implementation of this feature.

[4]RS422 (also EIA-422) is a technical standard that specifies the electrical characteristics of a digital signal transmission.

In the modules with a double side silicon detector, the ohmic side has a *ground* level which is not the external ground (0 V) but the bias voltage and all the signals have to be adapted. It is possible to set the reference of the electronics of both sides to 0 V but on the ohmic side, the voltage drop across the coupling capacitor may cause a pinhole in the capacitor itself thus shorting the preamplifier input and the bias resistor.

The role of the *optocoupler* is to adapt the ground level of the analog and digital signals, respectively with the HCPL 4562 and the ADUM 2400 integrated circuits (IC).

Custom ADC boards are placed close to each detector. Each board hosts four AD9220 12 bit ADCs, manufactured by Analog Devices, to digitize the sampled signal of each strip. Each ADC is in charge of digitizing one silicon plane, that is, an ADC board can be used for up to two silicon detectors.

The ADC board features an Altera Cyclone II EP2C8 FPGA, responsible of the communication with the VME Readout Boards (which will be described in section 3.2.2) through 16+16 I/O LVDS (Low-Voltage Differential Signal) lines, which are transmitted over flexible scotchflex flat cables.

3.2.2 The Readout Boards

The *readout electronics* includes both commercial and custom electronic boards in charge of handling the communication between the data acquisition software, running on a PC, and all the particle detectors and test equipment of the test system.

The term *controller* refers to a VME (Versa Module Eurocard) board designed to interface the readout boards and the data acquisition PC through the VME bus. The VME controller is coupled to a dedicated PCI board inside the DAQ PC, forming the so-called *bridge*.

The VME bridge is typically connected via an optical fiber cable to maximize the data transfer rate. For the beamtests described in this thesis, either the SBS Bit3 620 or the CAEN V2718 - A2818 [81] bridges were used. Figure 3.8 presents a CAEN VME bridge.

Up to 2011 the readout of the silicon tracking modules was based on commercial ADC modules, namely the CAEN V550 and the events were written on disk on an event-by-event basis [82].

The VME Readout Boards (VRB) are used to readout the digitized output signals and to temporarily store the data before being transferred to the PC to be saved permanently on a disk. Each VRB hosts a 50k cell FPGA (Altera EP2C50) with 581 kbit of internal RAM (Random Access Memory) and 4 PLLs (Phase Locked Loops) for the clock generation. The board has 16+16 LVDS inputs/outputs, 2+2 TTL (Transistor-Transistor Logic) inputs/outputs

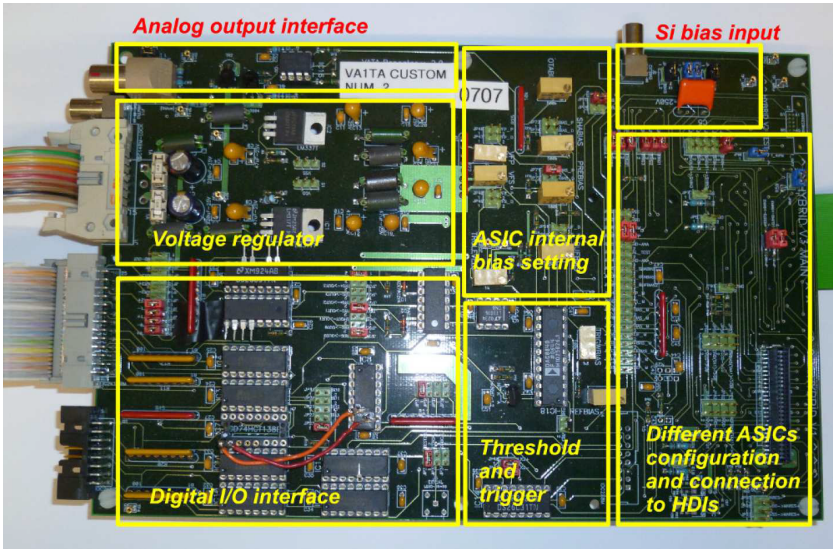

(a)

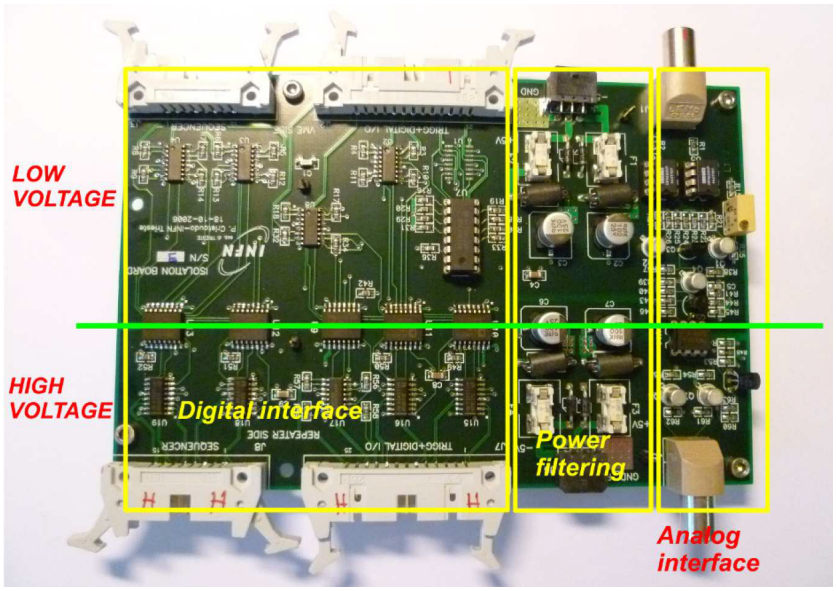

(b)

Figure 3.7: Photos of the frontend electronics: (a) the repeater board; (b) the optocoupler. The main blocks performing the different tasks are shown. Image from [78].

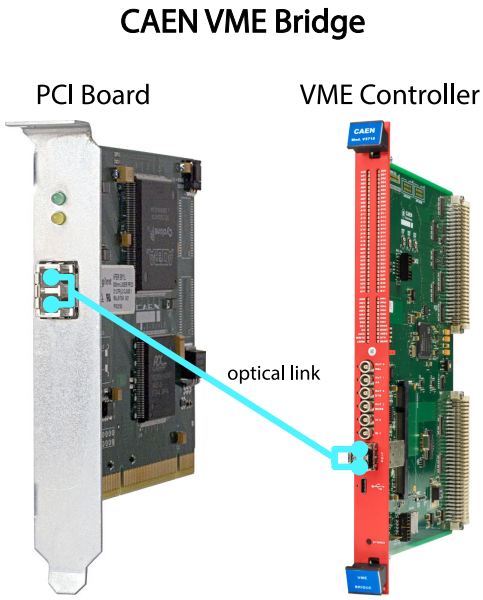

Figure 3.8: Photo of the CAEN VME Bridge: PCI board (left) and VME controller (right) which are connected through an optical fiber. Image from CAEN website.

and a TLK1501 Gigabit link. The FPGA is also in charge of the interface with the VME bus.

The board features 4 RAM blocks for a total of 4×10^6 32-bit words where the data from the silicon trackers are buffered during the spill, and transferred to the PC in the interspill period, since this operation requires a significant amount of time which would limit the data acquisition rate. More details about these electronic boards may be found in [83].

Each VRB is in charge of reading out one silicon module, which is composed of two strip planes. There are two main operation modes of the VRBs:

- Normal mode: all the 2×384 strip values are stored for each event
- Zero suppression mode: only the strips above a given threshold are stored in the RAM. In this operation mode, a total of 2×16 strips can be saved for each event.

In the *zero suppression* mode, a threshold is chosen in terms of the noise rms of each strip.

The possibility of working in zero suppression is strictly related to the silicon module noise, which consists of the intrinsic noise (due to the silicon strip leakage current and to the ASIC) and of the common mode (CM) one.

The CM noise affects all the strips in the same way and is due to the external noise on the detector bias line [78]. When working in normal mode, the CM contribution is computed and subtracted on an event by event basis, using all the strips read out by an ASIC which have seen no signal. This procedure cannot be applied when in zero suppression. Thus, for the zero suppression mode to be efficient it is important that the CM noise is low.

Figure 3.9 presents a photo of a VRB, where the main blocks are indicated. Each VRB features a single 68 pin 3M P50E-10011-SR1-EA connector, while the input and output signals travel on a 16 LVDS line through a scotchflex flat cable: an adapter board (IDC adapter) is therefore employed.

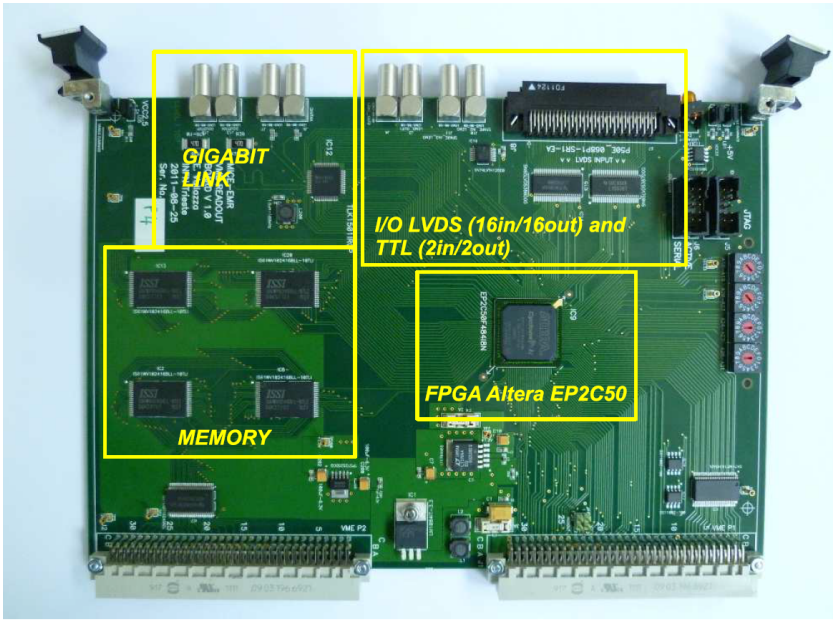

Figure 3.9: Photo of a VRB (VME Readout Board), where the main blocks are indicated.

The INSULAB silicon tracking system is a clear example of the advantages of a modular test system based on the VME bus: the system can be operated with a different number of silicon modules, using one VRB for each module and providing each VRB with a different VME address. One board acts as master: it receives the trigger signal from the trigger board and produces in turn a *busy* signal, which is used as the trigger for the other (slave) VRBs. Each VRB generates also the *hold* signal at a precise time after the trigger: this is the time at which the analog signal from each strip is *sampled* by the sample and hold circuit.

The *trigger board* is a VCB (VME Cyclone Board) board, that is a VME board with an Altera Cyclone FPGA. This board features 4+4 TTL

input/output and 4+4 NIM input/output digital signals. Unlike the VRB, it does not include additional RAM. The main task of the trigger board is to manage the control signals, such as the spill signal, a logic signal that remains HIGH during the spill period and LOW otherwise. The trigger board receives signals from different particle detectors, including plastic scintillators generating the trigger or Čerenkov detectors to select the particle type. Performing logic operations like OR or AND, the trigger board generates the trigger signal for the whole system.

The VCB boards are multi purpose, and depending on the firmware loaded on the FPGA, they may perform different tasks. This is the case of the *trigger configuration boards*, identical to the trigger boards from the hardware point of view, but that have been programmed to load the correct trigger masks and thresholds on the ASICs of the detectors with self trigger capabilities.

The trigger configuration boards can control a single silicon tracking module, and can be extended to control a total of four silicon planes with a daughter board plugged on an extension connector.

This board receives from each silicon module the self generated trigger signal, when one of the chosen strips exceeds the programmed threshold. The FPGA can perform logical operations on the trigger signals to produce a single trigger signal, that is the trigger from the silicon detectors. This signal is then fed into the trigger board, where it can be used together with other detectors.

For a scenario where 4 tracking modules are installed, as for a typical crystal characterization beamtest, if the overall noise of each module allows a large enough cut for the zero suppression in order to have less than 5 strips per module above threshold and a 2.5 MHz clock is used, the readout sequence requires:

- $384 \times 0.2\,\mu s = 76.8\,\mu s$: it is the so called *multiplexing time*, that is, the time required for the analog sampled pulse height of each strip to be transferred on a single differential line (multiplexed) to the ADC, where the analog to digital conversion takes place.

- 5 strips $\times$ 8 sides $\times\, 5\,\mu s$ VME Cycle $= 200\,\mu s$: it is the time needed to transfer the data to the data acquisition computer, through the VME bus.

Thus the overall readout time for each event would be $\sim 300\,\mu s$, corresponding to a maximum acquisition rate of $\sim 3\,kHz$ [82].

However, the CERN beamlines can provide only a *spilled beam*, that is, a bunch of particles, whose exact parameters (such as duration or intensity) depend on the beamline and the beam configuration. A typical duration may

be 400 ms for T9 and around 5 s for the North Area beamlines, and a spill is delivered every 30 - 90 s, depending on the machine cycle.

The new readout electronics has been developed to minimize the dead times, and therefore exploit as much as possible the beam. The reduction of the dead time implies the possibility to acquire statistics faster, and some beamtests need such an improvement.

3.3 The Data Acquisition Software

The DAQ system is controlled by a sophisticated software running on a PC where a Linux operating system is installed. The source code consists of a set of C routines which are called by a GUI (Graphical User Interface) written in Tcl (Tool Command Language), which is a dynamic programming language. The main tasks performed by the DAQ software are the following:

- It defines the trigger logic to be implemented in the trigger board.
- It allows to load the trigger mask and the trigger thresholds for the ASICs with self trigger capabilities through the trigger configuration board.
- It sets the hold time for all the silicon detectors and generates the clock for the readout ASICs.
- It allows to acquire and load the pedestal for the silicon detectors.
- It controls the goniometer stages.
- It handles the full data acquisition process.

Different acquisition modes are implemented in the DAQ software. By exploiting a random trigger, it is possible to acquire the *pedestal*, namely the baseline of the readout electronics chain of each silicon strip, which has to be subtracted in order to compute the correct pulse height.

Figure 3.10 presents the windows of the DAQ software. In particular, figure 3.10a is the main window, from which the different features of the DAQ software may be accessed. The DAQ software assigns a unique 6 digit number to each run, which is shown in the "FILE" label in this window.

The DAQ software supports two main acquisition modes:

- Single data taking (figure 3.10b): the upper part of the tab allows to choose the trigger logic for the trigger board. This tab allows to program the number of events to acquire (Nr of events); anyway the DAQ can be stopped manually. Two different "Run types" are supported:

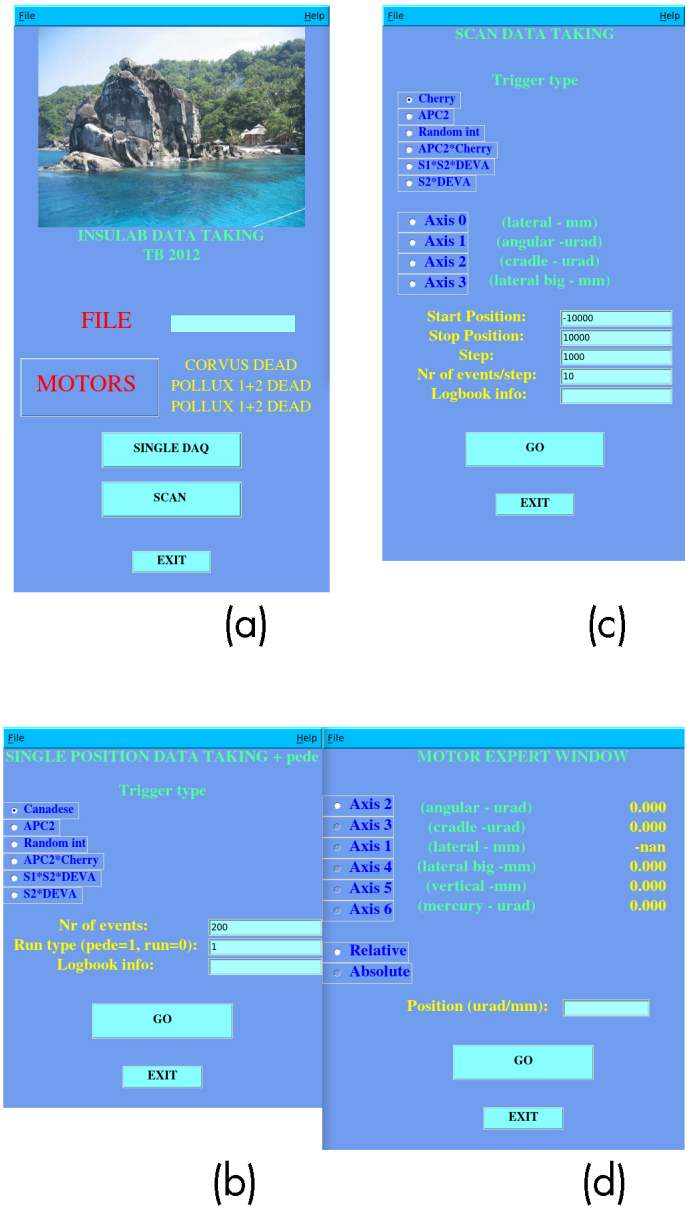

Figure 3.10: Screenshots of the DAQ software windows: (a) main window, (b) single DAQ tab, (c) scan of a goniometer stage and (d) window for the manual movement of the goniometer stages.

  - Normal run: an event is associated to each trigger received by the DAQ system, which is the result of the logic implemented in the trigger board. Each event contains the information recorded by all the detectors when the trigger arrives.
  - Pedestal run: by exploiting a random trigger when particles are not crossing the detectors, the pedestal of the silicon strip trackers can be measured.

- Scan data taking (figure 3.10c): this tab allows to perform a set of normal runs varying the position of one of the goniometer stages. In particular, the start position, the end position, the step and how many events to acquire at each step should be provided.

Figure 3.10d presents the tab to manually move the goniometer stages. This tab supports both relative and absolute movements.

The DAQ software, through the VME bus, manages the relevant signals for the readout electronics, such as the clock, the hold and the digital reset of the ASICs. The raw data are saved in the HBOOK compressed format at the end of each spill. Depending whether or not the zero suppression technique is used, a maximum of 16 strips per silicon module or the information of all the 384 strips are saved. In the zero suppression case, the pedestal is subtracted before saving the data.

An offline *stripping* procedure, based on a FORTRAN code, first determines the number of clusters, which are defined as the groups of neighboring strips where the particle deposits its charge, for each silicon module. The crossing position can be reconstructed with a COG algorithm, that is, the weighted mean of the strips, using the deposited charge as weight, is computed. The stripping software finally saves, for single cluster events, the crossing positions in ASCII files, one per each spill.

Some Python scripts can package the information of the ASCII files inside ROOT or HDF5 compressed files, to match the requirements of different data analysis softwares. If the software is not running in zero suppression mode, the stripping procedure can also subtract the common mode on an event by event basis.

Additional VME boards may be present in the system, such as the *digitizers*, capable of sampling the waveform of other detectors and which are readout by the DAQ software on an event by event basis. This is the case for the signals of light detectors such as Silicon PhotoMultipliers and PhotoMultiplier Tubes (SiPM and PMT) employed to read out the scintillating light from plastic scintillators, scintillating crystal calorimeters or Čerenkov detectors. The DAQ software saves the waveforms sampled in a window of a given width

and with a frequency and resolution which depend on the digitizer board. The DAQ software can compute the maximum amplitude of the waveform and the time with respect to the trigger at which such maximum is reached. All these values are saved in the data files together with the complete waveforms themselves.

Chapter 4

The Characterization of The Self Triggering System

The experimental requirements for the beamtests of the crystal-based positron source and the GALORE experiment required the upgrade of the electronics of the tracking detectors to enable the self generation of the trigger signal.

This chapter is dedicated to the description of the laboratory and on-beam characterization of the self triggering system capabilities which were performed before the beamtests to ensure that the upgraded system matched the requirements.

4.1 Laboratory characterization

The upgrade of the readout electronics consisted in three main steps:

- The repeater boards needed to handle different signals with respect to the usual configuration, which resulted in changing few components and modifying the connections between the components themselves.

- The firmware of the trigger configuration board was upgraded to provide the trigger thresholds and masks to the ASICs and to implement the trigger logic to generate the final trigger signal from the silicon detectors.

- Dedicated routines were implemented in the DAQ software to load the trigger thresholds and masks, which are provided to the ASICs through the trigger configuration board, and to select the logic for combining the trigger signals from each silicon module.

4.1.1 The VA1TA Laboratory Test

The preliminary laboratory tests of the ASICs may be divided into two categories:

- The *Noise Threshold Scan* consists in studying the trigger rate for each strip as a function of the threshold using only noise, that is, without any particle source. This scan allows to identify noisy channels that have to be disabled during the data taking.
- The *Analog Response* of each channel of the ASIC can be tested providing an external calibration signal to the channel itself and digitizing the shaped signal. This test is important to ensure that the HDIs work, before bonding the silicon detectors to the HDIs themselves.

The noise threshold scan has been performed setting the VA1TA trigger threshold (in the -40 - 40 mV range), with the 8 bit DAC on the repeater board. The VA1TA has the possibility to reduce the channel by channel threshold spread with a 4 bit DAC to trim the local threshold voltage for each channel (cfr. figure 3.5); this feature has not been used.

Figure 4.1 presents the trigger rate as a function of the threshold for each strip of two silicon modules readout by the VA1TA ASICs for 1 s long acquisitions. It is possible to see that most of the strips have zero counts, accordingly to the fact that no particle source is present. Few vertical lines may be identified, with an intensity that decreases as the threshold increases. Such lines correspond to noisy strips, which trigger without an energy deposit. These strips can be excluded from the trigger logic, even if the chosen trigger region includes them, by setting the *disable bit* of the corresponding channels (figure 3.5).

The plot also proves that it is possible to set a low threshold and, if the noisy strips are excluded, the trigger will be generated only by physical events. The exact value to be used must be verified for each experimental setup, as the noise depends on several factors, for instance the noise of the electrical network to which the power supplies are connected. By using the AND of two detectors in the trigger logic, the probability of noise triggers may be largely reduced.

Once understood the behavior from the trigger point of view, the analog performance of the ASICs can be tested with a calibration signal. In fact, each channel features a coupling capacitor which may be connected to an external signal (not related to the one produced by the silicon strip) to independently test the analog and digital parts of each channel.

For the VA1TA, this operational mode may be achieved by setting the *Test_on* bit (cfr. figure 3.5) in the loaded mask. The repeater board features

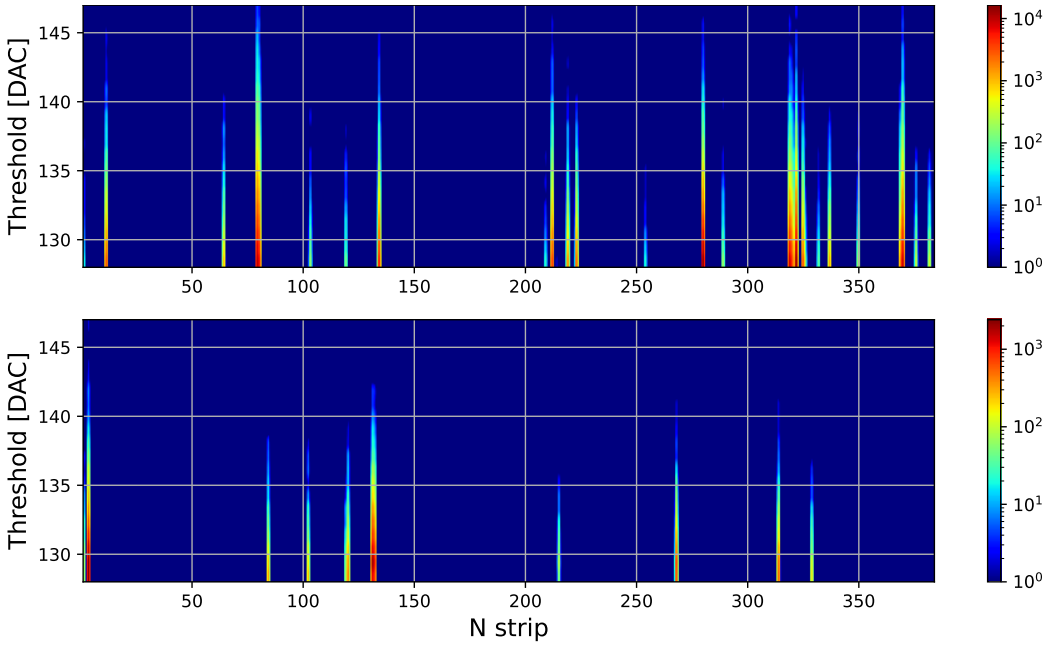

Figure 4.1: Trigger rate as a function of the threshold for each strip of two silicon modules for 1 s long acquisitions. Most of the strips have zero counts, that is, the noise trigger rate is low, and it is possible to set a low threshold for triggering on physical events. The noisy strips can be disabled by the DAQ software.

an analog input which can be used to provide a calibration signal to the chosen channel of the ASIC.

A step signal with an amplitude in the 10 - 50 mV range was used. The shaped signal was digitized by the ADC boards. In fact the readout of the pulse height of the silicon strips is based on a sample & hold circuit, which samples the value of the waveform itself when the hold signal arrives, and *holds* this value till the completion of the readout procedure. The sampled pulse heights are then multiplexed, to be digitized one after the other by the ADC. By varying the hold time, it was possible to sample the shaped signal at different times, which corresponds to digitizing the shaped signal itself. This procedure cannot digitize a single waveform, but each point is sampled from a different signal: thus, five points corresponding to each hold value were acquired to be then averaged.

Each waveform has been fitted with the following function:

$$y(t) = k(t - t_0)\, e^{-(t-t_0)/\tau} + c \tag{4.1}$$

where the vertical offset c was added to include the pedestal and t_0 is a horizontal offset which is needed given the fact that the test signal is delayed by a few hundreds of nanoseconds with respect to the acquisition trigger in order to evaluate the baseline. The maximum of this function is reached at $t = \tau$, where the function is $y(\tau) = k\tau/e + c$. The amplitude of the signal, namely the difference between the maximum and the baseline, is $k\tau/e$. Figure 4.2 presents a few examples of the digitized waveform of a channel (green) and the fitted curve (orange) for a 10 mV calibration signal. In some cases, when a channel was apparently dead, considering the next channel (black), the signal was found to be there. This may mean that the two channels are shorted. Figure 4.2a presents a working channel, figure 4.2b a channel where the signal is found in the next (black) channel. Finally, figure 4.2c presents an example of a really dead channel, where the signal is neither found in the channel itself nor in the next. The system in fact has not saved also the previous channel so this possibility cannot be verified.

Figure 4.3 presents the waveforms of the first 25 channels of an ASIC; it is possible to see that channel 10 is clearly dead, since there is no output.

Figure 4.4 presents the peaking time (first plot) and the peak amplitude extracted from the fit without (second plot) and with (third plot) the baseline subtraction on a channel by channel basis.

Figure 4.5 presents the histograms of the peaking times and peak amplitudes of the waveforms for each ASIC for a 10 mV calibration signal; the channels, where the fit has not converged optimally, have been excluded. The mean value and the standard deviation are also reported. The plots show

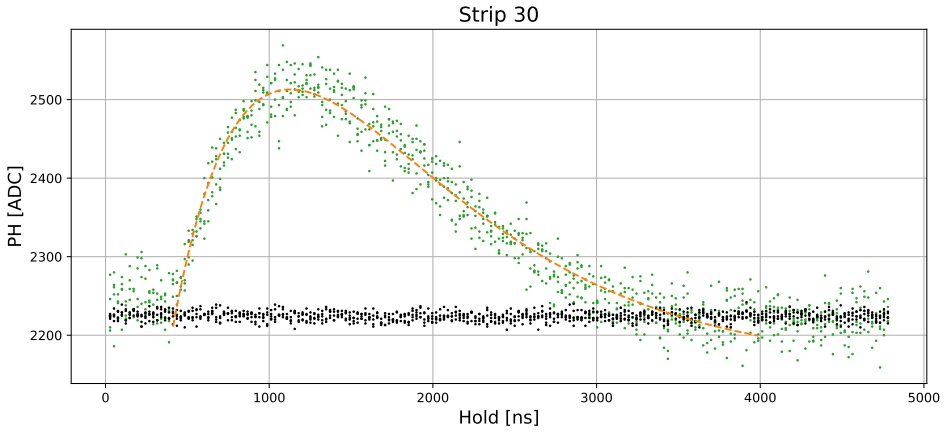

(a)

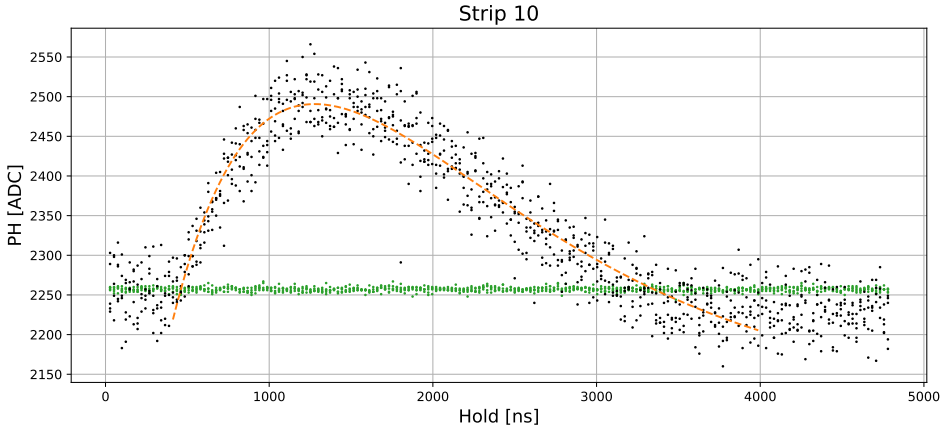

(b)

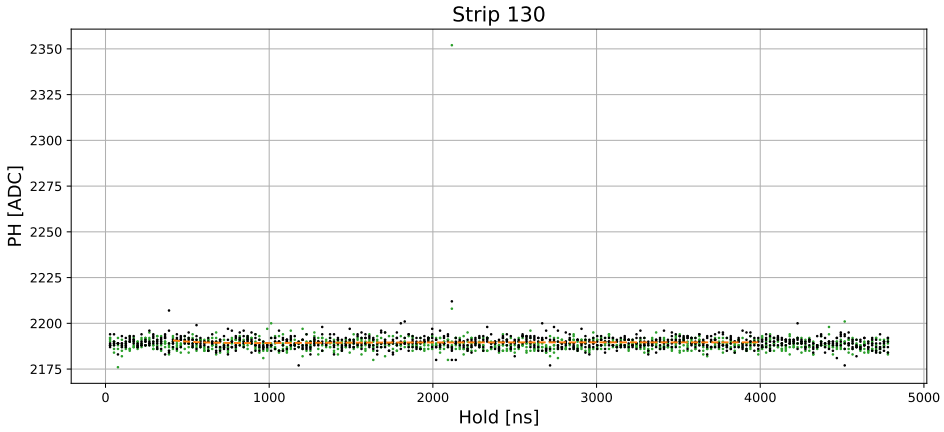

(c)

Figure 4.2: A few examples of the digitized waveform of a channel (green) and the fitted curve (orange) for a 10 mV calibration signal for the VA1TA: (a) a working channel; (b) a channel where the signal is found in the next (black) channel; (c) a dead channel.

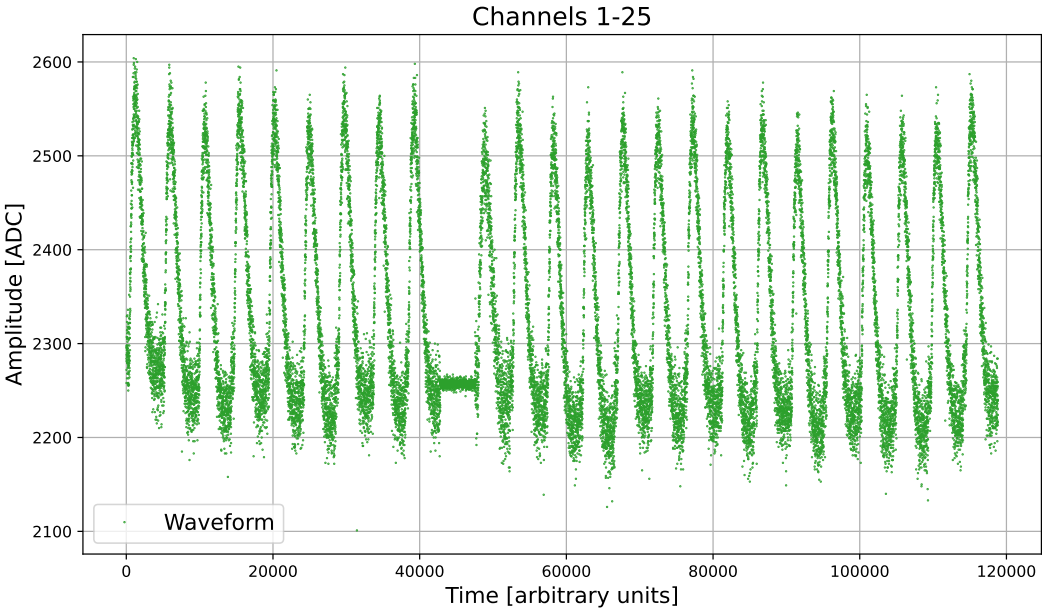

Figure 4.3: Waveforms of the first 25 channels of a VA1TA ASIC for a 10 mV calibration signal; channel 10 is clearly dead, since there is no output.

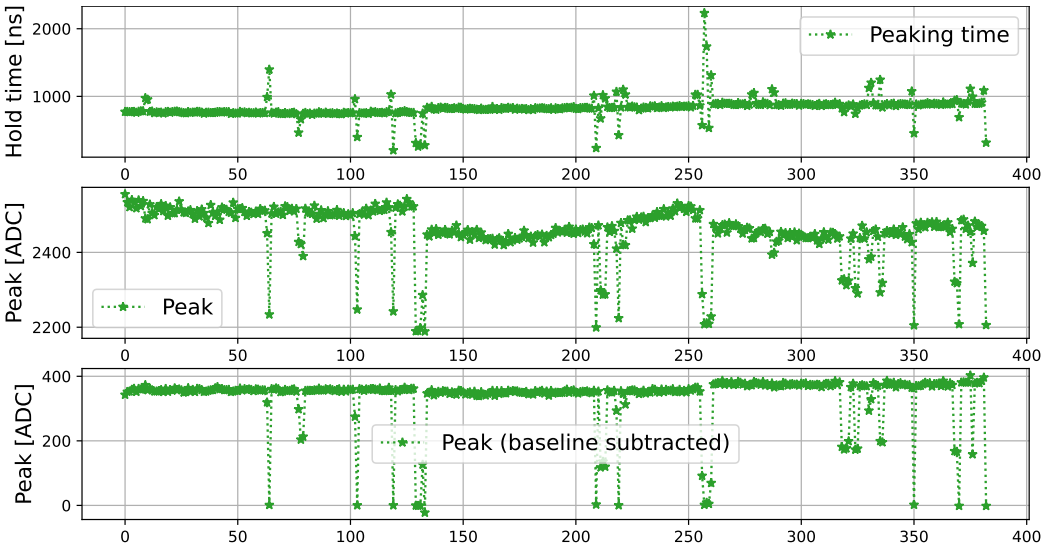

Figure 4.4: Peaking time (first plot) and the peak amplitude extracted from the fit for a 10 mV calibration signal without (second plot) and with (third plot) baseline subtraction on a channel by channel basis for the VA1TA ASIC.

that the three ASICs performance is very similar: the peaking time mean values have a maximum difference of slightly more than 100 ns but, given the shape of the analog signal, this is not a problem for the data taking. As far as the amplitudes are concerned, the mean values are very similar and the spread among the channels of each ASIC is around 1-2%.

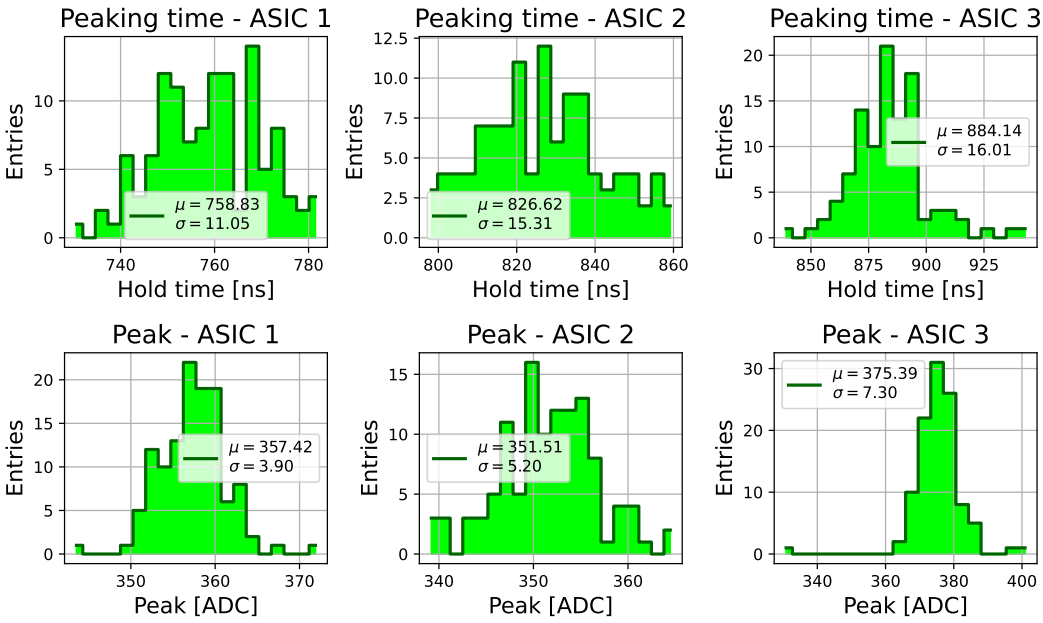

Figure 4.5: Histograms of the peaking times and peak values for each VA1TA ASIC, where the channels, where the fit has not converged optimally, have been excluded. The mean value and the standard deviation are also reported.

Finally, figure 4.6 presents the mean pulse height for each ASIC as a function of the amplitude of the calibration signal. From the plot it might be seen that the second (orange) and third (green) ASICs are starting to slightly saturate, while the first one (blue) is linear in the considered range.

4.1.2 The VA2TA Laboratory Test

The characterization with an external calibration signal has been performed also for the VA2TA ASIC. Despite having a dynamical range smaller than the VA1TA one (± 4 MIPs compared to ± 10 MIPs), the VA2TA has a larger current gain ($\sim 25\,\mu A/fC$ compared to $\sim 10\,\mu A/fC$) with respect to the VA1TA ASIC. It was therefore necessary to use the 5 V range for the ADC chips, although they are usually operated with the 2 V range to avoid

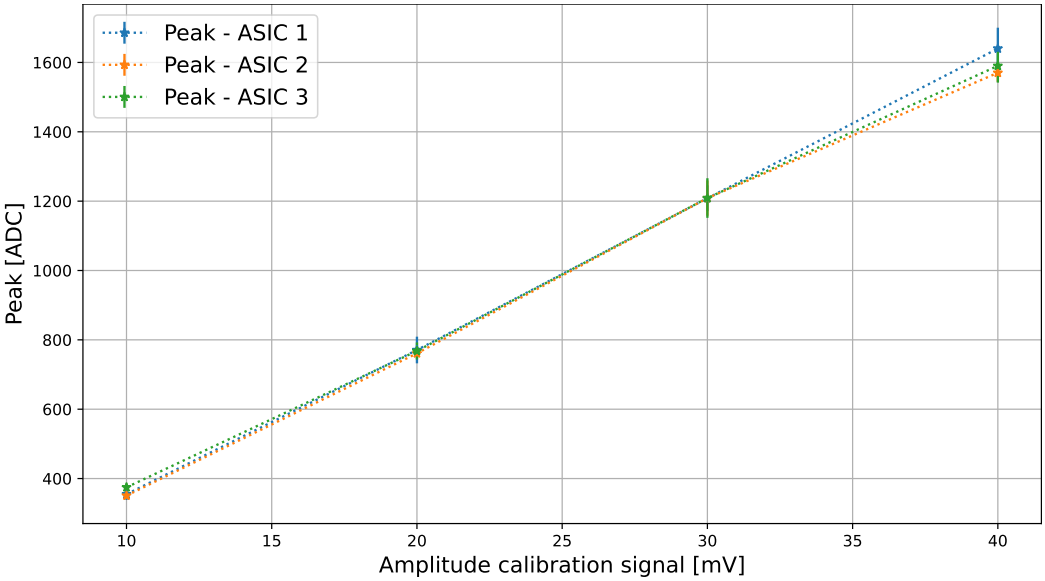

Figure 4.6: Mean pulse height for each VA1TA ASIC as a function of the amplitude of the calibration signal.

the saturation of the ADC itself. A calibration signal in the 5 - 25 mV range has been used.

Figure 4.7 presents an example of a digitized waveform of a channel (green) and the fitted curve (orange) with equation (4.1) for a 10 mV calibration signal. As for the VA1TA, the waveform of the next channel is presented (black). However, the signal has never been found in the next channel.

Figure 4.8 presents the waveforms of the first 25 channels of the first ASIC: it is possible to see that the first channel does not work properly.

Figure 4.9 presents the peaking time (first plot) and the peak amplitude extracted from the fit without (second plot) and with (third plot) the baseline subtraction on a channel by channel basis.

Figure 4.10 presents the histograms of the peaking times and peak amplitudes of the waveform for each ASIC for a 10 mV calibration signal; the channels, where the fit has not converged optimally, have been excluded. The mean value and the standard deviation are also reported. As far as the peaking time is concerned, the parameters chosen for these ASICs led to a long shaping time (which means that the signal to noise ratio is better); the spread between the values of the 3 ASICs is similar to the VA1TA case. The peak amplitudes are larger than the previous case and the spread among the channels of each ASIC is around 6%.

Finally, figure 4.11 presents the mean pulse height for each ASIC as a function of the amplitude of the calibration signal. From the plot it might

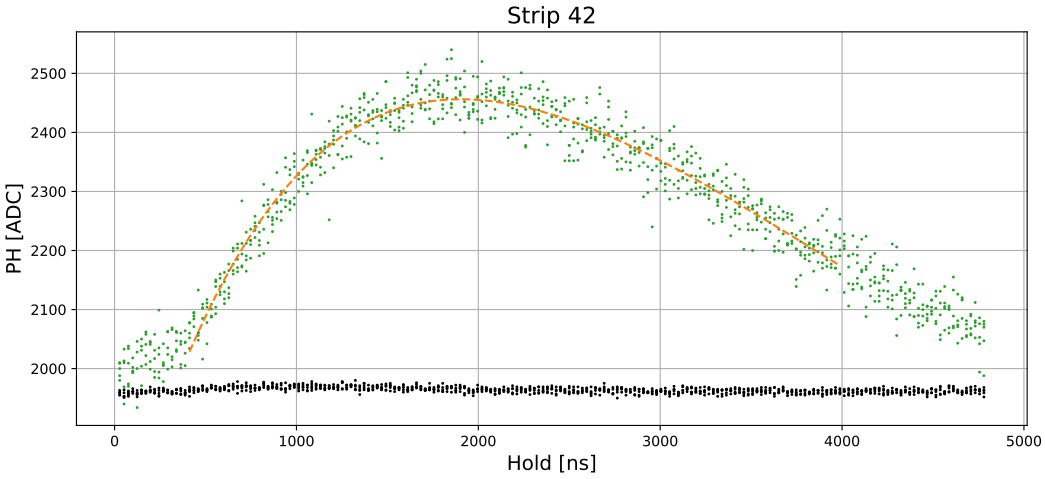

Figure 4.7: Example of the digitized waveform of a channel (green) and the fitted curve (orange) for a 10 mV calibration signal for the VA2TA.

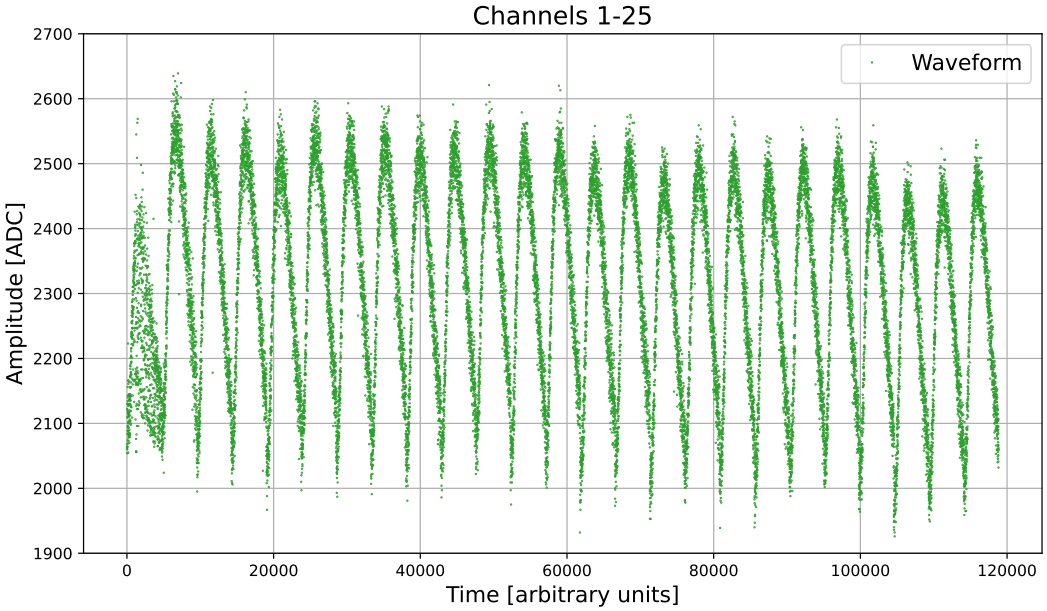

Figure 4.8: Waveforms of the first 25 channels of a VA2TA ASIC for a 10 mV calibration signal.

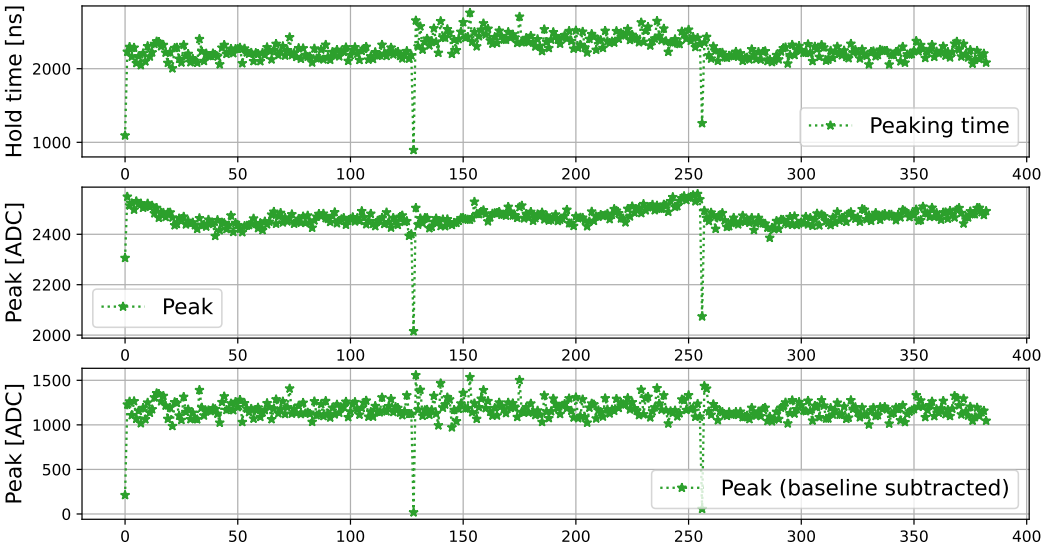

Figure 4.9: Peaking time (first plot) and the peak amplitude extracted from the fit for a 10 mV calibration signal without (second plot) and with (third plot) baseline subtraction on a channel by channel basis for the VA2TA ASIC.

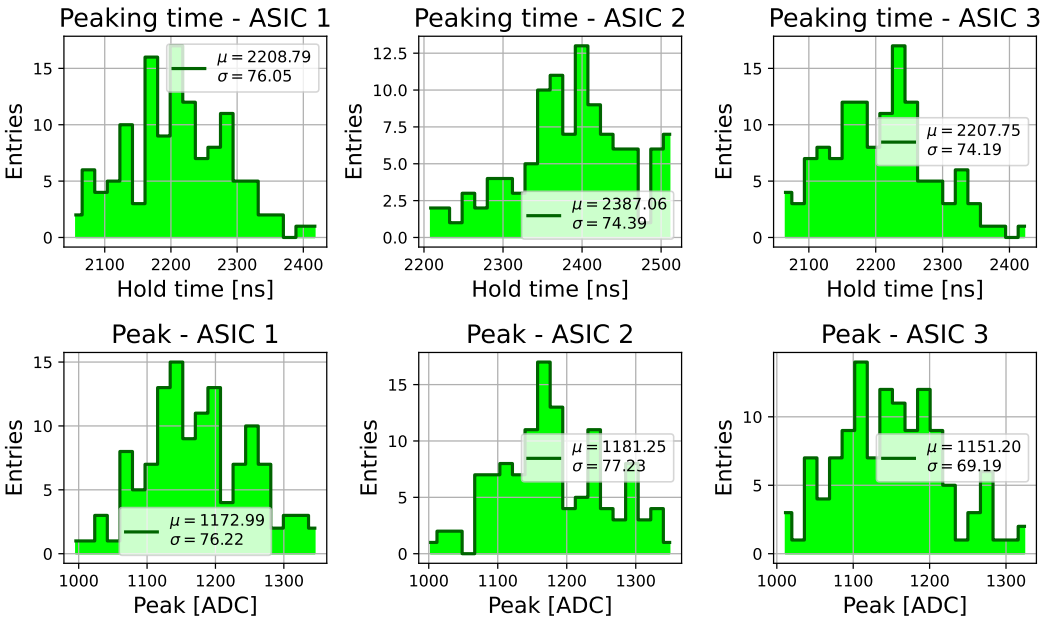

Figure 4.10: Histograms of the peaking times and peak values for each VA2TA ASIC, where the channels, where the fit has not converged optimally, have been excluded. The mean value and the standard deviation are also reported.

be seen that with a calibration signal larger than 20 mV the ASICs begin to saturate.

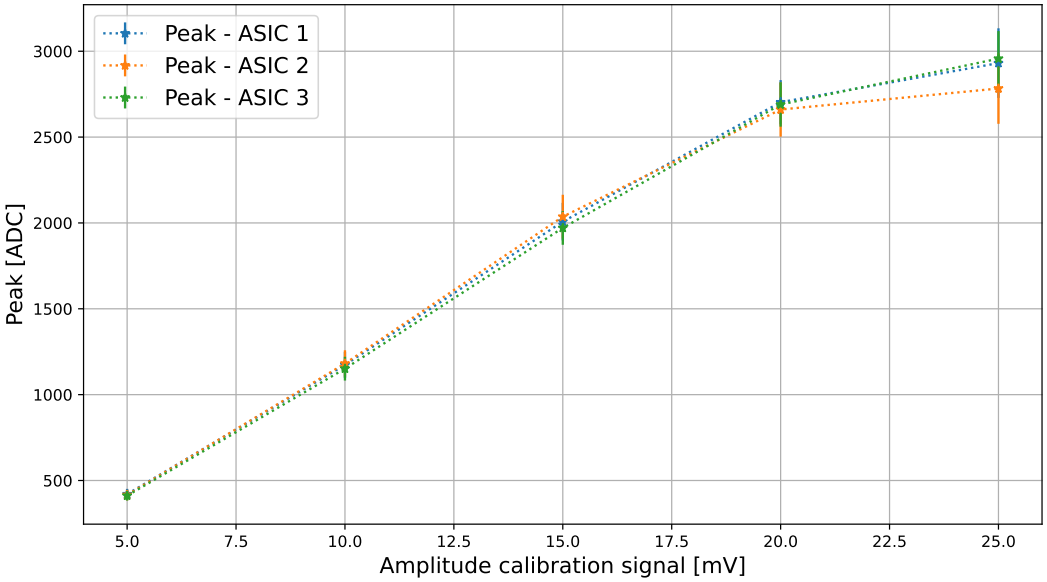

Figure 4.11: Mean pulse height for each VA2TA ASIC as a function of the amplitude of the calibration signal.

4.1.3 Estimation of the Saturation in Terms of MIPs

As a conclusion of the section for the laboratory characterization, it is possible to give an estimation of the saturation in terms of energy deposit by MIPs. A ^{90}Sr radioactive source, which is a β^- emitter, was used as electron source to provide physical signals in the silicon detectors.

Figure 4.12 presents the distribution of the pulse height of the strip which has registered the largest value for each event for the VA1TA beam telescope. Each distribution has been fitted in the region denoted with the grey vertical lines with a Landau distribution, which describes the energy deposit in a thin absorber; the mean and most probable values are reported on the figure.
The first plot represents the case in which the silicon module under test was the first to be crossed by the electrons emitted by the source. The second plot refer to the situation where the ^{90}Sr source was placed on the other side of the telescope, and the electrons must cross the first silicon side before reaching the one under test: the electrons, having lost part of their energy in the first silicon tile, deposit a larger amount of energy in the silicon under test since they are slower. Finally, the last plot refers to an acquisition with cosmic rays, which behave as MIPs. By comparing the first and the third plot, it is

possible to see that the electrons emitted by the ^{90}Sr source placed directly on the silicon side to test are a reasonable approximation of a MIP.

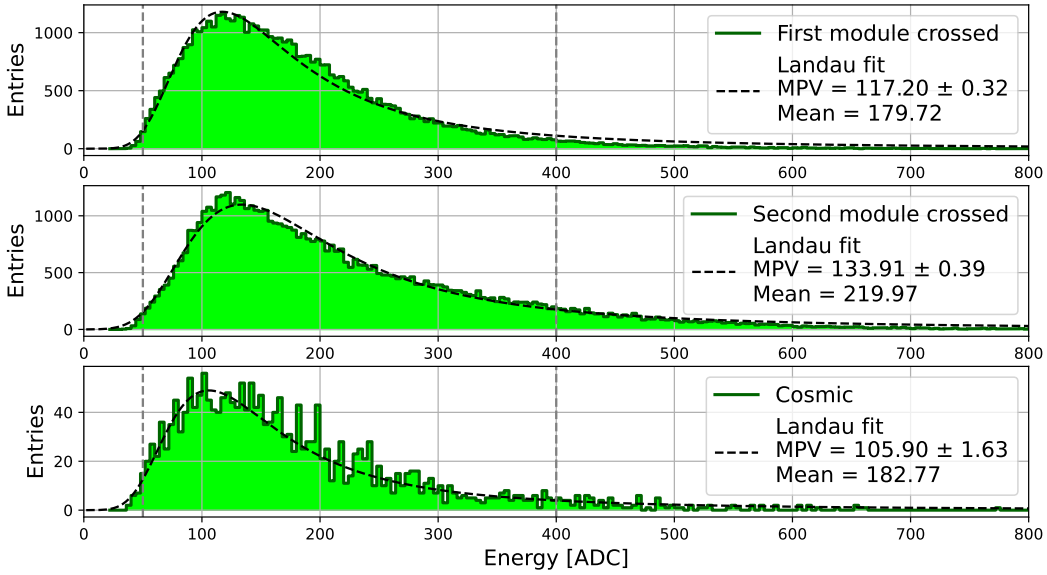

Figure 4.12: Distribution of the pulse height of the strip which has registered the largest value for each event for the VA1TA ASIC. The distribution has been fitted in the region denoted with the grey vertical lines with a Landau distribution, which describes the energy deposit in a thin absorber. The mean and most probable values are also reported. The first plot refers to the case where the electrons emitted by the ^{90}Sr source crossed directly the silicon module under test; in the second plot the radioactive source was placed on the other side of the beam telescope, and the electrons must cross the other silicon side before reaching the one under test. The last plot refers to an acquisition with cosmic rays.

By using the values obtained with the cosmic run, it is possible to give an estimation of the saturation in terms of MIPs. Considering figure 4.6, it is possible to see that the ASICs behave in a linear way up to a peak value of about 1400 ADC. This means that the ASIC starts saturating at about 8 to 13 MIPs depending on whether the mean or the most probable value extracted from the fit with the Landau distribution is considered, which is compatible with the 10 MIPs value reported in table 3.3.

The same estimation may be provided also for the VA2TA beam telescope. In this case, only the ^{90}Sr source was used. Figure 4.13 presents the distribution of the pulse height of the strip which has registered the largest value for each event. The distribution has again been fitted with a Landau distribution.

Considering figure 4.11, it is possible to see that the linearity is preserved up to about 2500 ADC, that is, the ASIC saturates at about 10 to 15 MIPs depending on whether the mean or the most probable value extracted from the fit with the Landau distribution is considered. The obtained value is larger compared to the one reported in table 3.2 (4 MIPs). The reason may be related to a different gain of the amplifiers which is set on the HDI.

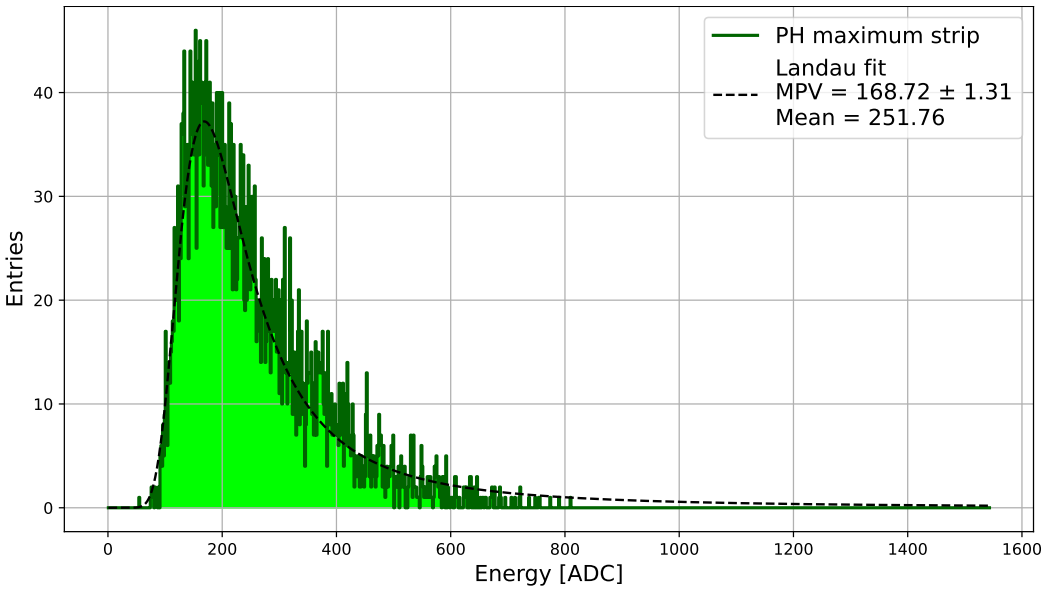

Figure 4.13: Distribution of the pulse height of the strip which has registered the largest value for each event for the VA2TA ASIC. The distribution has been fitted with a Landau distribution, which describes the energy deposit in a thin absorber. The mean and most probable values are also reported.

4.1.4 The Hold Scan

Figure 4.14 presents the scan on the hold time, namely the time at which the analog signal of the silicon strips is sampled, using the ^{90}Sr radioactive source for the VA1TA (diamonds) and VA2TA (stars) beam telescopes to find the optimal value. Two quantities have been studied to determine the best values: the SNR (dashed line) and the pull (dotted line), which is defined as the ratio between the PH of the channel with the maximum signal and its corresponding noise rms.

Both the SNR and the pull provided the same hold value, which resulted to be 400 ns for the VA1TA and 600 ns for the VA2TA. However, the distributions are quite flat around the maximum and therefore the exact value is not so

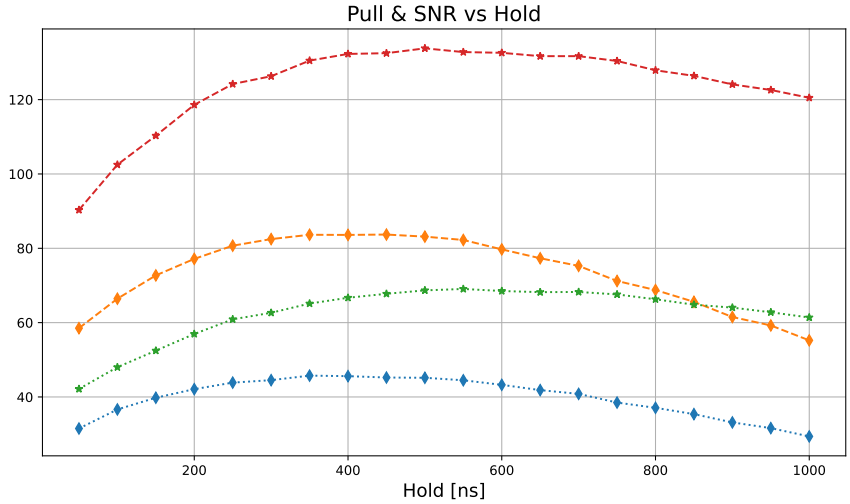

Figure 4.14: Scan on the hold value to find the optimal value for the VA1TA (diamonds) and VA2TA (stars) beam telescopes. Two quantities have been considered: the SNR (dashed line) and the pull (dotted line).

crucial due to the long shaping time of the slow shapers of the ASICs, which is of the order of one µs.

Furthermore, the hold value depends on whether the trigger signal is self generated by the silicon detectors or produced by another detector. Providing the hold signal at the correct time is fundamental to sample the shaper output of the ASIC at the peak of the signal itself, and thus to maximize the SNR.

Figure 4.15 presents the two situations: on the left, the trigger signal (red) is produced when the signal of the scintillator (green) crosses a threshold (orange). Detectors such as scintillators are usually fast, and the peak of the slow shaper of the ASIC (pink) arrives after a long time. On the other hand, on the right, the trigger is produced when the output of the fast shaper of the ASIC crosses a threshold, and the trigger is generated closer to the maximum of the output of the slow shaper.

Figure 4.16a presents an example of the pull distribution for the x sides of the three beam telescopes used for the GALORE beamtest, respectively the VA2TA telescope, a VA1TA telescope and a VA2 one. During the beamtest the trigger was generated only by the x sides, as the channelling deflection is in the xz plane. The first and the last telescopes feature a floating strip on the x side (which is the junction side), and thus a double peak structure can be observed. This structure is related to whether the impinging particle crosses a floating (lower peak) or a readout strip.

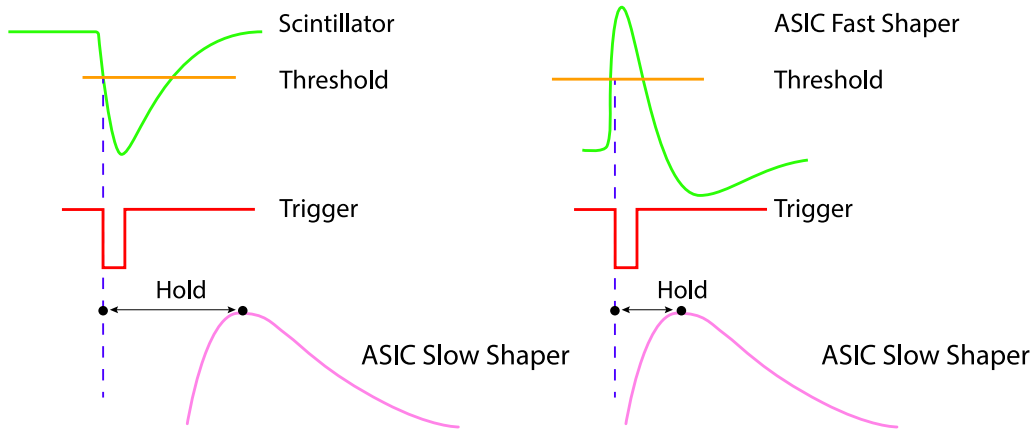

Figure 4.15: (left) The trigger signal (red) is produced when the waveform of the scintillator (green) crosses a threshold (orange). (right) The trigger signal (red) is produced when the output of the fast shaper (green) crosses a threshold (orange). In the first case, the trigger arrives earlier with respect to the peak of the slow shaper, while in the latter case it is closer.

Figure 4.16b presents the SNR distribution for the same beam telescopes: even being different for the three telescopes, the SNR is large enough to set a threshold and operate the detectors in zero suppression mode.

Finally, figure 4.16c presents the distribution of the eta parameter, which is a quantity that describes the sharing of the charge between nearby strips. The eta distribution is defined for single cluster events considering the strip with the maximum signal ($\mathrm{PH_{max}}$) and the strip with the largest signal between the two neighbour ones:

$$\eta_{\mathrm{right}} = \frac{-\mathrm{PH_{max}} + \mathrm{PH_{right}}}{\mathrm{PH_{max}} + \mathrm{PH_{right}}} \tag{4.2a}$$

$$\eta_{\mathrm{left}} = \frac{\mathrm{PH_{max}} - \mathrm{PH_{left}}}{\mathrm{PH_{max}} + \mathrm{PH_{left}}} \tag{4.2b}$$

η_{right} or η_{left} are used depending on whether the pulse height with the largest signal corresponds to the strip on the right of the one with the maximum or the strip on its left.

The two peaks at the edges of the distribution describe the clusters where there is the maximum charge asymmetry between the strip with the maximum signal and its neighbour. This means that the energy has been deposited in one readout strip. In the first and third plots, there is also a peak in the middle, which corresponds to the case of a particle crossing a floating strip so that the charge is collected equally by the two nearby readout ones.

The symmetry of the eta distribution indicates that there is no bias in the readout of the multiplexed analog values.

4.2 Beamtest characterization

After proving to work in a laboratory, the system needs to be tested and validated on a beamline before being used for the data taking for the crystal-based positron source and for the GALORE experiment. This test has been performed at the Frascati BTF which is able to delivery a pure electron beam with a tunable intensity.

The beam telescopes with a self triggering capability were installed in April 2023 to experimentally test the possibility to select a small portion of the incoming beam, which is fundamental for the beamtests described in this thesis. Figure 4.17 presents a photo of the experimental setup, where the beam telescopes and the readout electronics can be seen.

After aligning the beam telescopes with the beam, the first step consisted in choosing the correct hold time. Figure 4.18 presents the results of the hold scan: figure 4.18a shows the mean value of the pull distribution as a function of the hold time, while figure 4.18b the mean value of the pulse height distribution of the strip with the maximum signal in each event. Both plots provided a value of 600 ns as the optimum value for all the four silicon modules.

The whole beam of the BTF, which was presented in figure 2.17, was progressively sliced in the y direction by triggering on the AND of a subset of the two detectors strips around the maximum. Table 4.1 presents the angular divergence in the yz plane as a result of the selection of a small portion of the beam: the divergence decreases reducing the triggering strips interval. In the last configuration (figure 2.18) which is only 500 µm wide (10 strips) on both planes, the angular divergence dropped of a factor three with respect to the one of the whole beam.

Figure 4.19 presents the beam profiles for the external trigger (dotted black lines), and for the smallest and largest slice of the beam: the 120-190 AND 130-190 trigger interval (orange) and the 135-145 AND 150-170 (green) one. Triggering only in the y direction resulted in a reduction of the y profile, while the x one is unchanged.

Figure 4.20 presents the pull (a), SNR (b) and eta (c) distributions for the y sides of the beam telescopes used during the beamtest at the BTF. The VA1TA telescopes do not feature any floating strip, therefore the pull distribution presents a single peak and the eta distribution does not present the peak in the middle.

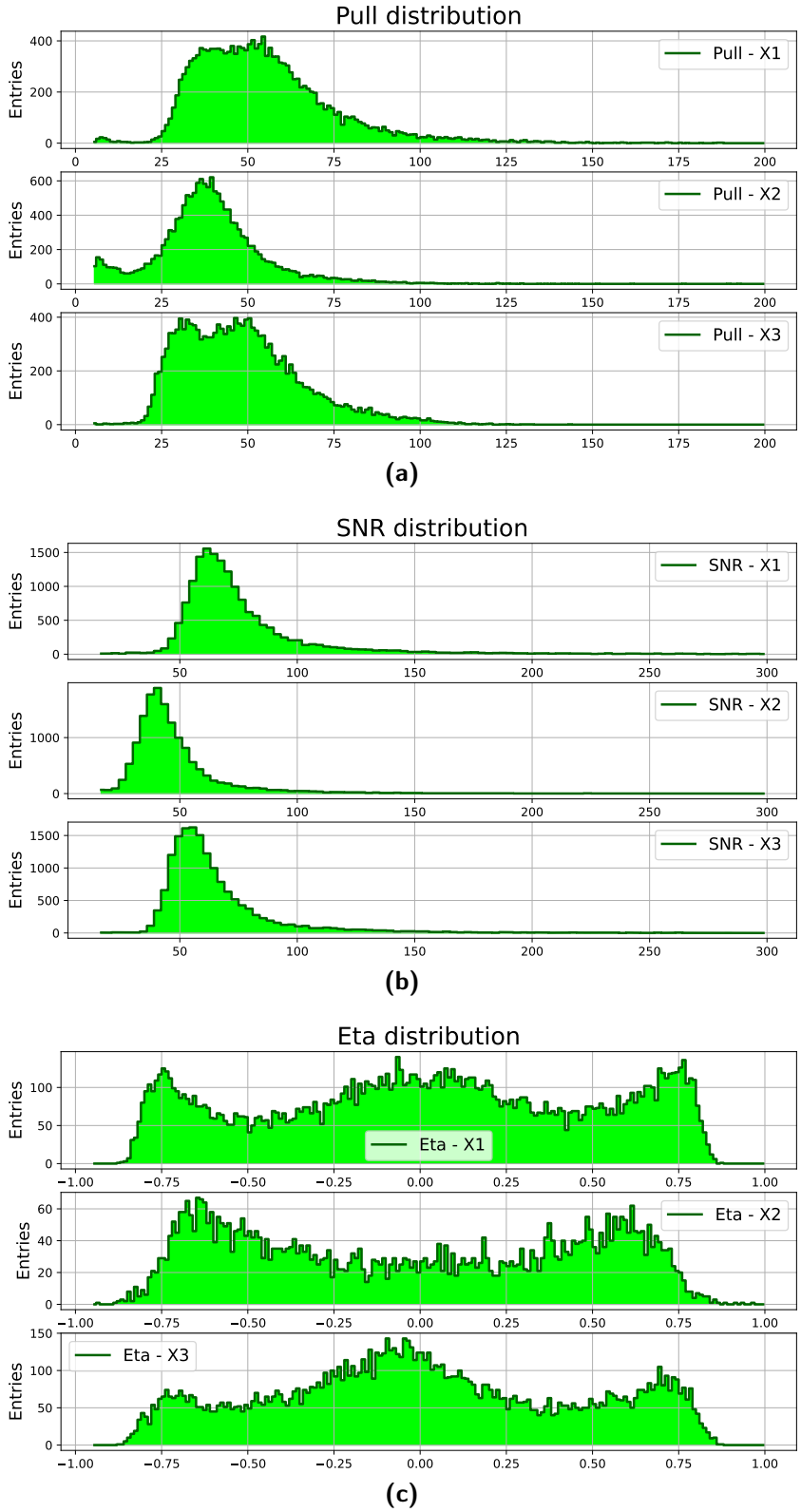

Figure 4.16: (a) Pull, (b) SNR and (c) eta distributions for the x sides of the beam telescopes used during the GALORE beamtest. The first plot of each group refers to the VA2TA telescope, the second to the VA1TA telescope and the third to the VA2 telescope.

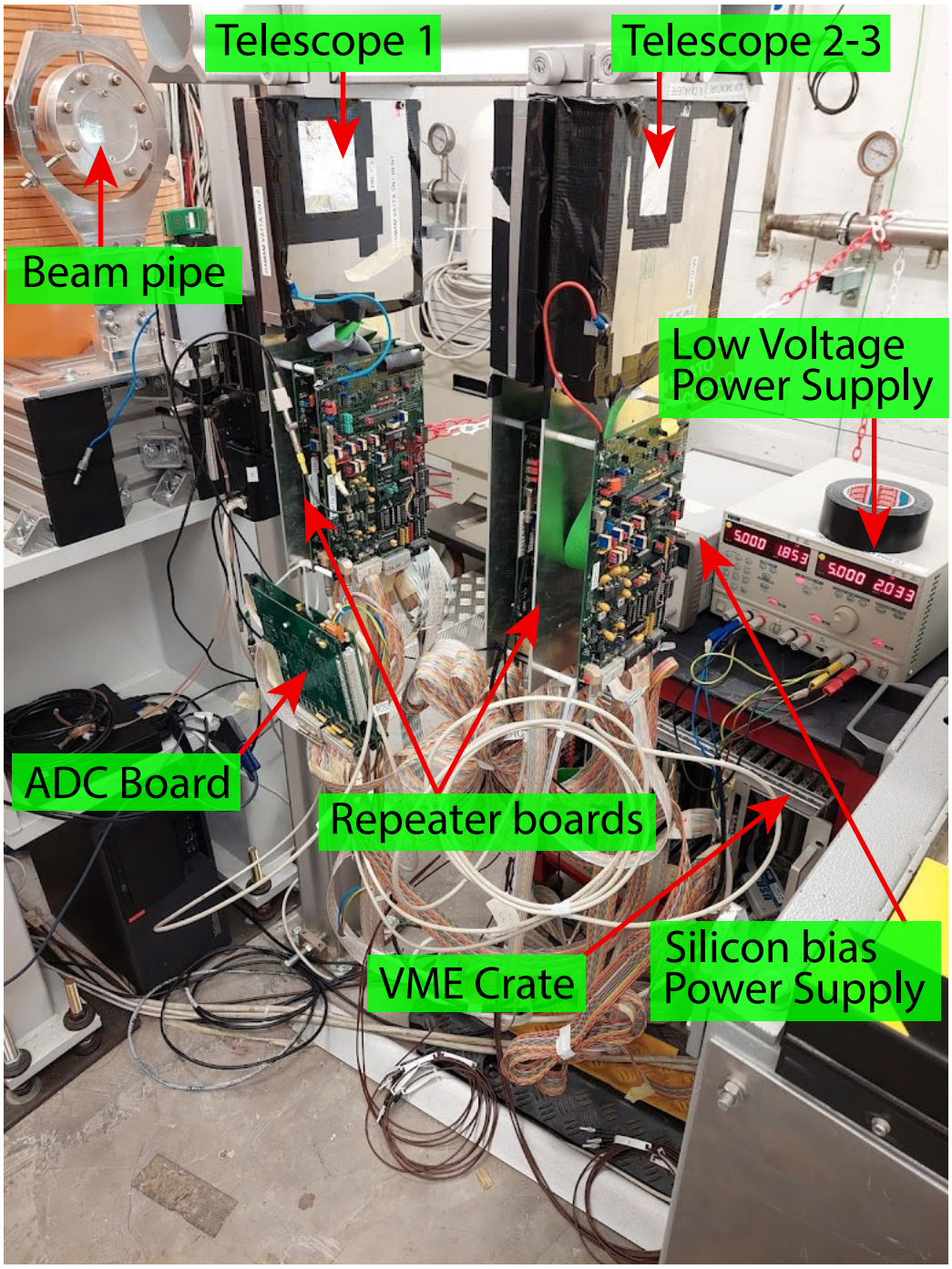

Figure 4.17: Photo of the experimental setup of the BTF beamtest in April 2023.

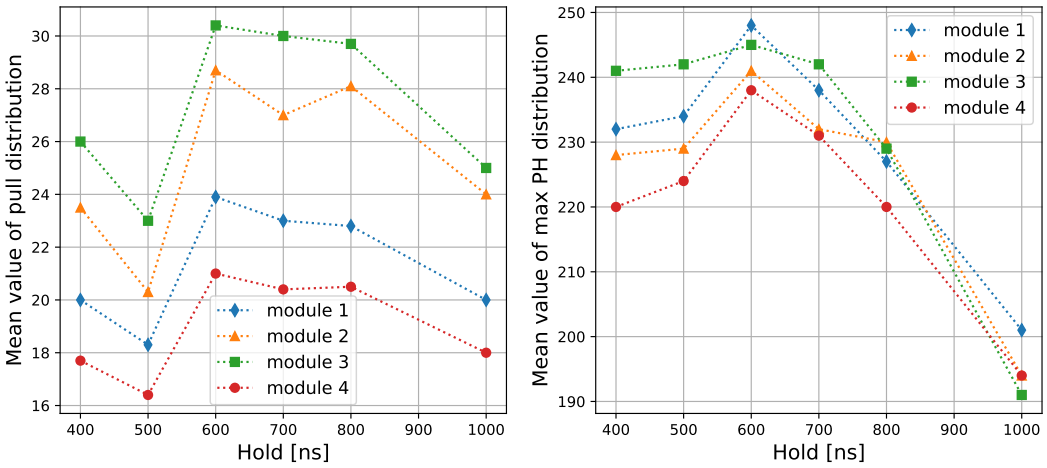

Figure 4.18: Hold scan during the beamtest at the Frascati BTF. (left) Mean value of the pull distribution as a function of the hold time. (right) Mean value of the pulse height distribution for the strip with the maximum signal in each event. Both plots provided a value of 600 ns as the optimum value for all the four silicon modules.

Table 4.1: Table of the strip interval and the corresponding y angular divergence. The trigger condition was the AND of the two y sides.

Region sili 1 (strips)	Region sili 2 (strips)	y angular divergence (mrad)
Ext trig	Ext trig	3.02 ± 0.02
120 - 190	130 - 190	2.39 ± 0.07
120 - 160	130 - 190	2.46 ± 0.14
120 - 160	140 - 180	2.10 ± 0.12
120 - 160	150 - 170	2.36 ± 0.32
130 - 150	150 - 170	1.87 ± 0.22
120 - 160	155 - 165	1.67 ± 0.15
135 - 145	150 - 170	0.93 ± 0.01

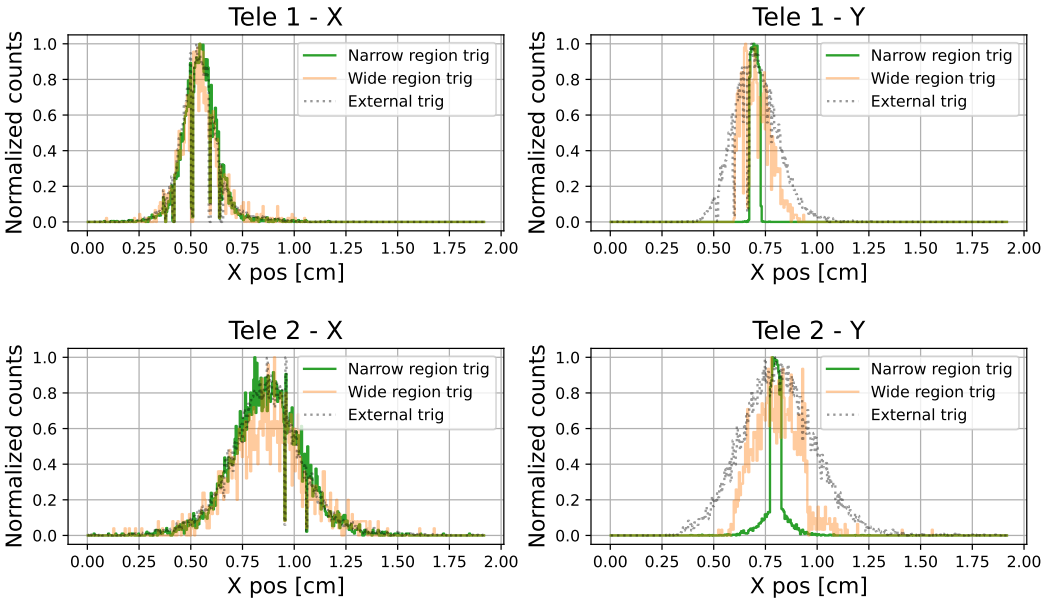

Figure 4.19: Beam profiles for the external trigger (dotted black lines), and for the smallest and largest beam slices during the beamtest at the Frascati BTF: the 120-190 AND 130-190 trigger interval (orange) and the 135-145 AND 150-170 (green) one. Triggering only in the y direction resulted in a reduction of the y profile, while the x one is unchanged.

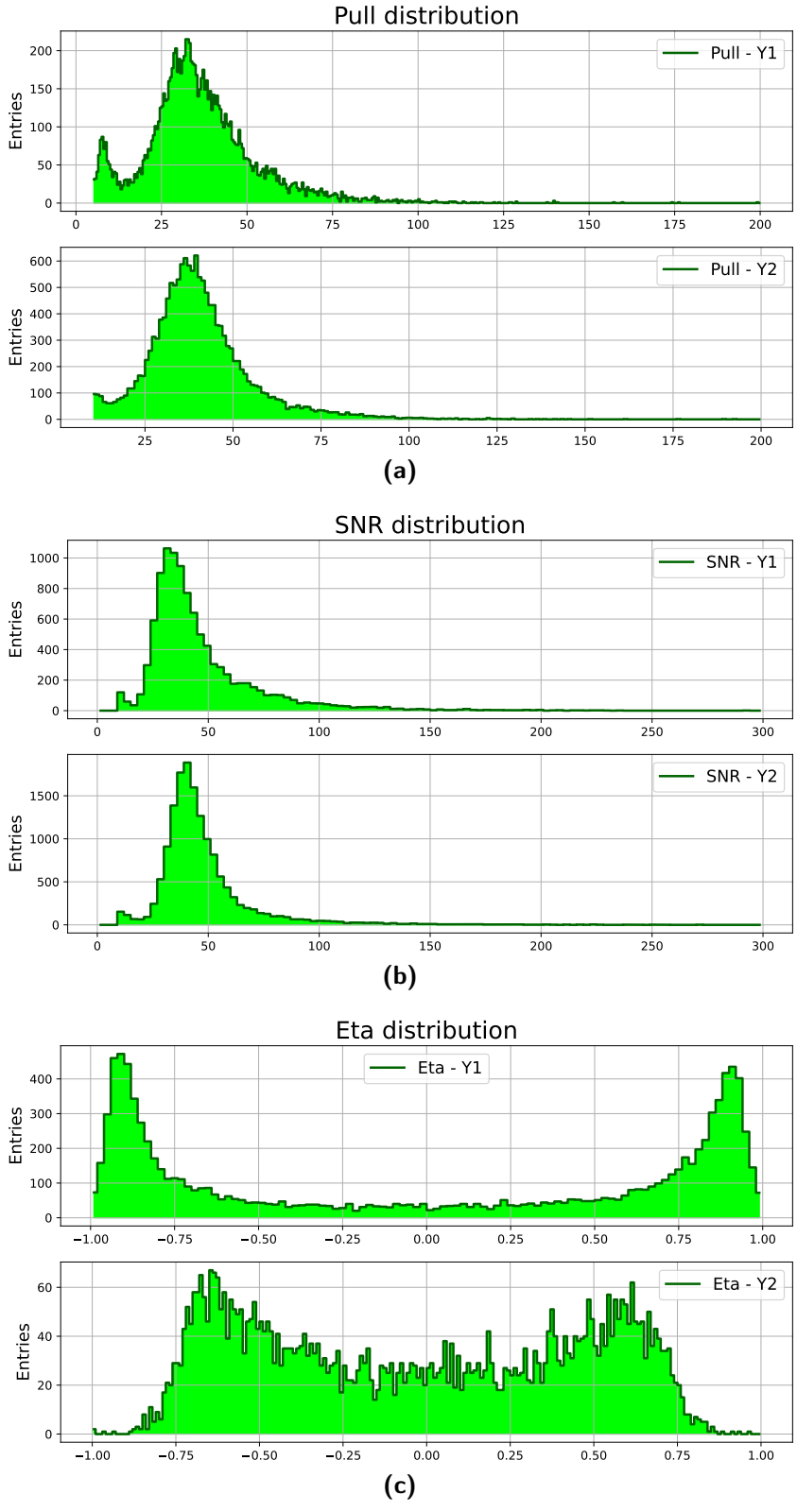

Figure 4.20: (a) Pull, (b) SNR and (c) eta distributions for the y sides of the beam telescopes used during beamtest at the BTF for the VA1TA telescopes.

In channelling experiments, crystals are usually installed so that the deflection happens in the xz plane, therefore the tracking detectors are mounted with the highest resolution direction along x. However, in the BTF beamtest the detectors were installed 90° rotated with respect to the usual configuration: the beam was sliced along the y direction to test the exact configuration that is required for the GALORE experiment.

Chapter 5

Beamtests Data Analysis

The first chapter of this thesis was dedicated to the description of the Physics of crystals and, in particular to two possible applications of bent crystals in particle Physics. The characterization of a crystal radiator for a hybrid positron source and the new crystal design of the GALORE project required a strict control over the beam size and the angular divergence of the beam itself. To meet the experimental requirements, an upgrade of the readout electronics of the silicon microstrip tracking detectors was implemented, to allow them to self generate a trigger signal once a particle impinges on a subset of strips: in this way, only a portion of the whole beam can be selected, allowing the rejection of events due to particles not interacting with the crystal and increasing the acquisition rate, which is fundamental to collect a statistics large enough.

This chapter presents some experimental results based on the collected data. The goal of the following sections is to focus on the features of the system that allowed the data to be acquired rather than on the physical results themselves.

5.1 The GALORE Beamtest

The GALORE beamtest was performed at CERN in June 2023 in the PPE128 experimental area, on the H8 SPS extracted beamline. For the whole beamtest a positive pion beam with a momentum of 180 GeV/c was used; on the other hand, the configuration of the optics of the beamline, which determined the beam size, angular divergence and intensity, was changed several times.

5.1.1 The Experimental Setup

Being a test of the channelling performance, the experimental setup belongs to the class presented in figure 2.2. However, given that the GALORE crystal is only 4.1 mm long in the z direction, one downstream tracker was enough, and the second point for the outgoing track reconstruction was provided by the position of the particle on the crystal itself. Figure 5.1 presents a sketch of the experimental layout of the GALORE beamtest. A 1 cm thick plastic scintillator was added at the beginning of the beamline to provide an *external* trigger signal, that is, not produced by the silicon detectors themselves. An external signal is necessary in the preliminary phase to ensure that the self generated trigger signal works properly. The crystal under test was installed on a multi stage high precision goniometer. The PPE128 experimental area does not offer a remotely controlled moving platform, therefore the goniometer was also equipped with a vertical stage.

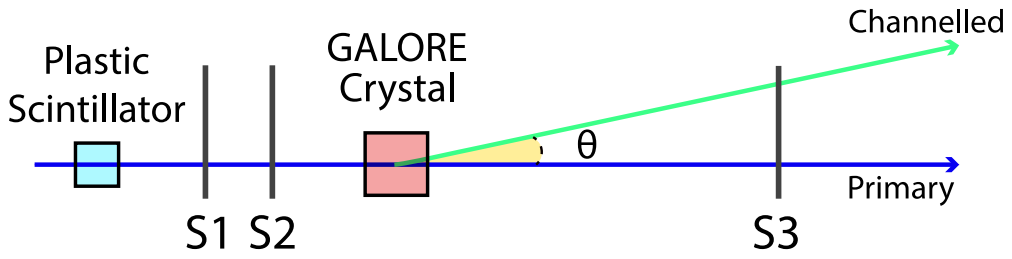

Figure 5.1: Sketch of the experimental setup for the GALORE beamtest in the PPE128 experimental area. A 1 cm thick plastic scintillator was added at the beginning of the beamline to provide an *external* trigger signal; the crystal under test was installed on a multi stage high precision goniometer.

The first two beam telescopes featured the VA1TA and VA2TA readout ASICs and were therefore capable of self producing the trigger to be able to select only a small portion of the incoming beam. The downstream detector, on the other hand, needed to be installed in such a way that both the primary and the channelled beam crossed its sensitive area.

An example of the beam profile acquired with an external trigger and with a selection in x has been presented in figures 2.13 and 2.14. However the beam configuration was changed during the beamtest. The trigger signal was produced by the *AND of the* x sides of the first two beam telescopes, but the chosen strip interval was modified from time to time.

Figure 5.2 presents two x beam profiles as seen by the first two telescopes for two different beam configurations (orange), one per each row, and the portion of the beam selected by self triggering on the first two telescopes (green). For the first situation (first row), triggering by selecting the 30 strip wide x interval represented in figure 5.2 resulted in selecting 20 - 25 % of the whole beam, that is, in the possibility to acquire statistics 4 to 5 times faster. For the second beam configuration the beam profile was *flattened* along the x direction to reduce the beam divergence: after a precise alignment of the crystal, it was possible to trigger on a 13 strip wide region, which allowed to select only 3 - 5 % of the beam, thus giving the possibility to acquire statistics 20 to 30 times faster.

The last beam configuration was kept for more than half of the week. Considering that the crystal is 500 µm wide in the x direction, but the micro trench is only 150 µm, as it may be seen in the sketch of the GALORE crystal with the relevant dimensions in the xz plane (figure 5.3), it would have been impossible to collect a statistics large enough with the whole beam. It is worth to mention that the particles selected by triggering on such strip interval are not guaranteed to produce an event of physical interest: no selection was applied in the y direction and the selected region was wider than the crystal x dimension and therefore than the micro trench. However, particles that are rejected by the trigger are for sure of no physical interest, and considering their percentage it should be clear how powerful such test system is.

Figure 5.4 presents the angular divergence of the beam for the same runs of figure 5.2, considering the whole beam (orange) and the portion of the beam selected by triggering on the AND of the x sides of the silicon telescopes (green). The values of the beam divergence, quoted as the standard deviation of the distributions, are reported in the legend of the figure. It is worth to note the horizontal divergence of the second beam configuration: by triggering on the beam telescopes, it was possible to reduce the divergence itself from 86 µrad to 32.2 µrad. For the first beam configuration, triggering on the beam telescopes allowed to reach an angular divergence of 25.6 µrad, even if the gain with respect to the whole beam is smaller. Finally, triggering only on the x sides of the telescopes did not cause a significant modification to the y angular divergence of the beam.

The alignment of a non scintillating crystal with respect to the incoming beam is a difficult task, primarily due to the fact that the crystal cannot

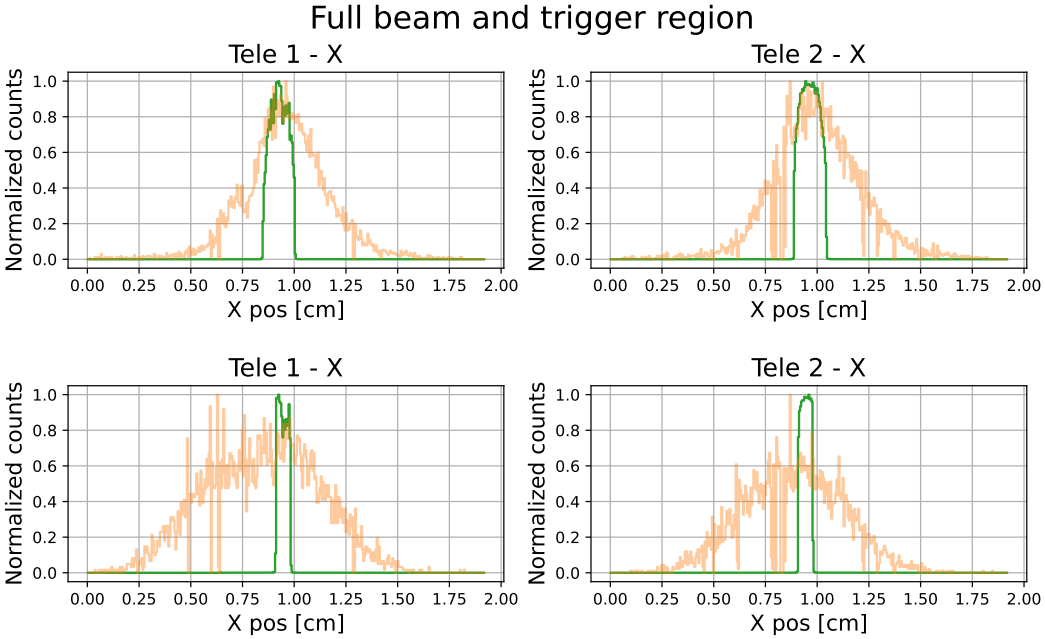

Figure 5.2: x beam profiles as seen by the first two telescopes (orange) and portion of the beam selected by self triggering on the AND of the x sides (green) of the first two telescopes, for two different beam configurations (one in each row) during the GALORE beamtest. The strip interval chosen for the self trigger generation is the logical AND of the two detectors. In the first configuration a 30 strip wide interval allowed to select 20 - 25 % of the whole beam. On the other hand, in the last case, a 13 strip wide interval allowed to select 3 - 5 % of the whole beam.

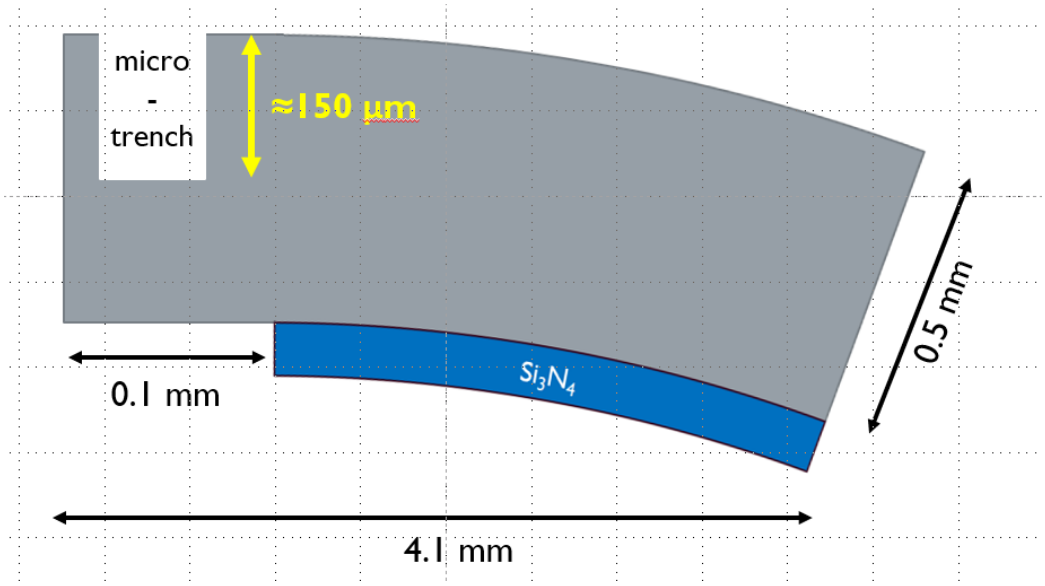

Figure 5.3: Sketch of the GALORE silicon crystal (top view). The crystal is curved along the beam direction z. Image from [84].

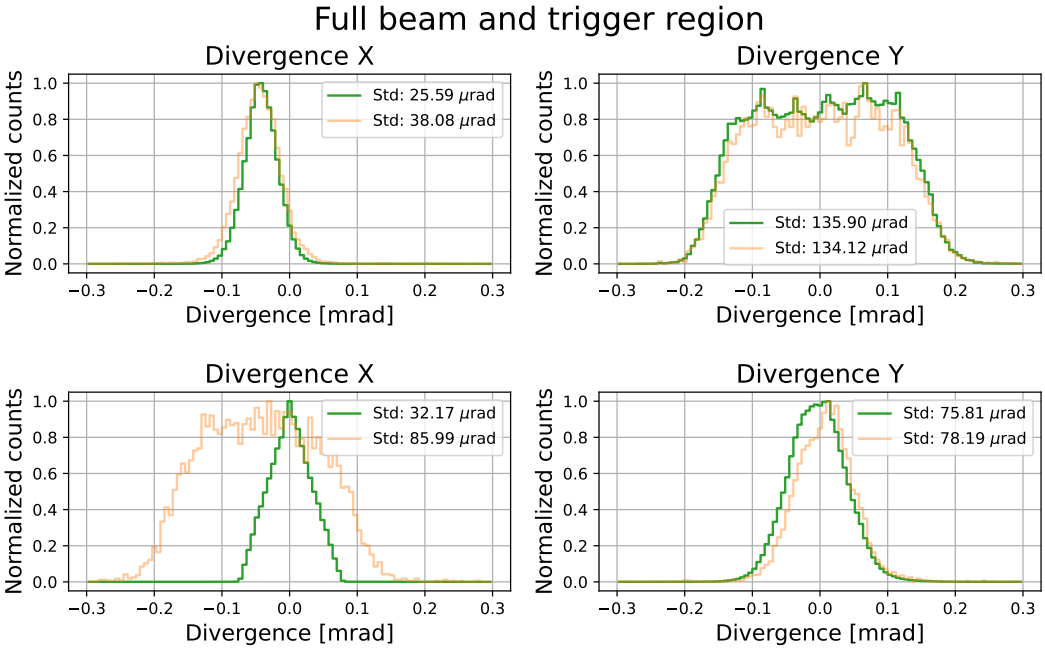

Figure 5.4: Beam angular divergence considering the whole beam (orange) and the portion of the beam selected by triggering on the AND of the x sides of the silicon telescopes (green), for two different beam configurations (one in each row) during the GALORE beamtest.

produce a signal when crossed by particles. Neither the channelling peak may be searched for, since for channelling to happen, a precise alignment of the crystal planes/axes with respect to the beam direction is necessary and for this alignment it is fundamental that the crystal is crossed by the incoming beam.

Considering how the crystal was installed on the goniometer (figure 5.5) in the x direction, at least 2 cm of air gap were present at each side of the crystal. If a *lateral scan* with the linear stage of the goniometer is performed, that is the holder with the crystal is moved across the beam, one expects that when the beam crosses the crystal, particles are scattered by the crystal itself. By filling a 2d histogram of the reconstructed x position on the crystal face for each particle versus the difference $\Delta\theta$ of the outgoing and incoming angles, the position of the crystal should appear as an increase in the rms of the $\Delta\theta$ distribution itself. Recall that only single particle events can be considered in the analysis. In fact, if two or more particles impinge on the crystal at the same time, it is not possible to associate the incoming tracks to the outgoing ones.

For the vertical alignment a similar idea was adopted. However the crystal is fixed to a mechanical holder at both its ends, as it may be seen in figure 5.5. Although the horizontal sections of the "C-shaped" mechanical support scatter the incoming particles, this was not enough to clearly identify the vertical position of the crystal itself. Hence, an aluminum block was added on the goniometer plate, to provide a reference point in the y direction.

Figure 5.6 left presents the 2d histogram of the reconstructed y position on the crystal face for each particle versus the difference $\Delta\theta_x$ of the outgoing and incoming particle angles in the xz plane. The events on the left of the pink line are the ones corresponding to the beam crossing the aluminum block: the resulting scattering is larger than the one in the right region, where the beam crosses either the crystal or the air.

For what concerns the x position, the scatter induced by a several cm thick aluminum block is much larger than the one caused by the crystal. This means that considering all the events, the ones corresponding to a particle crossing the aluminum block would mask the ones of particles crossing the crystal. Thus, to identify the horizontal position of the crystal, it was compulsory to consider only the particles that did not cross the aluminum block itself. The right side of figure 5.6 presents the 2d histogram of the reconstructed x position on the crystal face versus $\Delta\theta_x$ only for the events that do not cross the aluminum block, that is, the events with a reconstructed y position greater than the pink line of the left plot of figure 5.6. Again, the x position of the crystal corresponds to an increase in the $\Delta\theta_x$ distribution.

As a conclusion of this subsection, it is worth to mention that all the

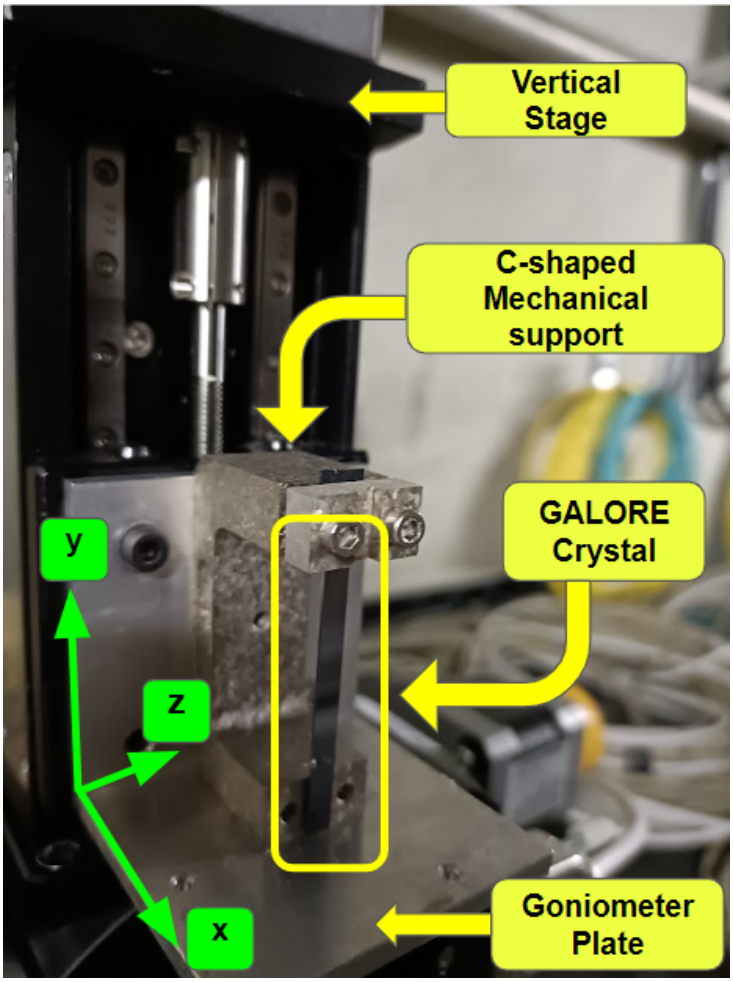

Figure 5.5: GALORE crystal installed on the goniometer in the PPE128 experimental area. The "C-shaped" mechanical support has been indicated: it is possible to see that at least few centimeters of air are present along the x direction, but the ends of the crystal are fixed to the support itself in the y direction. Furthermore, the goniometer plate, where the aluminum block was added, has been indicated.

measurements up to this point were performed with the whole beam, namely triggering on the plastic scintillator. Considering figure 5.6 right, it is clear that collecting data with the whole flat beam would result in rejecting offline 95 - 97 % of the events (figure 5.2). When studying effects like the difference in channelling efficiency in the micro trench and in the rest of the crystal, statistics plays a fundamental role: angular and position cuts have to be applied and this reduces statistics. Thus, it is fundamental to acquire events only in the interesting region.

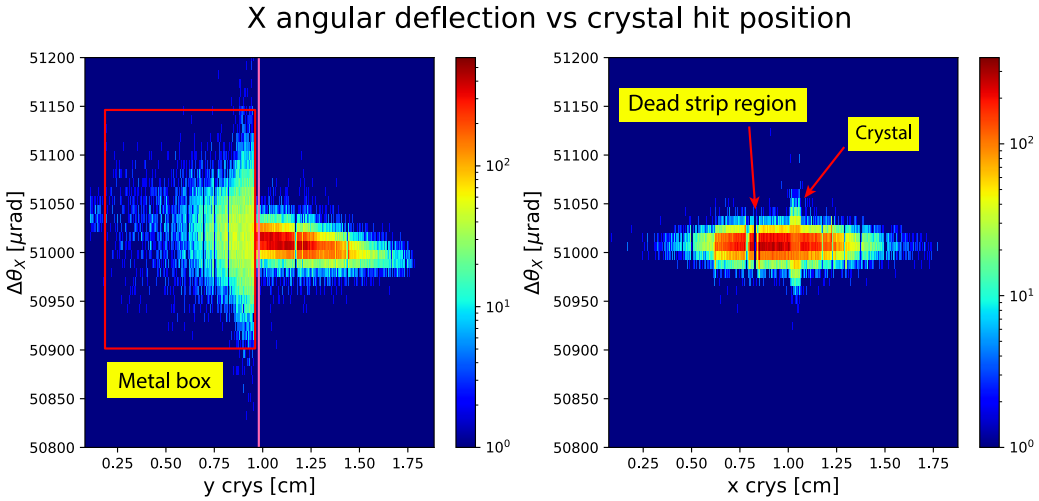

Figure 5.6: 2d histogram of the reconstructed track position on the crystal face versus the difference $\Delta\theta_x$ of the outgoing and incoming particle angles in the xz plane. (left) Reconstructed y position vs $\Delta\theta_x$: the pink line defines the events that cross an aluminum block placed as a reference point (resulting in a large rms in the $\Delta\theta_x$ distribution) from the other events. (right) Reconstructed x position vs $\Delta\theta_x$ only for the events on the right of the pink line, which are the ones that do not cross the aluminum block. The crystal can be clearly identified considering the increase in the rms of the $\Delta\theta_x$ distribution.

5.1.2 The Self Triggering Beam Telescopes

Once the crystal was successfully put on the beam, a fine tuning of the goniometer stages positions was performed. In particular, as it may be seen in figure 5.2, the second beam telescope presents several dead strips around $x = 0.75\,\text{cm}$, which can be seen as a "hole" in figure 5.6 around the same x position. Such strips may correspond to either dead channels or to noisy strips, that are disabled by the DAQ software. The crystal was therefore

positioned in the best region not to have "holes".

Once the crystal was centered on the beam, the trigger could be restricted to a narrow region around the crystal itself, and an angular scan with the rotational and cradle stages of the goniometer has been performed in order to find the correct orientation.

Figure 5.7 presents the 2d histogram of the x deflection as a function of the x position reconstructed on the crystal face. An increase in the rms of the horizontal angular deflection appears for a region 500 µm wide, which corresponds to the crystal x dimension. Provided that the micro trench is 150 µm along the x direction, the 50 µm vertical slice was chosen in the middle of the trench itself, that is between 50 µm and 100 µm from the beginning of the crystal.

In the right part of the plot, where the micro structure is not present, two regions (1) and (2) with a spread in the angular deflection distribution which extends in opposite directions may be seen. Despite the origin being not fully understood, they may be related to some imperfection in the crystal; perhaps the silicon nitride film, which was hot deposited in such a way that the temperature difference induces the stress that bends the crystal, may have diffused inside the crystal itself causing these effects.

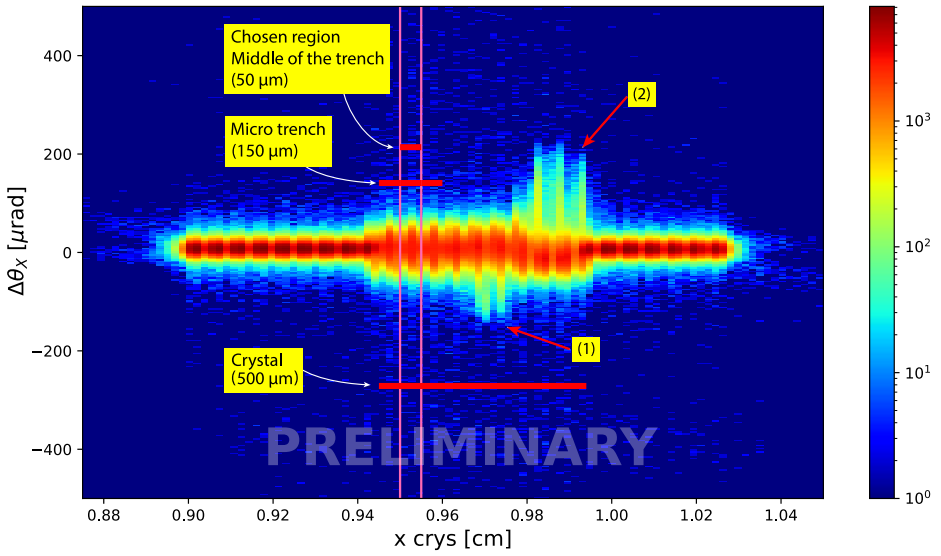

Figure 5.7: 2d histogram of the horizontal deflection as a function of the reconstructed x position on the crystal face. The crystal appears as a 500 µm wide region characterized by an increase in the rms of the horizontal deflection. The pink lines denote a 50 µm wide vertical region in the middle of the micro trench. The effects in regions (1) and (2) are not fully understood.

Figure 5.8 presents the 2d histogram of the horizontal deflection as a function of the incoming angle for the 50 µm vertical slice to select only particles impinging in the middle of the micro trench. The channelling region is indicated by the pink lines: it is centered on the channelling peak and $2\theta_c = 30$ µrad wide. The channelling region itself is followed by the volume reflection, where the deflection is in the opposite direction.

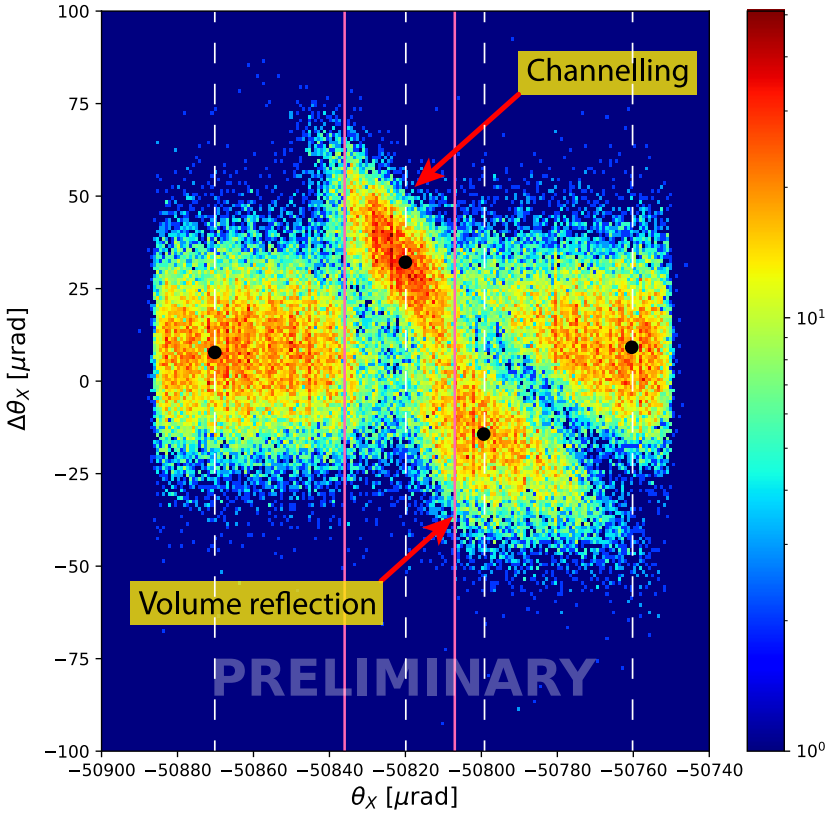

Figure 5.8: 2d histogram of the horizontal deflection as a function of the incoming angle selecting only particles impinging in the middle of the micro trench. The pink lines denote the region where the channelling lies. Immediately after, there is the volume reflection, where the deflection is in the opposite direction. The black dots indicate the center of the 10 µrad regions that have been considered for figure 5.9.

Four 10 µrad regions of incoming x divergence have been chosen, whose centers are indicated with black dots in figure 5.8, corresponding to the channelling, volume reflection and two amorphous lateral regions. Figure 5.9 presents the histograms of the horizontal deflection in the four regions themselves. The two amorphous regions (orange and black) are practically superimposed. The channelling region (red) and the volume reflection one (blue)

result in a deflection in two opposite directions. Furthermore, both regions contain a lower peak due to particles that have not undergone any effect.

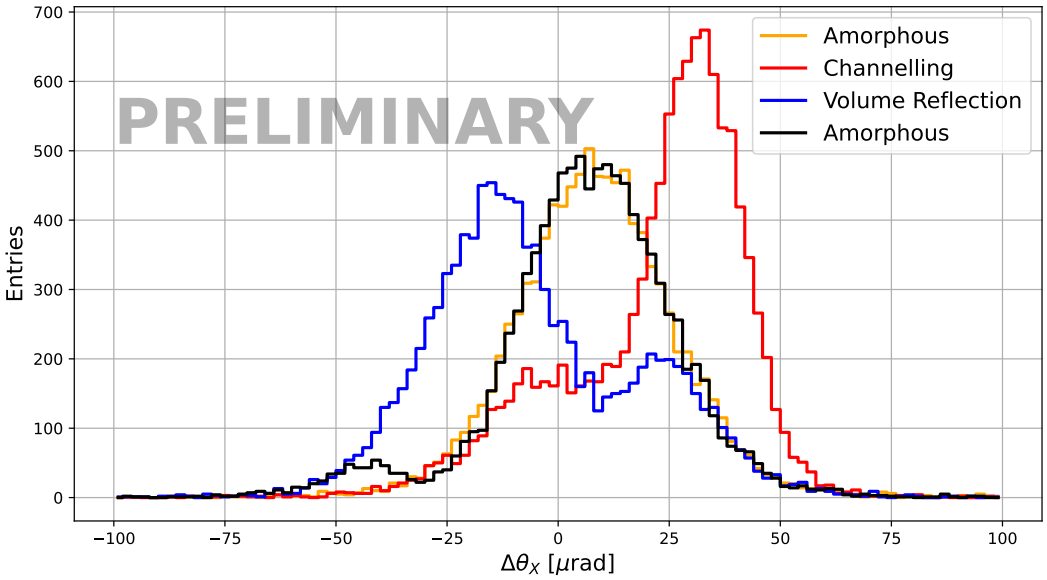

Figure 5.9: Histograms of the horizontal deflection in the 10 µrad regions whose centers are indicated with black dots in figure 5.8. The two amorphous regions (orange and black) are practically superimposed. The channelling region (red) and the volume reflection one (blue) result in a deflection in two opposite directions.

The analysis team is still working on the data analysis for a correct selection of the relevant events upon which the estimation of the channelling performance should be made. For instance, a further selection in the y direction is needed to truly select only the events that cross the micro trench. However, for a preliminary estimation, one may consider only the events that lie between the two pink lines of figure 5.8. Figure 5.10 presents the histogram of the deflection angle for those events. The channelling efficiency may therefore be estimated as the area of the channelling peak, which can be measured with a gaussian fit divided by the area of the whole histogram; the preliminary analysis yields a value around 65 %.

5.2 Positron source beamtests

The beamtests for the characterization of different possible crystal radiators for a hybrid positron source were performed in August 2022 and August 2023 on the T9 experimental area, using a 1 - 6 GeV/c electron beam. For both

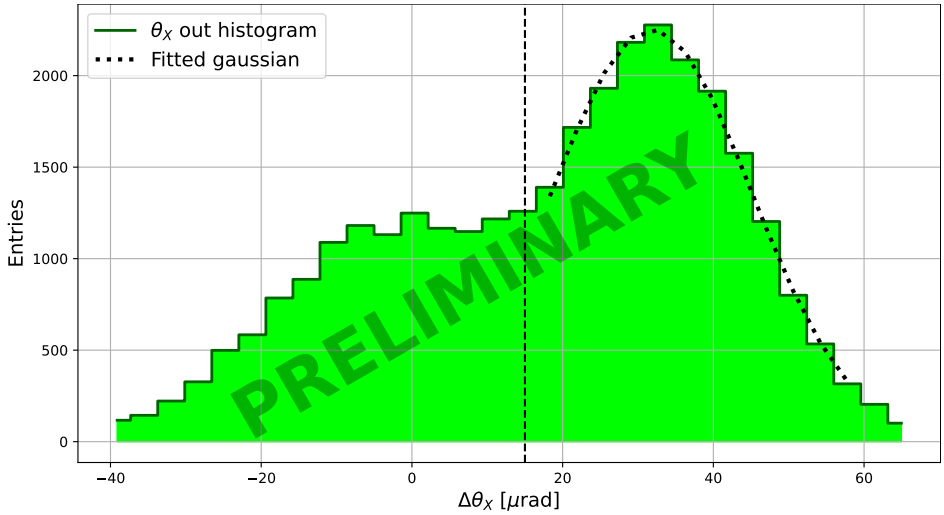

Figure 5.10: Histogram of the horizontal deflection in the channelling range selected in figure 5.8. The fraction of the channelling peak, measured with a gaussian fit may represent an estimation of the channelling efficiency.

beamtests, the beamline was configured with a parallel optics. The reason is that the three crystals were installed in a horizontal line on a plastic support (figure 5.11) and in this way it was possible to acquire particles crossing any of the three crystals.

5.2.1 The Experimental Setup

The tested crystals during the 2023 beamtest (already introduced in section 1.5) are the following:

- a 2.5 mm thick $\langle 111 \rangle$ tungsten crystal
- a 1.5 mm thick $\langle 111 \rangle$ tungsten crystal
- a 1 mm thick $\langle 110 \rangle$ iridium crystal

An intense positron source is a crucial element for future e^+e^- colliders. As presented in section 1.5, the main goal of the e+BOOST project is to demonstrate the feasibility of a hybrid positron source, using oriented crystals as photon radiators and then an amorphous high Z target where the photons themselves can convert into electron/positron pairs.

The test of the increase in the radiation production by an oriented crystal with respect to the non oriented situation requires an experimental setup such as the one presented in figure 2.1; figure 5.12 presents a photo of the

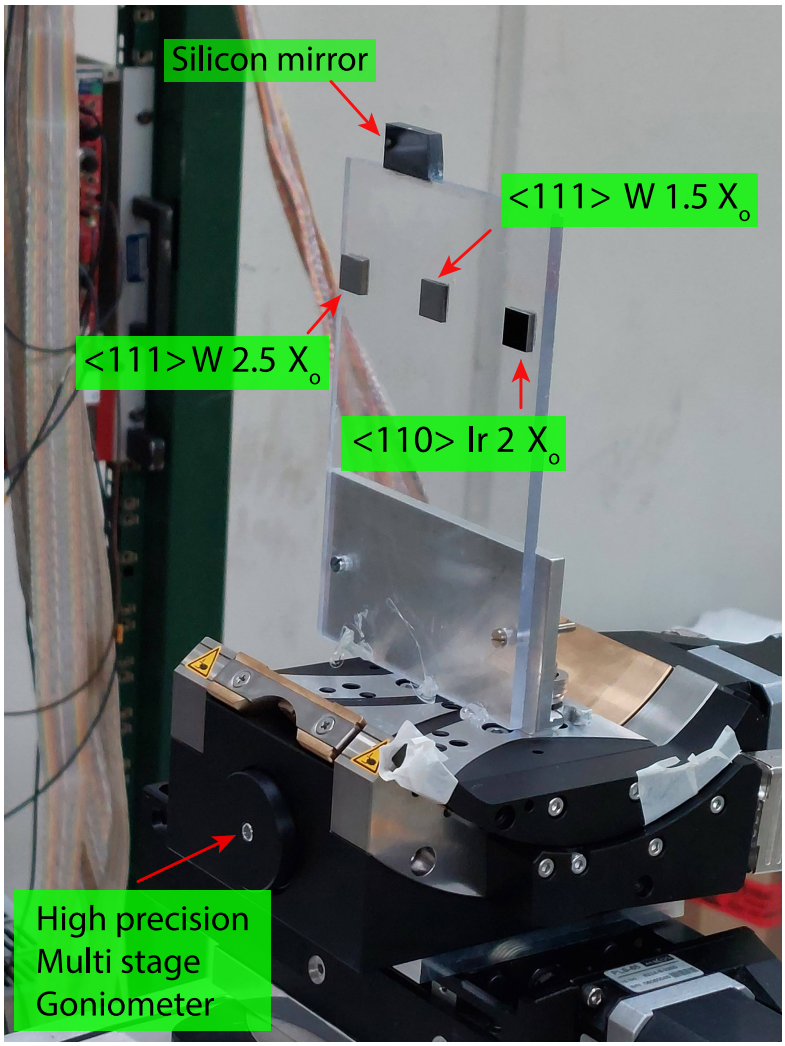

Figure 5.11: Photo of the crystal radiators for a hybrid positron source tested in August 2023 on the T9 beamline. A silicon mirror is added as a reference point for the pre-alignment.

experimental setup itself, where the key elements have been indicated. In particular:

- A pair of beam chambers tracks the incoming particles.
- The crystals under test were installed on a high precision multi stage goniometer for a precise orientation of the crystal planes/axes with respect to the beam direction.
- The goniometer, in turn, was installed on a remotely controlled moving platform (XSCA table) to position the crystal out of the beam; this can be useful for instance during the calibration phase of the calorimeter, when the incoming particles are required to be absorbed by the calorimeter without any obstacle.
- A dipole magnet sweeps away all the charged particles from the beam direction, leaving only photons.
- The APC composed of a thin copper layer sandwiched between a couple of plastic scintillators, provides an information that, coupled with the simulation, allows to compute the photon multiplicity, useful both to find the correct axial orientation and to measure the produced radiation.
- A lead glass electromagnetic calorimeter is placed at the end of the beamline to measure the deposited energy by fully absorbing the beam. The calorimeter is placed on a remotely controlled moving platform (Desy table) for the correct alignment on the beam.

5.2.2 The Self Triggering Beam Chambers

As for the GALORE beamtest, the first step was to put the crystals on the beamline. However in this case the task was somewhat easier, since a direct effect of the interaction between the crystal and the electrons of the beam, that is, the photon production, can be directly measured, for instance using the APC and the calorimeter.

Figure 5.13 presents the 2d histogram of the reconstructed tracks on the crystals plane weighted on the calorimeter pulse height. In fact, if the sweeping magnet is turned on, the calorimeter will only measure the energy deposited by photons, which are mainly produced by electrons inside the crystal radiator via bremsstrahlung. The plot on the left refers to a random orientation while on the right the same plot for the axial orientation of the crystal in the middle ($\langle 111 \rangle$ tungsten) is shown. In both plots, three squares

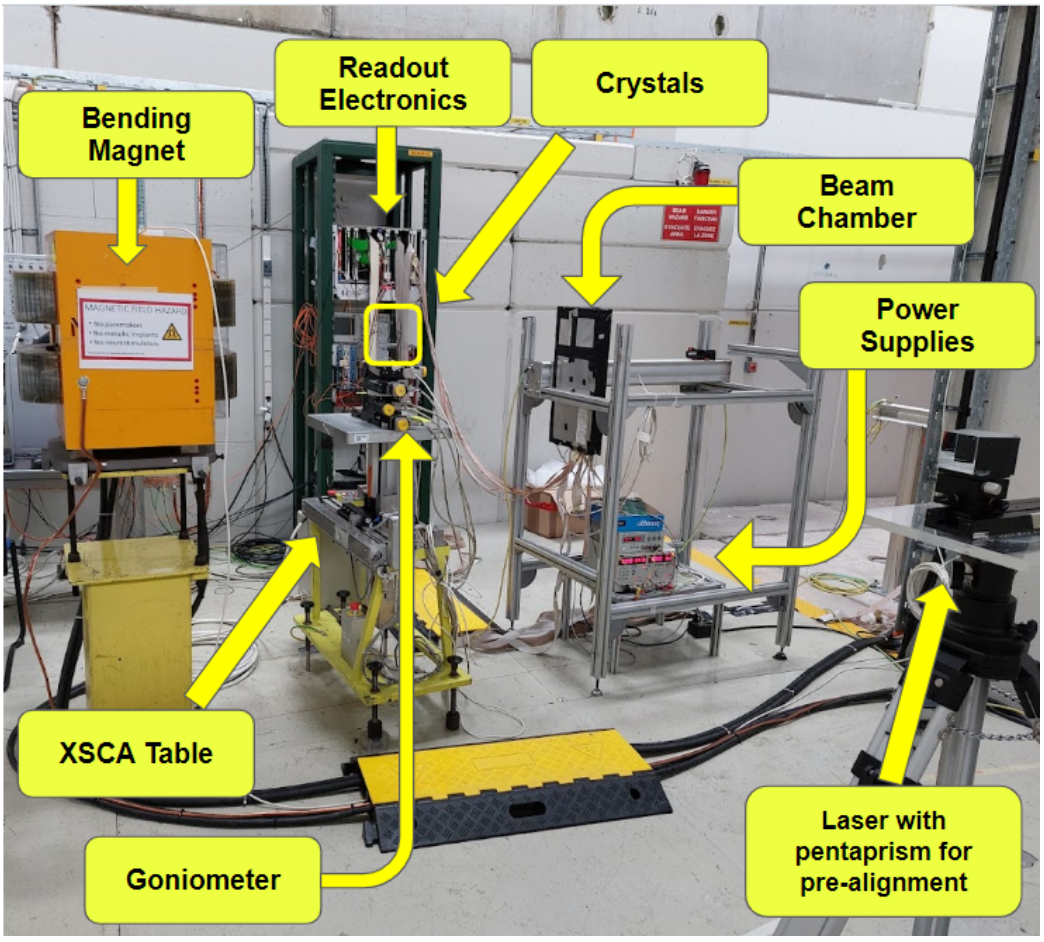

Figure 5.12: Photo of the experimental layout in the T9 experimental area for the August 2023 beamtest of the crystal based hybrid positron source.

corresponding to the crystals are clearly visible. This plot allowed to find the spatial position of the crystals, and therefore selecting a 3 cm wide vertical region, centered on the position of the crystals themselves, it was possible to acquire particles crossing any of the three crystals. Figure 5.14 presents the whole beam profile and the horizontal portion of the beam selected around the crystals triggering on the beam chambers in two different runs.

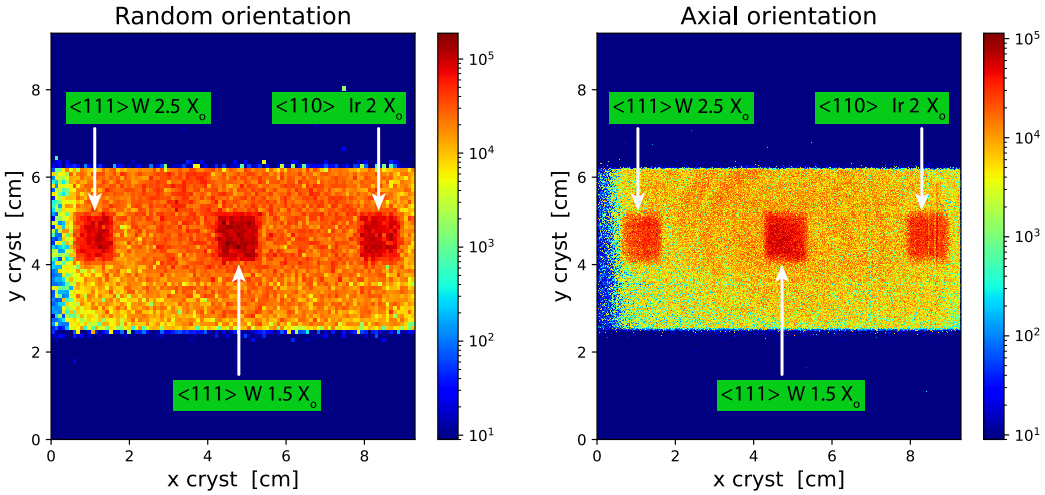

Figure 5.13: 2d histogram of the reconstructed tracks on the crystals plane weighted on the calorimeter pulse height. If the sweeping magnet is turned on, the calorimeter will only measure the energy deposited by photons, which are mainly produced by electrons inside the crystal radiator via bremsstrahlung: (left) random orientation; (right) axial orientation of the crystal in the middle, which has a larger intensity with respect to the background.

Once the crystals have been centered with respect to the beam, some *angular scans* have been performed, namely on the rotational and cradle goniometer stages, to find the axial direction of each crystal. Figure 5.15 presents the so called stereogram: each point of this plot represents a rotational-cradle pair measured during each scan. The color is relative to the mean pulse height in the lead glass calorimeter. The point with the highest value corresponds to the axial position.

Figure 5.16 presents an example of the photon spectrum as seen by the lead glass calorimeter for the non oriented (green) and oriented (orange) 1.5 mm thick $\langle 111 \rangle$ tungsten crystal selecting only the particles that cross the crystal itself within one critical angle with respect to the axial direction. Indeed, for all the runs with the magnet on, the spectrum looks similar and is the typical *bremsstrahlung spectrum*. The increment in the produced radiation

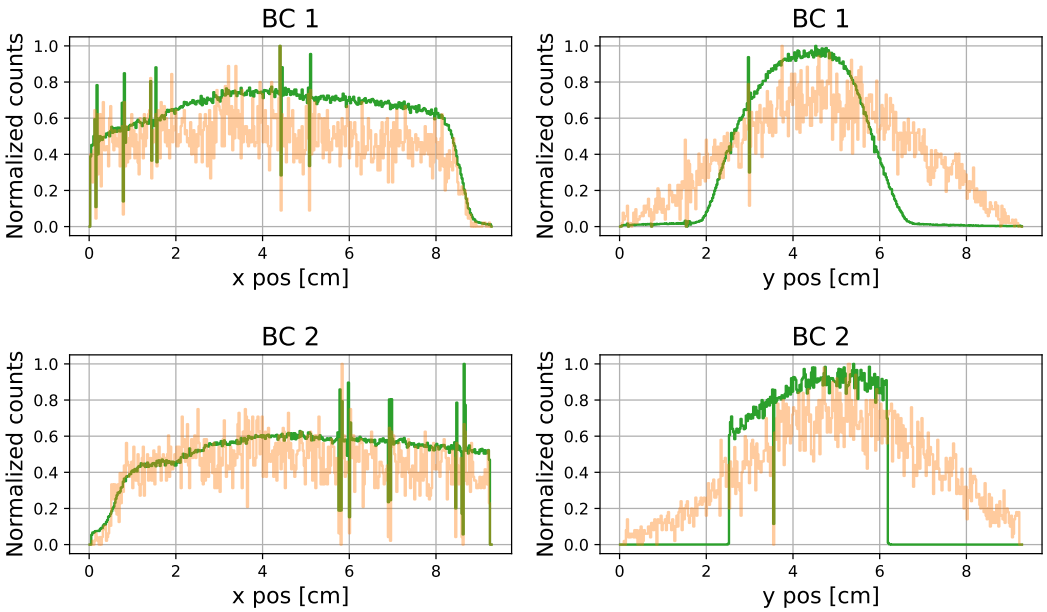

Figure 5.14: Whole beam profile (orange) and the horizontal portion of the beam (green) selected around the crystals, triggering on the beam chambers in two different runs.

is hard to see from the plot itself, however it becomes evident when looking at the mean values of the two histograms above the threshold (dotted line), which resulted to be approximately 2933.4 ADC and 3569.4 ADC for the non oriented and oriented crystal respectively.

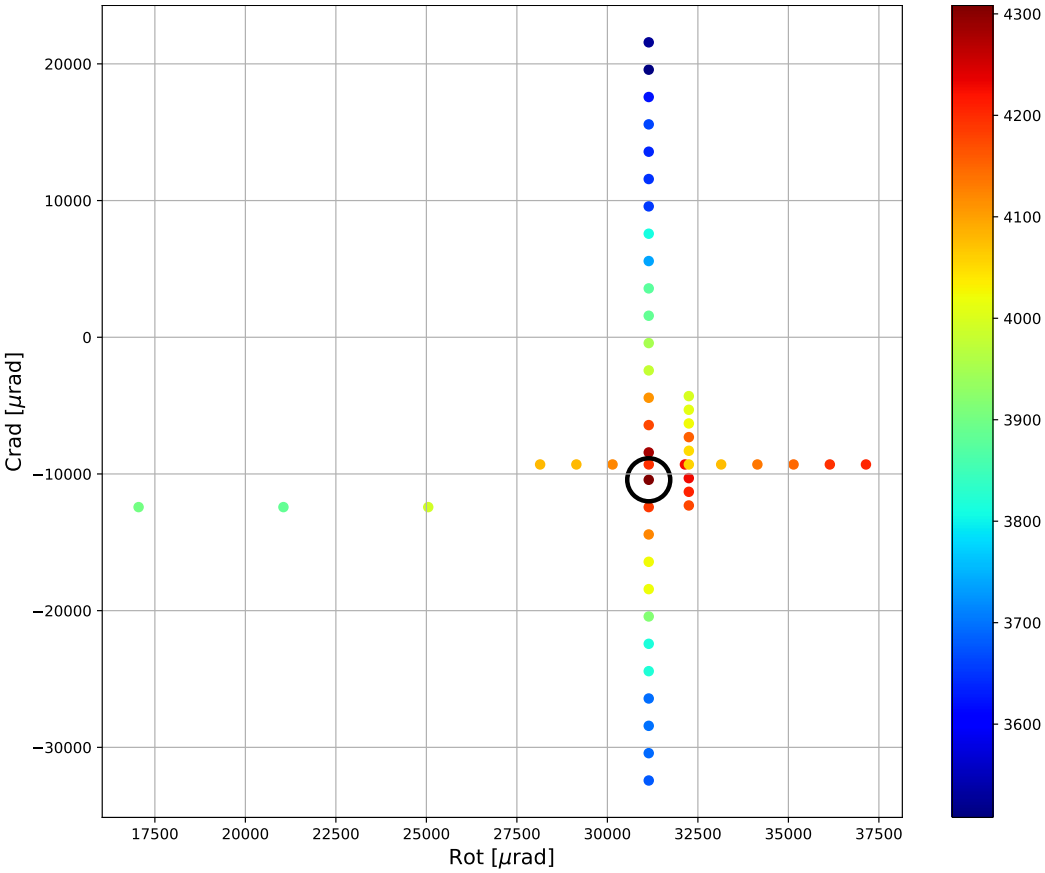

Figure 5.15: Stereogram plot: each point of this plot represents a rotational-cradle pair measured during each scan. The color is relative to the mean pulse height in the lead glass calorimeter.

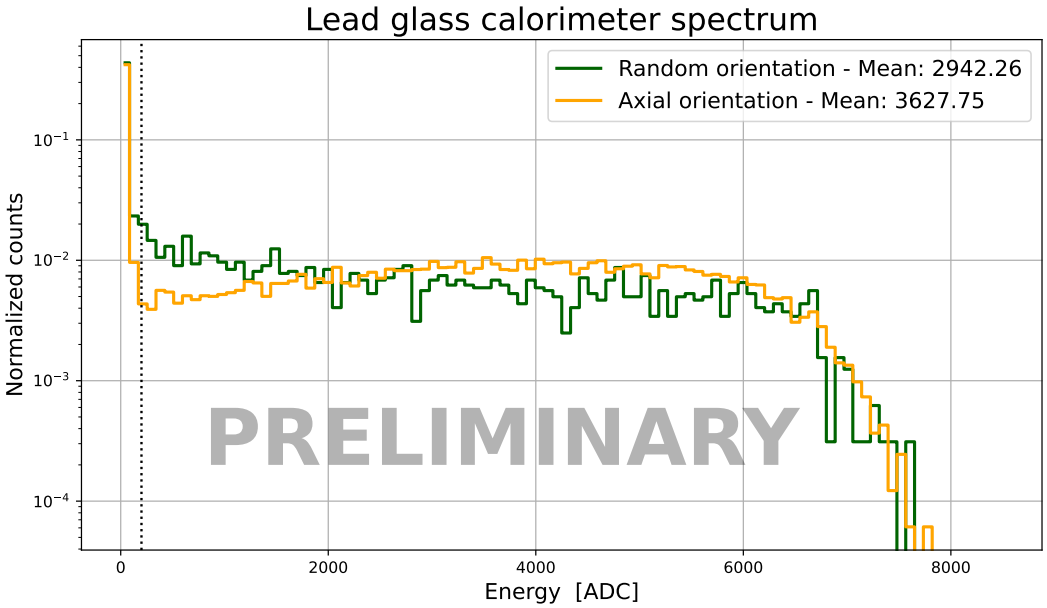

Figure 5.16: Photon spectrum as seen by the lead glass calorimeter for the non oriented (green) and oriented (orange) 1.5 mm thick ⟨111⟩ tungsten crystal selecting only the particles that cross the crystal itself. This is the typical *bremsstrahlung spectrum*, namely the spectrum of photons inside an electromagnetic calorimeter. The mean values of the histograms above the threshold (dotted line) are reported in the legend.

Conclusions

The idea of this thesis work was born in the framework of the feasibility tests of two applications of oriented crystals:

- The test of different possible crystal radiators for the design of a hybrid crystal based positron source, a key element for future e^+e^- colliders.
- The test of a new design of bent crystals, which consists in inserting a lattice interruption at the very beginning of the crystal itself that should act as a focussing lens, thus allowing to achieve a channelling efficiency of around 100 %.

These two ideas are at the basis of the e+BOOST project funded by the Italian Ministry of Research and the GALORE project of the National Institute of Nuclear Physics.

To identify the different effects in oriented crystals, it is fundamental to reconstruct the incoming direction of the particle and, in some cases (as in the GALORE project) the outgoing direction too, with a high spatial resolution tracking system, as the one used and upgraded for this thesis work.
Moreover, for crystals directional effects to happen, a very precise alignment of the crystal with respect to the particle beam is required. Furthermore, only particles that impinge onto the crystal face within the angular acceptance of the effect under study can undergo the effect itself.

The study and characterization of the GALORE and e+BOOST crystals required a strict control over the beam dimension and the beam angular divergence. Acting on the beam optics, it is possible to modify the divergence and the beam profile. Unfortunately, when decreasing the beam divergence, the beam profile increases, and vice versa. In order to acquire a statistics large enough, it turned out to be necessary to select only a portion of the beam.

This thesis work concerned the upgrade of the readout electronics of the INSULAB microstrip silicon detectors to allow them to self generate a trigger signal when crossed by charged particles in a given range of strips. The INSULAB tracking system has been developed to be used with the extracted

beams of the PS and SPS beamlines at CERN. It consists of several silicon strip detectors, with different dimensions and resolution, that have to be selected depending on the test that has to be performed. In particular two types of detectors have been upgraded during this thesis work: large area ($9.5 \times 9.5\,\mathrm{cm}^2$) single side beam chambers with a spatial resolution of around 40 μm and small single and double side silicon telescopes ($1.92 \times 1.92\,\mathrm{cm}^2$) with a spatial resolution in the 5-10 μm range. Some of these detectors are readout by ASICs with a self triggering capability. To implement this possibility, both the frontend and the readout electronics have been modified.

The preliminary tests on the upgraded readout electronics were performed in the laboratory. The performance of the ASICs has been verified with a dedicated procedure: after testing each channel with an external calibration signal to measure the analog response, the ASICs were tested in terms of noise trigger rate to identify the noisy channels that must be disabled by the DAQ system. The silicon detectors have been characterized studying the pull (that is the ratio of the pulse height of the strip with the maximum signal in the event and its rms noise), the cluster SNR and the eta distribution (which is a parameter defining the symmetry of the charge sharing). The pull and the cluster SNR allowed to measure the optimal value of the hold that is the time between the trigger and the sampling of the analog signal by the ASICs themselves. The hold scan is usually performed also when putting the detectors on the beam to optimize the SNR.

Once completed the laboratory tests, the single side telescopes have been taken to the BeamTest Facility of the Frascati National Laboratories to verify the performance on beam. The system proved to be able to select a portion of the beam, by using single detectors or a logic condition, such as the AND of two silicon modules. As a consequence of this selection, a reduction in the angular divergence was observed and measured. This result was fundamental in view of the GALORE beamtest where the control over both the beam size and the beam divergence was mandatory to understand the performance of the crystal design.

The GALORE beamtest was performed at CERN in June 2023 on the H8 SPS extracted beamline with a positive $180\,\mathrm{GeV}/c$ pion beam. The whole beam, which has a dimension of around 1 cm and a divergence of around 80 µrad, has been used to center the crystal on the beam: in fact, by filling a 2d histogram of the reconstructed x position on the crystal face for each particle versus the $\Delta\theta$ difference of the outgoing and incoming angles, the position of the crystal appears as an increase in the rms of the $\Delta\theta$ distribution itself.

The GALORE crystal is a 4.1 mm long in the beam direction silicon crystal with a face perpendicular to the beam of $0.5\,\mathrm{x}\,55\,\mathrm{mm}^2$. The micro

structure is 0.15x10 mm^2 measured in the middle of the crystal sample. If the whole beam were used, given the crystal size, only a few percent of the particles would have interacted with the crystal itself and thus almost all the events would have been rejected in the offline analysis. The possibility to select a very small region (thirteen 50 µm strips) allowed to acquire statistics 20 to 30 times faster while at the same time reducing the divergence from 86 µrad to 32.2 µrad.

The goal of this thesis was the development of the tracking system able to allow a measurement to be performed in a short time and not a detailed analysis of the crystal channeling performance, which anyway resulted to be at least 65% in the micro trench region. The goal of a $\sim 100\,\%$ channeling efficiency is still far from being reached, and this is probably related to imperfections in the crystal lattice.

The same approach was used also for the e+BOOST beamtest on the PS T9 beamline in August 2023. In this case the requirements were less stringent, but the possibility to trigger on a part of the beam in the vertical direction has allowed to test at the same time 3 different crystal radiators to be used in the design of a hybrid crystal based positron source collecting a large enough statistics. Aligning such crystals is an easier task with respect to the GALORE one, since a direct effect of the interaction of the crystal with the particle beam can be measured, namely the production of photons inside the crystal radiator itself. If a bending magnet is used to swipe all charged particles, an electromagnetic calorimeter can be used to detect and measure the produced radiation.

The upgraded test system proved to work properly, for both the experiments, allowing the collection of a statistics large enough in a short time (which is essential when taking data on extracted beamlines where different users have to alternate). Furthermore, thanks to its versatility, the same test system can be applied to any kind of beamtest where a high resolution particle tracking is needed, with the possibility to select a small portion of the beam thus reducing also the divergence, which is a fundamental parameter when studying oriented crystals.

List of acronyms

ADC	Analog to Digital Converter
AGILE	Astrorivelatore Gamma a Immagini LEggero (Light Imager for Gamma-ray Astrophysics)
ALICE	A Large Ion Collider Experiment
APC	Active Photon Converter
ASI	Agenzia Spaziale Italiana (Italian Space Agency)
ASIC	Application Specific Integrated Circuit
ATLAS	A Toroidal LHC Apparatus
BC	Beam Chamber
BiCMOS	Bipolar Complementary Metal Oxide Semiconductor
BTF	BeamTest Facility
CERN	Conseil Européen pour la Recherche Nucléaire (European Council for Nuclear Research)
ChR	Channelling Radiation
CLS	Crystal-based Light Sources
CM	Common Mode
CMS	Compact Muon Solenoid
CMOS	Complementary Metal Oxide Semiconductor
COG	Center Of Gravity
CSA	Charge Sensitive preAmplifier
DAC	Digital to Analog Converter
DAΦNE or **DAFNE**	Double Annular Φ Factory for Nice Experiments
DAQ	Data AcQuisition
DESY	Deutsches Elektronen-Synchrotron
EDM	Electric Dipole Moment
EHN1	Experimental Hall North 1
ENC	Equivalent Noise Charge
e+BOOST	Intense positron source Based On Oriented crySTals

FCC	Future Circular Collider
FPGA	Field Programmable Gate Array
GALORE	hiGh-efficient beAm defLector fOR accElerators
GUI	Graphical User Interface
HDI	High Density Interconnection
HEP	High Energy Physics
HL	High Luminosity
IC	Integrated Circuit
INFN	Istituto Nazionale di Fisica Nucleare (National Institute of Nuclear Physics)
IR	Insertion Region
LEP	Large Electron Positron collider
LHC	Large Hadron Collider
LHCb	Large Hadron Collider beauty
LINAC	LINnear ACcelerator
LVDS	Low-Voltage Differential Signaling
MDM	Magnetic Dipole Moment
MIP	Minimum Ionizing Particle
MUR	Ministero dell'Università e della Ricerca
PBC	Physics Beyond Colliders
PCB	Printed Circuit Board
PCI	Peripheral Component Interconnect
PH	Pulse Height
PLL	Phase Locked Loop
PMT	PhotoMultiplier Tube
PoT	Proton on Target
PS	Proton Synchrotron
PSB	Proton Synchrotron Booster
QFT	Quantum Field Theory
RAM	Random Access Memory
R&D	Research and Development
S&H	Sample and Hold
SASP	Small Amplitude and Small Period
SELDOM	SEarch for the eLectric Dipole MOment of strange and charm baryons at LHC
SiPM	Silicon PhotoMultiplier
SNR	Signal to Noise Ratio
SPS	Super Proton Synchrotron
TCCP	Target Collimator Crystal for Precession
TCCS	Target Collimator Crystal for Splitting
Tcl	Tool command language
TECHNO-CLS	TECHnology for Crystal Light Sources

TTL	Transistor-Transistor Logic
VCB	VME Cyclone Board
VISION	Versatile and Innovative SIlicON Telescopes
VME	Versa Module Eurocard
VRB	VME Readout Board

List of Figures

List of Tables

Bibliography

[1] N. Ashcroft and D. Mermin. *Solid State Physics*. 1976.

[2] W. H. Bragg and W. L. Bragg. "The Structure of the Diamond". In: *Proceedings of the Royal Society of London. Series A, Containing Papers of a Mathematical and Physical Character* 89.610 (1913), pp. 277–291. ISSN: 09501207. DOI: https://doi.org/10.1098/rspa.1913.0084. URL: http://www.jstor.org/stable/93489 (visited on 09/14/2023).

[3] M. Romagnoni et al. "Bent Crystal Design and Characterization for High-Energy Physics Experiments". In: *Crystals* 12.9 (2022). ISSN: 2073-4352. DOI: 10.3390/cryst12091263. URL: https://www.mdpi.com/2073-4352/12/9/1263.

[4] L. Bandiera et al. "A highly-compact and ultra-fast homogeneous electromagnetic calorimeter based on oriented lead tungstate crystals". In: *Frontiers in Physics* 11 (2023). ISSN: 2296-424X. DOI: 10.3389/fphy.2023.1254020. URL: https://www.frontiersin.org/articles/10.3389/fphy.2023.1254020.

[5] D. Mirarchi, A. S. Fomin, S. Redaelli, et al. "Layouts for fixed-target experiments and dipole moment measurements of short-lived baryons using bent crystals at the LHC". In: *Eur. Phys. J. C* 80 (2020). DOI: 10.1140/epjc/s10052-020-08466-x. URL: https://doi.org/10.1140/epjc/s10052-020-08466-x.

[6] K. A. Dewhurst et al. "Performance of a double-crystal setup for LHC fixed-target experiments". In: *14th International Particle Accelerator Conference, Venezia*. Ed. by JACoW Publishing. 2023. ISBN: 978-3-95450-231-8. DOI: doi/jacow-ipac2023-mopl048/index.html. URL: doi:%20doi/jacow-ipac2023-mopl048/index.html.

[7] P. D. Hermes et al. "Layouts for feasibility studies of fixed-target experiments at the LHC". In: *IPAC2022, Bangkok, Thailand*. Ed. by JACoW Publishing. 2022. ISBN: 978-3-95450-227-1. DOI: 10.18429/JACoW-IPAC2022-WEPOTK033. URL: https://accelconf.web.cern.ch/ipac2022/papers/wepotk033.pdf.

[8] A. Y. Silenko. "Measurement of quadrupole moments of unstable nuclei during channeling and the possibility of revealing the effect of vector polarization of tensor-polarized beams of nuclei". In: *Physics of Particles and Nuclei Letters* 8.4 (July 2011), pp. 368–373. DOI: 10.1134/S1547477111040145.

[9] V. L. Lyuboshits. "Spin rotation associated with the deflection of a relativistic charged particle in an electric field". In: *Sov. J. Nucl. Phys. (Engl. Transl.); (United States)* 31:4 (Apr. 1980). URL: https://www.osti.gov/biblio/6562813.

[10] D. Chen et al. "First observation of magnetic moment precession of channeled particles in bent crystals". In: *Physical review letters* 69 (Jan. 1993), pp. 3286–3289. DOI: 10.1103/PhysRevLett.69.3286.

[11] *LHC Run 3: physics at record energy starts tomorrow*. URL: https://home.cern/news/news/physics/lhc-run-3-physics-record-energy-starts-tomorrow.

[12] L. Rossi and O. Brüning. "Introduction to the HL-LHC Project". In: *Adv. Ser. Direct. High Energy Phys.* 24 (2015). Ed. by Oliver Brüning and Lucio Rossi, pp. 1–17. DOI: 10.1142/9789814675475_0001.

[13] R. Assmann et al. "The final collimation system for the LHC". In: *Proceedings of EPAC 2006*. May 2006.

[14] *Emerging technologies for crystal-based gamma-ray light sources*. URL: https://cordis.europa.eu/project/id/101046458.

[15] A. V. Korol et al. *Novel Light Sources beyond Free Electron Lasers*. Ed. by Springer Nature Switzerland AG. 2022.

[16] A. V. Korol et al. "Atomistic modeling and characterizaion of light sources based on small-amplitude short-period periodically bent crystals". In: *Nuclear Instruments and Methods in Physics Research Section B: Beam Interactions with Materials and Atoms* 537 (Apr. 2023), pp. 1–13. DOI: 10.1016/j.nimb.2023.01.012. URL: https://doi.org/10.1016%2Fj.nimb.2023.01.012.

[17] U. I. Uggerhøj. "The interaction of relativistic particles with strong crystalline fields". In: *Rev. Mod. Phys.* 77 (4 Oct. 2005), pp. 1131–1171. DOI: 10.1103/RevModPhys.77.1131. URL: https://link.aps.org/doi/10.1103/RevModPhys.77.1131.

[18] A. V. Korol et al. *Channeling and Radiation in Periodically Bent Crystals*. Ed. by Springer-Verlag. 2014.

[19] W. Scandale et al. "Comprehensive study of beam focusing by crystal devices". In: *Phys. Rev. Accel. Beams* 21 (1 Jan. 2018), p. 014702. DOI: 10.1103/PhysRevAccelBeams.21.014702. URL: https://link.aps.org/doi/10.1103/PhysRevAccelBeams.21.014702.

[20] *Beam H8 - PPE128*. URL: https://edms.cern.ch/ui/file/1605378/1/H8_ZONE_PPE128_Model_(1).pdf.

[21] P. Schwarz. *Electrical circuits layout between converters and magnets - SPS North Area*. URL: https://edms.cern.ch/ui/file/1605378/1/H8_ZONE_PPE128_Model_(1).pdf.

[22] S. Redaelli et al. *Crystal collimation brings HL-LHC into focus*. URL: https://cerncourier.com/a/crystal-collimation-brings-hl-lhc-into-focus/.

[23] P. D. Hermes et al. "LHC Heavy-Ion Collimation Quench Test at 6.37 Z TeV". In: (2016). URL: https://cds.cern.ch/record/2136828.

[24] L. Alexandru. *Upgrading CERN with niobium-tin magnets*. URL: https://h2020-tarantula.eu/upgrading-cern-with-niobium-tin-magnets/.

[25] W. Scandale et al. "Observation of channeling for 6500 GeV/c protons in the crystal assisted collimation setup for LHC". In: *Physics Letters B* 758 (2016), pp. 129–133. ISSN: 0370-2693. DOI: https://doi.org/10.1016/j.physletb.2016.05.004. URL: https://www.sciencedirect.com/science/article/pii/S0370269316301514.

[26] A. Selmi. "Electromagnetic Shower Development in Oriented Crystals". MSc Thesis, Università degli Studi dell'Insubria. 2022. URL: https://cds.cern.ch/record/2814582.

[27] *Crystalline structure*. URL: https://physics.itmo.ru/sites/default/files/courses/additional_documents/crystallinestructureptx_0.pdf.

[28] W. H. Miller. *A treatise on crystallography*. Ed. by Deighton. 1839.

[29] American Physical Society. *Crystallographic Notation*. URL: https://journals.aps.org/authors/crystallographic-notation-h1.

[30] A. H. Sørensen et al. "Channelling and channelling radiation". In: *Nature* 325 (1987). DOI: https://doi.org/10.1038/325311a0. URL: https://doi.org/10.1038/325311a0.

[31] J. Stark et al. "Serienemission an festen Metallverbindungen durch Kanalstrahlen. Schwellenwert der erregenden Energie". In: *Phys. Z.* 13 (1912), pp. 973–977. URL: https://scholar.archive.org/work/fjdjdec3tlzbzpnty67v4uke434/access/ia_file/crossref-pre-1923-scholarly-works/10.1002%252Fandp.19123420414.zip/10.1002%252Fandp.19123430809.pdf.

[32] M. Wortis. "Bound States of Two Spin Waves in the Heisenberg Ferromagnet". In: *Phys. Rev.* 132 (1 Oct. 1963), pp. 85–97. DOI: 10.1103/PhysRev.132.85. URL: https://link.aps.org/doi/10.1103/PhysRev.132.85.

[33] J. Lindhard. "Influence of Crystal Lattice on Motion of Energetic Charged Particles". In: *Dan. Vid. Selsk. Mat. Fys. Medd.* 34 (1965).

[34] A. H. Sørensen. "Channeling, bremsstrahlung and pair creation in single crystals". In: *Nuclear Instruments and Methods in Physics Research Section B: Beam Interactions with Materials and Atoms* 119.1 (1996), pp. 2–29. ISSN: 0168-583X. DOI: https://doi.org/10.1016/0168-583X(96)00349-7. URL: https://www.sciencedirect.com/science/article/pii/0168583X96003497.

[35] A. H. Sørensen. "Erratum to: "Channeling, Bremsstrahlung and Pair Creation in Single Crystals; Preamble" [Nucl. Instr. and Meth. B 119 (1996) 1–29]". In: *Nuclear Instruments and Methods in Physics Research Section B: Beam Interactions with Materials and Atoms* 122.1 (1997), p. 168. ISSN: 0168-583X. DOI: https://doi.org/10.1016/S0168-583X(96)00775-6. URL: https://www.sciencedirect.com/science/article/pii/S0168583X96007756.

[36] A. Sørensen and E. Uggerhøj. "Channelling and channelling radiation". In: *Nature* (Jan. 1987). DOI: 10.1038/325311a0.

[37] V. Guidi et al. "Silicon crystal for channelling of negatively charged particles". In: *Journal of Physics D: Applied Physics* 42.18 (Aug. 2009), p. 182005. DOI: 10.1088/0022-3727/42/18/182005. URL: https://dx.doi.org/10.1088/0022-3727/42/18/182005.

[38] A. M. Taratin and S. A. Vorobiev. ""Volume reflection" of high-energy charged particles in quasi-channeling states in bent crystals". In: *Physics Letters A* 119.8 (1987), pp. 425–428. ISSN: 0375-9601. DOI: https://doi.org/10.1016/0375-9601(87)90587-1. URL: https://www.sciencedirect.com/science/article/pii/0375960187905871.

[39] Yu. M. Ivanov et al. "Volume Reflection of a Proton Beam in a Bent Crystal". In: *Phys. Rev. Lett.* 97 (14 Oct. 2006), p. 144801. DOI: 10.1103/PhysRevLett.97.144801. URL: https://link.aps.org/doi/10.1103/PhysRevLett.97.144801.

[40] W. Scandale et al. "High-Efficiency Volume Reflection of an Ultrarelativistic Proton Beam with a Bent Silicon Crystal". In: *Phys. Rev. Lett.* 98 (15 Apr. 2007), p. 154801. DOI: 10.1103/PhysRevLett.98.154801. URL: https://link.aps.org/doi/10.1103/PhysRevLett.98.154801.

[41] J. D. Jackson. *Classical Electrodynamics*. Ed. by Wiley Press. Wiley Press, 1975. ISBN: 978-0471309321.

[42] A. Sørensen and E. Uggerhøj. "Channeling, Radiation and Applications". In: *Nucl. Sci. Appl.* 3 (1989), p. 147. URL: https://books.google.com/books?hl=it&lr=&id=v6QMLI6v3j0C&oi=fnd&pg=PA147&dq=SerensenUggerhej+Channeling,+Radiation+and+Applications+1989&ots=1CLZFylRLd&sig=rirYqbTOD1psQ_C9WLbmDFIDpL0.

[43] P. G. Ratcliffe. *Introduction to elementary particle phenomenology*. Lecture notes. 2021.

[44] J. D. Bjorken and S. D. Drell. *Relativisic Quantum Mechanics*. Ed. by McGraw-Hill. McGraw-Hill, 1964. ISBN: 978-0070054936.

[45] H. Bethe and W. Heitler. "On the stopping of fast particles and on the creation of positive electrons". In: *Proceedings of the Royal Society of London. Series A, Containing Papers of a Mathematical and Physical Character* 146.856 (1934), pp. 83–112. URL: https://royalsocietypublishing.org/doi/pdf/10.1098/rspa.1934.0140.

[46] W. Zhu. "Improved Bethe-Heitler formula". In: *Nuclear Physics B* 953 (2020), p. 114958. ISSN: 0550-3213. DOI: https://doi.org/10.1016/j.nuclphysb.2020.114958. URL: https://www.sciencedirect.com/science/article/pii/S0550321320300444.

[47] E. Fermi. "Statistical method to determine some properties of atoms". In: *Rend. Accad. Naz. Lincei* 6.602-607 (1927), p. 5. URL: https://ipparco.roma1.infn.it/pagine/deposito/2011/TF.pdf.

[48] E. Fermi. "Eine statistische Methode zur Bestimmung einiger Eigenschaften des Atoms und ihre Anwendung auf die Theorie des periodischen Systems der Elemente". In: *Zeitschrift für Physik* 48.1-2 (1928), pp. 73–79. URL: https://link.springer.com/article/10.1007/BF01351576.

[49] R. L. Workman et al. "Review of Particle Physics". In: *PTEP* 2022 (2022), p. 083C01. DOI: 10.1093/ptep/ptac097.

[50] Y. S. Tsai. "Pair production and bremsstrahlung of charged leptons". In: *Rev. Mod. Phys.* 46 (4 Oct. 1974), pp. 815–851. DOI: 10.1103/RevModPhys.46.815. URL: https://link.aps.org/doi/10.1103/RevModPhys.46.815.

[51] L. Bandiera et al. "Crystal-based pair production for a lepton collider positron source". In: *The European Physical Journal C* 82.699 (2022). DOI: 10.1140/epjc/s10052-022-10666-6. URL: https://doi.org/10.1140/epjc/s10052-022-10666-6.

[52] I. Chaikovska et al. "Positron sources: from conventional to advanced accelerator concepts-based colliders". In: *Journal of Instrumentation* 17.05 (May 2022), P05015. DOI: 10.1088/1748-0221/17/05/P05015. URL: https://dx.doi.org/10.1088/1748-0221/17/05/P05015.

[53] X. Artru et al. "Polarized and unpolarized positron sources for electron–positron colliders". In: *Nuclear Instruments and Methods in Physics Research Section B: Beam Interactions with Materials and Atoms* 266.17 (2008). Radiation from Relativistic Electrons in Periodic Structures, pp. 3868–3875. ISSN: 0168-583X. DOI: https://doi.org/10.1016/j.nimb.2008.02.086. URL: https://www.sciencedirect.com/science/article/pii/S0168583X08001894.

[54] D. A. Edwards and M. J. Syphers. *An introduction to the physics of high energy accelerators*. Ed. by Wiley. Wiley, 1993. ISBN: 978-0-471-55163–8.

[55] M. Soldani et al. "Radiation in oriented crystals: Innovative application to future positron sources". In: *Nuclear Instruments and Methods in Physics Research Section A: Accelerators, Spectrometers, Detectors and Associated Equipment* 1058 (2024), p. 168828. ISSN: 0168-9002. DOI: https://doi.org/10.1016/j.nima.2023.168828. URL: https://www.sciencedirect.com/science/article/pii/S0168900223008197.

[56] L. Bandiera et al. "Strong Reduction of the Effective Radiation Length in an Axially Oriented Scintillator Crystal". In: *Phys. Rev. Lett.* 121 (2 July 2018), p. 021603. DOI: 10.1103/PhysRevLett.121.021603. URL: https://link.aps.org/doi/10.1103/PhysRevLett.121.021603.

[57] V. V. Tikhomirov. "A technique to improve crystal channeling efficiency of charged particles". In: *Journal of Instrumentation* 2.08 (Aug. 2007), P08006. DOI: 10.1088/1748-0221/2/08/P08006. URL: https://dx.doi.org/10.1088/1748-0221/2/08/P08006.

[58] M. Romagnoni et al. "The GALORE project". In: *Eur. Phys. J. D* 76.8 (2022), p. 135. DOI: 10.1140/epjd/s10053-022-00439-x.

[59] C. Barschel et al. *LHC fixed target experiments: Report from the LHC Fixed Target Working Group of the CERN Physics Beyond Colliders Forum*. Vol. 4/2020. CERN Yellow Reports: Monographs. Geneva: CERN, 2020. ISBN: 978-92-9083-573-8, 978-92-9083-574-5. DOI: 10.23731/CYRM-2020-004.

[60] E. Uggerhøj and U. I. Uggerhøj. "Strong crystalline fields – a possibility for extraction from the LHC". In: *Nuclear Instruments and Methods in Physics Research Section B: Beam Interactions with Materials and Atoms* 234.1 (2005). Relativistic Channeling and Related Coherent Phenomena in Strong Fields, pp. 31–39. ISSN: 0168-583X. DOI: https://doi.org/10.1016/j.nimb.2005.01.007. URL: https://www.sciencedirect.com/science/article/pii/S0168583X05000108.

[61] C. Hadjidakis et al. "A fixed-target programme at the LHC: Physics case and projected performances for heavy-ion, hadron, spin and astroparticle studies". In: *Physics Reports* 911 (May 2021), pp. 1–83. DOI: 10.1016/j.physrep.2021.01.002. URL: https://doi.org/10.1016%2Fj.physrep.2021.01.002.

[62] A. Gerbershagen and B. Rae. *The H8 Secondary Beam Line of EHN1/SPS*. URL: https://sba.web.cern.ch/sba/BeamsAndAreas/H8/H8_presentation.html.

[63] W. Scandale et al. "Apparatus to study crystal channeling and volume reflection phenomena at the SPS H8 beamline". In: *Review of Scientific Instruments* 79.2 (Feb. 2008), p. 023303. ISSN: 0034-6748. DOI: https://doi.org/10.1063/1.2832638. URL: https://pubs.aip.org/aip/rsi/article/79/2/023303/386945/Apparatus-to-study-crystal-channeling-and-volume.

[64] P. Monti-Guarnieri. "Beamtest characterization of oriented crystals for the KLEVER Small Angle Calorimeter". MSc Thesis, Università degli Studi dell'Insubria. 2023. URL: http://cds.cern.ch/record/2850897.

[65] *CERN accelerator complex*. URL: https://home.cern/science/accelerators/accelerator-complex.

[66] S. Aretz et al. "An Overview of the CERN Beamline for Schools Competition". In: *The Physics Educator* 02.01 (2020), p. 2050001. DOI: 10.1142/S2661339520500018. URL: https://doi.org/10.1142/S2661339520500018.

[67] J. Bernhard et al. *CERN Proton Synchrotron East Area Facility: Upgrades and renovation during Long Shutdown 2*. Ed. by J. Bernhard. Vol. 4/2021. CERN Yellow Reports: Monographs. Geneva: CERN, 2021. DOI: 10.23731/CYRM-2021-004. URL: http://cds.cern.ch/record/2792490.

[68] N. Charitonidis et al. "Estimation of the R134a gas refractive index for use as a Cherenkov radiator, using a high energy charged particle beam". In: *Nuclear Instruments and Methods in Physics Research Section B: Beam Interactions with Materials and Atoms* 410 (2017), pp. 134–138. ISSN: 0168-583X. DOI: https://doi.org/10.1016/j.nimb.2017.08.020. URL: https://www.sciencedirect.com/science/article/pii/S0168583X17308133.

[69] D. Dannheim et al. "Particle Identification with Cherenkov detectors in the 2011 CALICE Tungsten Analog Hadronic Calorimeter Test Beam at the CERN SPS". In: (2013). URL: https://cds.cern.ch/record/1545809.

[70] C. Pralavorio. *LS2 Report: Focus on the North area*. URL: https://home.cern/news/news/engineering/ls2-report-focus-north-area.

[71] Na62 collaboration. *Na62 website: Experimental Area*. URL: https://na62.web.cern.ch/ExperimentalArea/SchematicNorthArea.html.

[72] L. Gatignon. "Design and Tuning of Secondary Beamlines in the CERN North and East Areas". In: (2020). URL: https://cds.cern.ch/record/2730780.

[73] *DAΦNE*. URL: http://www.lnf.infn.it/cee/STRONG2020/dafne.html.

[74] B. Buonomo et al. *The Frascati Beam Test Facility*. 2023. arXiv: 2308.03058 [physics.acc-ph]. URL: https://arxiv.org/abs/2308.03058.

[75] M. Prest et al. "The AGILE silicon tracker: an innovative γ-ray instrument for space". In: *Nuclear Instruments and Methods in Physics Research Section A: Accelerators, Spectrometers, Detectors and Associated Equipment* 501.1 (2003). Proceedings of the 10th International Workshop on Vertex Detectors, pp. 280–287. ISSN: 0168-9002. DOI: https://doi.org/10.1016/S0168-9002(02)02047-8. URL: https://www.sciencedirect.com/science/article/pii/S0168900202020478.

[76] G. Barbiellini et al. *The AGILE Silicon Tracker: architectural design and prototype testbeam results*. 2001. DOI: 10.15161/oar.it/1449011376.29. URL: https://doi.org/10.15161/oar.it/1449011376.29.

[77] G. Barbiellini et al. "The AGILE silicon tracker: testbeam results of the prototype silicon detector". In: *Nuclear Instruments and Methods in Physics Research Section A: Accelerators, Spectrometers, Detectors and Associated Equipment* 490.1 (2002), pp. 146–158. ISSN: 0168-9002. DOI: https://doi.org/10.1016/S0168-9002(02)01062-8. URL: https://www.sciencedirect.com/science/article/pii/S0168900202010628.

[78] D. Lietti. *Vision: a versatile and innovative silicon tracking system*. PhD Thesis, Università degli Studi dell'Insubria. 2013. URL: https://cds.cern.ch/record/2626151.

[79] IDEAS. *The VA1TA, Version 0.9*. the datasheet is provided directly by the firm.

[80] *NE592 Video Amplifier datasheet*. URL: https://www.onsemi.com/pdf/datasheet/ne592-d.pdf.

[81] *A2818 - PCI CONET Controller*. URL: https://www.caen.it/products/a2818/.

[82] D. Bolognini. *Study of Channeling Phenomena in Bent Crystals: the New Frontiers*. MSc Thesis, Università degli Studi dell'Insubria. 2008. URL: https://drive.google.com/file/d/1Kh6f5yciI7IBBEvMEmLnn_xLQ2ffvNjk/view?usp=sharing.

[83] D. Bolognini. *The MICE Electron Muon Ranger: a Fundamental Step Towards a Neutrino Factory*. PhD Thesis, Università degli Studi dell'Insubria. 2012. URL: https://inspirehep.net/literature/1326510.

[84] M. Romagnoni. *GALORE beam test*. URL: https://indico.cern.ch/event/1275868/contributions/5358777/attachments/2631832/4552042/H8%20GALORE.pdf.